A Head Mounted Digital Image Warping Prosthesis for Age-Related Macular Degeneration

A THESIS

SUBMITTED TO THE FACULTY OF

THE UNIVERSITY OF MINNESOTA

BY

Eric Kenneth Victorson

IN PARTIAL FULFILLMENT OF THE REQUIREMENTS

FOR THE DEGREE OF MASTER OF SCIENCE

Arthur Erdman, PhD

May, 2014

Acknowledgements

Thank you to the University of Minnesota Medical Devices Center, Gordon Legge, PhD, Stephen Engel, PhD, Timothy Kowalewski, PhD, Mary Ruff, OT, Mr. Andrew Stewart, Mr. Phillip Webber, and the University of Minnesota Mechanical Engineering and Ophthalmology and Visual Neurosciences departments.

Dedication

To coffee and my close friends and family, for repeatedly helping me work until I lost my mind, and then kindly finding and returning it to me.

Abstract

Age-related Macular Degeneration is a medical condition affecting an estimated 1.75 million Americans aged 40 years and older, with that number expected to grow to 2.95 million by 2020. AMD is a leading cause of blindness in the population aged 65 and over. Many existing methods to cope for the disease operate using the principle that magnifying an image results in a smaller portion it being lost due to a macular scotoma. With the increasing use of electronic vision enhancement systems (EVES) in recent years, a head mounted digital image warping prosthesis for use with AMD has been created that remaps images in a manner that compensates for central visual field defects.

Contents

List of Tables

List of Figures

Chapter 1

Introduction

Age-related macular degeneration is one of the leading causes of legal blindness in developed nations in individuals aged 65 and older. Due to the decreasing cost of computational power, in recent years electronic vision enhancement systems (EVES) have begun to gain popularity in the research community. This work will present the development of a head mounted digital image warping prosthesis for the compensation of central visual field defects accompanying exudative and non-exudative age-related macular degeneration.

- Chapter 2 presents the necessary anatomy and physiology concerning the human eye to understand the work of this thesis, an introduction to macular degeneration and current treatments, a review of necessary topics in geometric optics, and related work.
- Chapter 3 reflects design goals and methodology considerations, a background of spatial transformations and those used within this work, mathematical considerations of image warping and other concerns.
- Chapter 4 reviews difficulties in the development of the image warping software, including increasing frame rate and noise and disturbance rejection.
- Chapter 5 covers the experimental design, setup and procedure to verify the hypothesis that warping an image to a parafoveal region will increase reading rate.

- Chapter 6 presents the experimental results and any side effects.
- Chapter 7 provides a review of the work within this thesis, a discussion of the experimental results and conclusions.
- Appendix A covers calibrating the eye tracking software to new users.
- Appendix B presents an in depth look at the software developed.
- Appendix C highlights the MNRead test used for experimental validation.
- Appendix D provides a glossary and list of acronyms.

Chapter 2

Background

2.1 **Anatomy of the Eye**

Of the five special senses in humans (smell, taste, sight, hearing and equilibrium), and the somatic senses (touch), vision is the dominant form of processing our environments. Roughly 70% of sensory receptors in the body are located in the eyes, and nearly 40% of the cerebral cortex is involved in processing visual information. [1]

The eye consists of a fibrous outer layer (corneoscleral tunic), a vascular middle layer (uveal tunic), and an inner layer (retinal tunic), sometimes referred to as the nervous layer. In addition to these layers are the anterior and posterior chambers, as well as the vitreous chamber. The posterior 5/6 of the fibrous layer corresponds to the white sclera, and the anterior 1/6 to the transparent cornea, through which light enters the eye. In order to remain healthy, the cells of the corneal epithelium must be kept moist, whose duty falls upon the pre-corneal tear film layer, or PCTF. The tear film layer maintains the health of the corneal surface; it preserves clear vision by filling in irregularities in the ocular surface, and is the primary source of waste removal, as well as nutrition, for the outer surface of the eye. The avascular cornea is richly supplied with nerve endings, and is one of the cumulative elements that allows for refraction of light within the eye. Figure 2.1 shows the constituent elements of the human eye's fibrous layer.

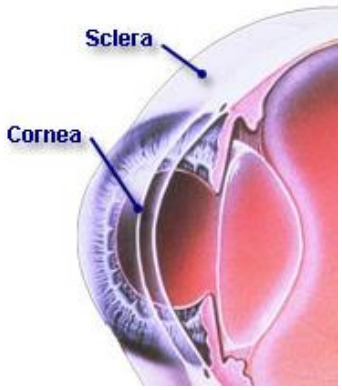

Figure 2.1: Corneoscleral Tunic [2]

The vascular layer, or uvea, consists of the highly vascular choroid, the ciliary body, and the iris. The choroid is consistent with the inner layer of the sclera, and its myriad blood vessels serve to nourish the outer layers of the eye. The choroid is darkly pigmented, generally brown due to its high melanin content, and serves to absorb light that is scattered within the eye, thereby preventing visual confusion that would result from internal reflections within the eye. Anterior to the choroid, the ciliary body, consisting of the ciliary muscle itself and ciliary processes, joins the ciliary zonule which attaches to the eye's crystalline lens. Contraction of the ciliary muscle results in reduced zonular tension, which causes the crystalline lens to change curvature and thereby allow accommodation, the process of changing the refractive power of the eye. This accommodation can result in a range of refraction of approximately 13 diopters, and is the only source of variable refraction, allowing the eye to change focus from a distance object to near objects. The last portion of the vascular layer is the iris, whose open central portion is the pupil which acts as an aperture for incoming light. For the optical system of the vertebrate eye, the iris acts as an aperture which determines how collimated light is that enters the eye, as well as the cone angle of a bundle of light rays to be focused on the imaging plane, the retina. Figure 2.2 illustrates the uveal tunic of the eye.

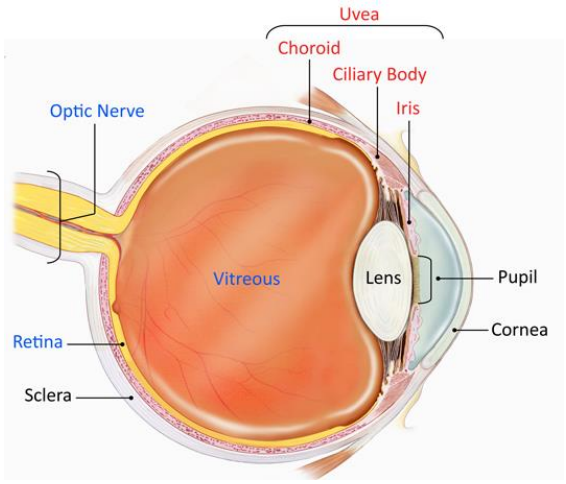

Figure 2.2: Uveal Tunic [3]

The area anterior to the crystalline lens and posterior to the cornea, comprising the anterior (area anterior to the iris) and posterior chambers (area posterior to iris, but anterior to crystalline lens), is filled with aqueous humor. The aqueous humor is a gelatinous liquid that serves to maintain intra-ocular pressure, assist vision as an ocular medium which aids in refraction, and provides nutrition to avascular tissues surrounding the anterior and posterior chambers. The chamber posterior to the crystalline lens is known as the vitreous chamber, and is correspondingly filled with vitreous humor. [2] The vitreous, unlike the aqueous humor, is virtually fixed from birth and accounts very little for changes in intra-ocular pressure due to the fact that the aqueous humor circulates while the vitreous does not. The aqueous humor, along with the crystalline lens, cornea, vitreous humor and pre-corneal tear film layer have differing indices of refraction and account for the refractive surfaces within the eye (the crystalline lens is typically modelled using a gradient index of refraction, but simplicity will be used here). Table 2.1 below lists the refractive indices for these constituent elements according to the Le Grand Schematic Eye model, and Emsley Simplified and Reduced Schematic Eye models. [4]

Table 2.1: Parameters of Paraxial Models of the Human Eye [5]

		Schematic Eye [6]	Simplified Schematic Eye [7]	Reduced Eye [7]
Radii of curvature (mm)	Anterior Cornea	7.8	7.8	5.55
	Posterior Cornea	6.5	-	-
	Anterior Lens	10.2	10	-
	Posterior Lens	-6	-6	-
Distance from anterior cornea (mm)	Posterior Cornea	0.55	-	-
	Anterior Lens	3.6	3.6	-
	Posterior Lens	7.6	7.2	-
	Retina	24.2	23.9	-
	1st principal point P	1.59	1.55	0
	2nd principal point P'	1.91	1.85	0
	1st nodal point N	7.2	7.06	5.55
	2nd nodal point N'	7.51	7.36	5.55
	1st focal point F	-15.09	-14.99	-16.67
	2nd focal point F'	24.2	23.9	22.22
Refractive indices	Tear Film	1.3369	-	-
	Cornea	1.3771	-	1.33
	Aqueous humor	1.3374	1.333	1.33
	Lens	1.42	1.416	1.33
	Vitreous humor	1.336	1.333	1.33

The inner layer of the eye consists of the retina and optic nerve. The retina consists of a thin pigmented layer, known as the retinal pigment epithelium, which serves much the same purpose as the choroid with the exception of vascularization, as it assists in absorbing scattered light, and a thick neural layer that contains the numerous photoreceptor cells. The sensing capability of the eye comes from the neural layer, consisting of photoreceptor cells, bipolar cells, and ganglion cells. When stimulated by incident light, the eye's photoreceptor neurons signal the bipolar cells,

which in turn signal the ganglion cells to create action potentials. These action potentials are then sent along axons which converge to form the optic nerve. These elements may be seen in Figure 2.3 below.

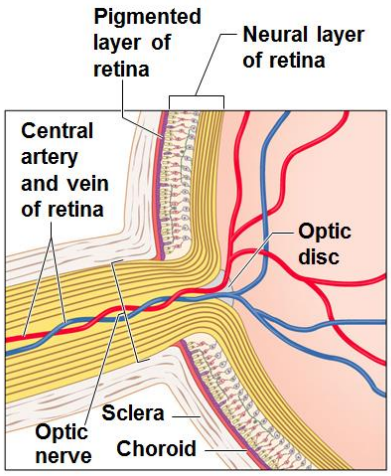

Figure 2.3: RPE and Neural Retina [1]

The photoreceptor cells come in two disparate varieties: rod cells and cone cells, so called because of their apparent shape. Rod cells are much more abundant and sensitive to light; capable of creating a detectable photocurrent response when absorbing just a single photon. Rod photoreceptors initiate under low illumination levels, known as scotopic light levels. Rod cells have peak spectral sensitivities around 498 nm, being completely insensitive to wavelengths above 640 nm. These cells provide very poor spatial resolution, and do not contribute to color vision. Due to this, images appear blurry and monochromatic in dimly lit situations.

A technique in astronomy used for viewing very faint objects, known as averted vision, is evidence of the sensitivity of these photoreceptor cells. In employing averted vision, astronomers use peripheral vision, sometimes coupled with a technique known as scope rocking, where they slightly move the telescope back and forth. These techniques enabled astronomers to view faint objects that they could not resolve when directly foveating on them. Both of these techniques

operate on the fact that the rods are very sensitive to low light levels and to light intensity changes. [8]

Cone cells function in contrast to rod cells, initiating vision under photopic, or bright light levels. Cone cells provide high spatial resolution, resulting in high-acuity color vision. These photoreceptors are vulnerable to damage and cannot regenerate if damage does indeed occur. Typically 1-10 cone cells will supply a ganglion cell, whereas 100 or more rods will supply a ganglion cell. Figure 2.4 illustrates the neural layer of the retina and the corresponding rod and cone photoreceptors.

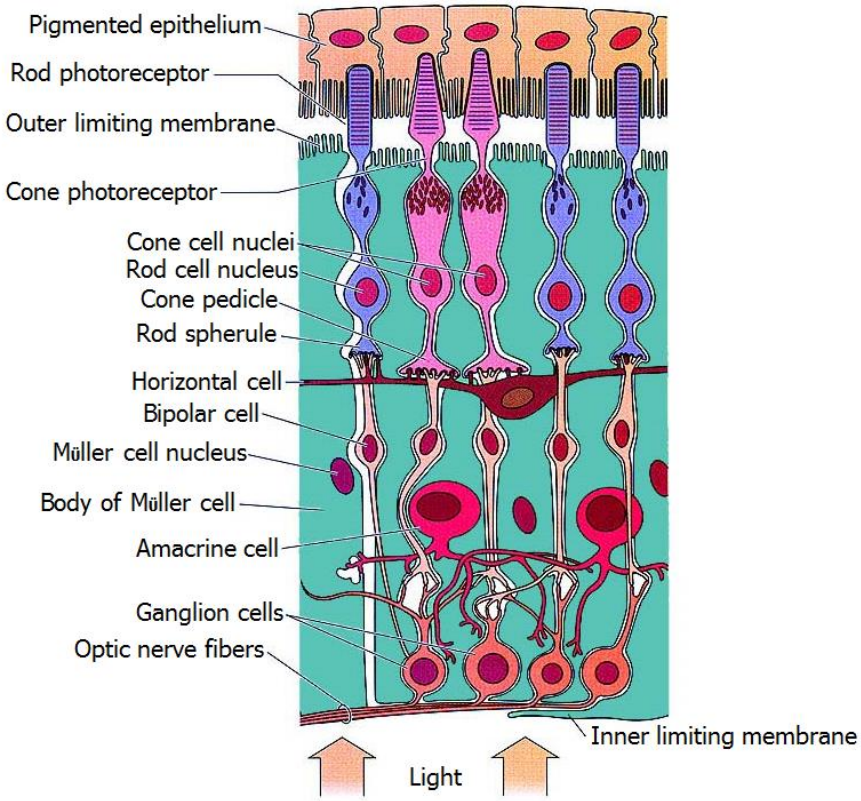

Figure 2.4: Neural Retina Rod and Cone Photoreceptors [9]

The posterior aspect of the retina contains several specialized areas that contribute to central vision. Lying directly along the eye's visual axis is the macula, whose central area is the fovea.

The macula, or macula lutea, is a small (6mm in diameter), highly sensitive part of the retina responsible for detailed central vision. Within the center of the macular region lies the fovea, or fovea centralis, a circular bundle, approximately 0.35mm in diameter, of highly concentrated cone photoreceptors. The fovea is completely devoid of rod photoreceptors. A distribution of rod and cone photoreceptors as a function of eccentricity from the optical axis is shown in Figure 2.5. [10] The fovea contains the highest density of cone photoreceptors in the retina with approximately 199,999/mm^2. The numbers drop to about 50% of that at 500 μm of eccentricity, 1.75^o, from the fovea center and to less than 5% at about 4 mm, 20^o, of eccentricity. [11]

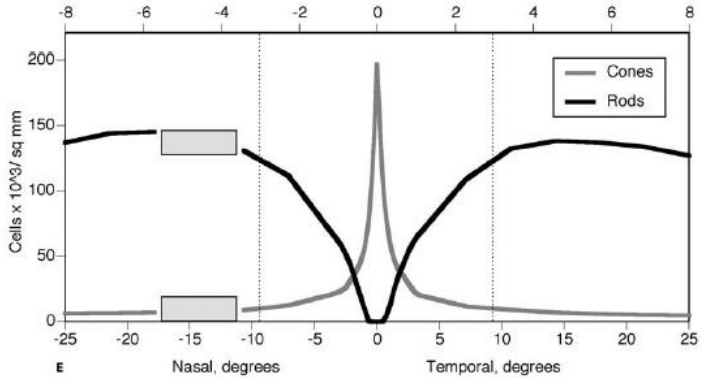

Figure 2.5: Cone and rod density of retinal surface in nasal and temporal retina

Of the photoreceptors of the eye, the rods are more numerous, totaling upwards of 100 million, and are sensitive to monochromatic changes in incident light intensity, but provide poor visual acuity. Rod photoreceptors are more abundant at the periphery of the retina, which gives rise to why individual's color vision, and visual acuity are poor at the periphery of vision, while this area is sensitive to motion (as motion is simply changes in light intensity). Cone cells are far less abundant, totaling nearly 7 million, and are responsible for an individual's perception of color and high visual acuity near the center of vision. [10] Cone photoreceptors may further be divided into three varieties based on their peak spectral sensitivities. These peak sensitivities correspond to

584 nm, 533nm and 437nm wavelength light, which approximate the colors we experience as red, green, and blue respectively. These cones, due to their wavelength sensitivities, are known as L (long), M (medium), and S (short) cones respectively. At the central 100 µm of the fovea lie exclusively red and green cones with an approximate density of 200,000 receptors / mm^2. The macular region and fovea are indicated in Figure 2.6 below, with cone spectral sensitivities indicated in Figure 2.7.

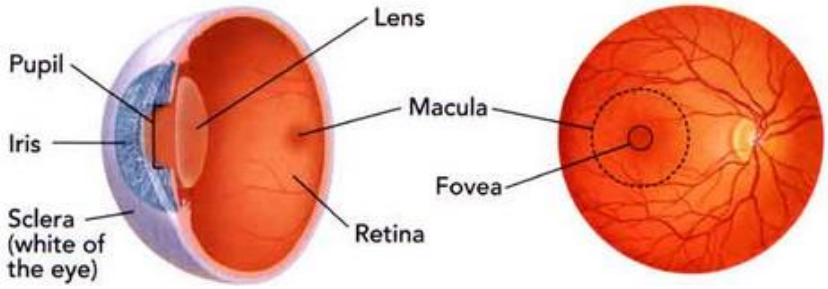

Figure 2.6: Retinal Tunic and Macula [12]

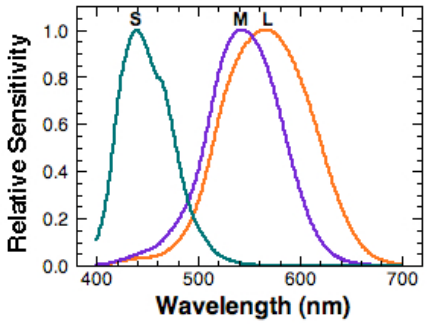

Figure 2.7: S, M, and L cone spectral sensitivities [13]

2.2 Age-Related Macular Degeneration

Age-related Macular Degeneration (AMD or ARMD) is a medical condition affecting an estimated 1.75 million Americans aged 40 years and older, with that number expected to grow to 2.95 million by 2020. [14] AMD is a disease which inhibits the transmission of information being sent from the eye's photoreceptors by means of a dry form (non-exudative AMD), and a wet form (exudative AMD), which causes the macula "degenerate". Due to the fact that the macula, and correspondingly the fovea, have the highest cone density, if information is not being sent from these photoreceptors successfully, individuals may experience a blurry central visual field, or complete central vision loss, resulting in what is known as a central scotoma.

Non-exudative AMD is more common than exudative, and has a slower scotoma growth rate than exudative AMD. Approximately 80 to 90% of AMD cases are of the non-exudative variety. In the dry form drusen, deposits of cellular debris, accumulates between the retinal pigment epithelium and Bruch's membrane as shown in Figure 2.8.

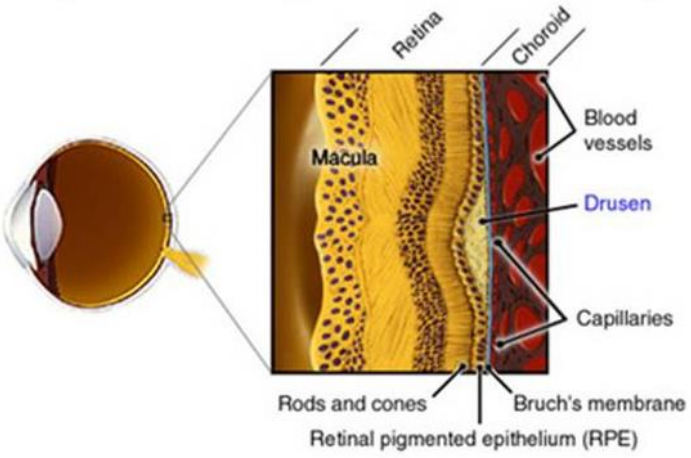

Figure 2.8: Drusen between RPE and Bruch's Membrane [15]

Drusen presents itself in two distinct varieties: hard and soft. Hard drusen are yellowish-white deposits of extracellular debris, commonly appearing small, less than 63 µm in diameter, round and flat. Nearly everyone over the age of 40 has some amount of hard drusen deposits. It should be noted that the presence of hard drusen does not necessarily indicate early onset AMD. Soft drusen is commonly a large, greater than 63 µm in diameter, collection of soft extracellular debris. Soft drusen deposits may coalesce to form confluent drusen. All drusen deposits are associated with minute detachments of the retinal pigment epithelium. These drusen deposits appear in a retinal stereoscopic fundal photograph as bright spots, as indicated in Figure 2.9. The drusen deposits, if large enough, can lead to visual field loss at the location of the deposits.

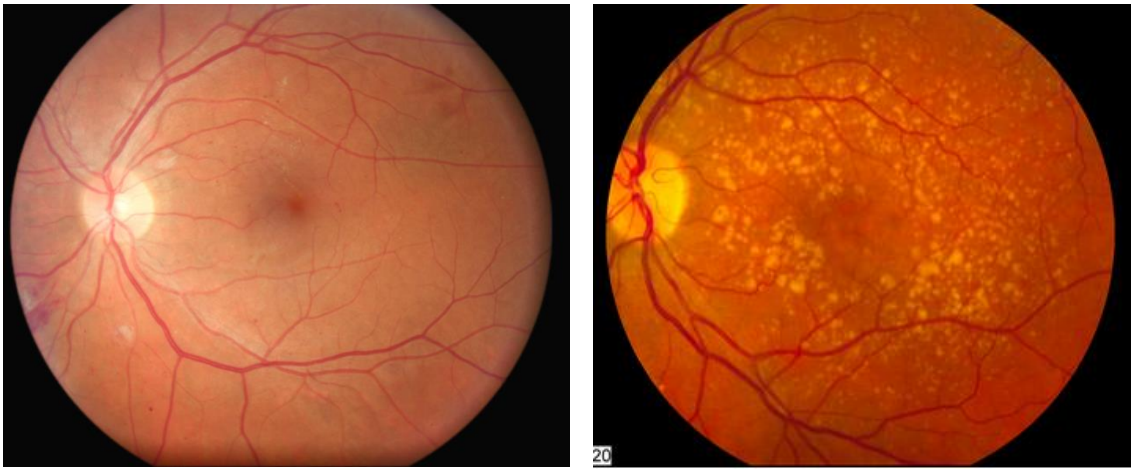

Figure 2.9: Fundus photograph of healthy retina (L), Retina with many spots of drusen accompanying AMD (R)

The advanced, or end stage, form of dry AMD results in what is known as geographic atrophy, or GA. Geographic atrophy refers to a degeneration of a large area of retinal pigment epithelial cells. The atrophy of the RPE causes the next layer of the neural retina, that populated by photoreceptor cells, to atrophy. The fundus photograph in Figure 2.10 shows the effect of GA.

Figure 2.10: Fundus photograph of eye with geographic atrophy [16]

In the exudative, or wet, form of AMD, choroidal neovascular tissue breaks through Bruch's membrane and occupies the space between the RPE and Bruch's membrane, or between the RPE and the photoreceptors themselves. The exudative form of AMD is an aggressive, quickly changing disease that can rapidly result in the loss of an individual's central visual field.

AMD results in a degradation of the individual's central visual field; often times this is depicted as in Figure 2.11. It is important to note that this is an abstraction of the described characteristics of the disease and may not be what is actually perceived by individuals with AMD, due to perceptual completion, and other phenomenon.

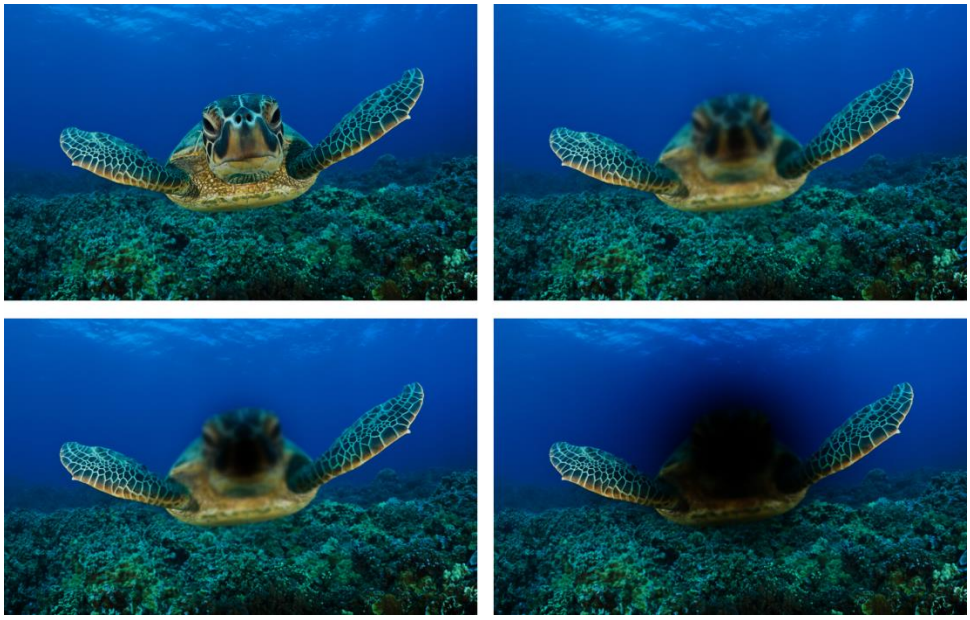

Figure 2.11: Progression of a central scotoma

2.2.1 AMD Detection and Diagnosis

Early stages of AMD typically are asymptomatic and go unnoticed; a comprehensive eye examination is the only certain way to diagnose AMD. A typical examination procedure may include a visual acuity test, a dilated eye examination, Amsler grid testing, a fluorescein angiogram, or optical coherence tomography. [17]

Visual acuity testing is used as a datum to gauge the impact of the disease due to the obvious fact that as cones degenerate in the macula visual acuity decreases. A dilated eye exam is a typical means for an eye care professional to gain a better view of the retina to visually inspect if damage has occurred to the area. Amsler grid testing, where an eye care professional asks the patient to view a grid of equispaced horizontal and vertical lines, is used to detect abnormalities in a person's central visual field. Often time's retinal diseases will cause this grid to appear wavy and

abnormal, a condition known as metamorphopsia. A typical Amsler grid is included in Figure 2.12.

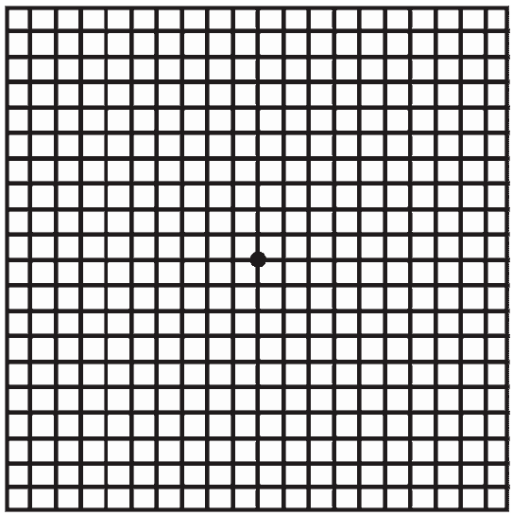

Figure 2.12: Prototypical Amsler Grid [18]

Intravenous Fluorescein angiography is a technique for examining the circulation of the retina and choroid using a fluorescent dye that is intravenously injected into a patient's arm. A special imaging system is then used to create images as the dye moves through the patient's blood stream, which can then detect leaking and pooling defects, as in exudative AMD, or alternatively blood blockages.

Optical coherence tomography, commonly known as OCT, is a technique for obtaining below surface images of opaque materials at microscopic resolutions. OCT essentially consists of interferometry with a low coherence, broad bandwidth light source, using backscattered light. Due to the fact that OCT employs backscattered light, it is often considered to be the optical analog to ultrasound imaging. [19] Figure 2.13, below, illustrates a typical image of the human retina obtained using OCT, and that of one with a detached fovea.

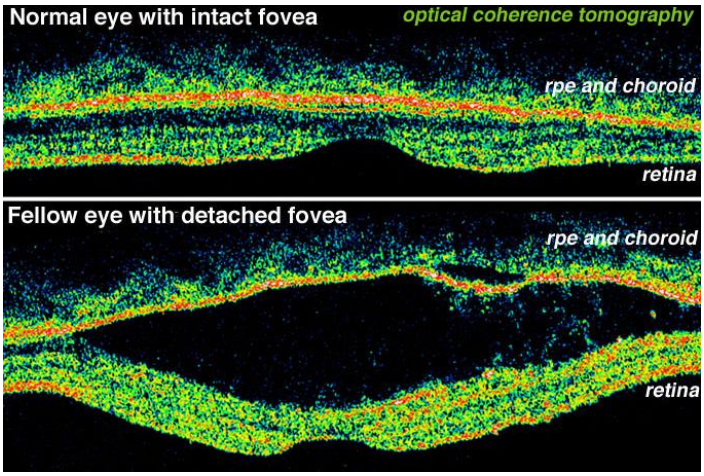

Figure 2.13: OCT of healthy fovea and detached fovea [20]

2.2.2 Eccentric Viewing

Many individuals affected by central scotomas resulting from AMD are no longer capable of using their fovea effectively. In many of these cases, individuals respond by using a fixation locus in the peripheral retina which is used as a pseudofovea to replace the dysfunctional one; such a locus is known as a preferred retinal locus, or PRL, as shown in Figure 2.14. [21] The use of a PRL results in many abnormalities, including position uncertainty, confusion of sequences, deficits in spatial resolution, and abnormal symmetry detection. Position uncertainty exists due to the individual having the tendency to re-foveate to bring the image formed back to the anatomical fovea, as all normally sighted individuals do. There is a correlation between fixation stability and reading speed in subjects who have recently begun eccentric viewing. [22] A significant relationship between visual acuity and PRL eccentricity was found, with increasing eccentricity leading to decreasing visual acuity. [21] To complicate matters, there is proof that individual's may have multiple PRLS which are task dependent. [23] The use of a PRL causes an individual

to employ a different scanning behavior from normally sighted individuals to identify features in an image, often times resulting in altered object and facial recognition. It has been documented that some patients exhibit a re-referencing of the oculomotor system to the PRL, such that they experience themselves fixating straight ahead, when in fact they are fixating with the PRL. As many as 85% of individuals with long standing central visual field defects have been observed to re-reference their oculomotor system this way. [24]

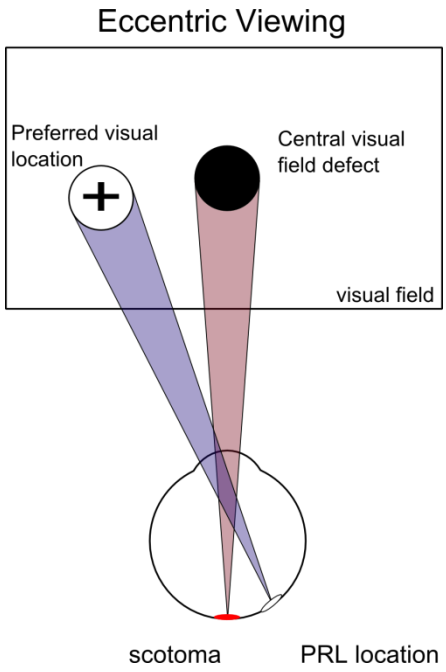

Figure 2.14: Eccentric Viewing

In addition to the phenomenon of oculomotor re-referencing, it has been posited that individual's with AMD may not even be aware of the presence of central visual field scotomas. [25] A common hypothesis within the low vision community is that a process known as perceptual completion occurs for patients with central scotomas, just as it occurs for the physiological blind spot caused by the optic nerve entering the eye by passing through the retina. This process can, very basically, be elucidated by stating that the physiological blind spot occurs due to the fact that no photoreceptors can exist where the optic nerve enters the eye. Primate eyes, however, do not

experience this as spot of vision without any sensory input; the individual's mind does its best job to "fill in the blank". If this is the case with AMD, it could very well be the case that the mind interpolates between sensory input available at the periphery of the scotoma and uses this information to fill in the central visual field defect. It is also within the realm of possibility that the scotoma appears to "sew together" to create the perception that there really is no visual field defect. As opposed to filling in the visual defect with interpolated sensory data, known as perceptual completion, the mind may just remove it or severely distort it, which is known as metamorphopsia. [26]

Further complications from eccentric viewing are the result of artifacts from the Stiles-Crawford effect of the first and second kind. The Stiles-Crawford effect derives from the directional sensitivity of cone photoreceptors. The Stiles-Crawford effect of the first kind is the phenomenon that light entering the eye through the periphery of the pupil is less efficient at stimulating retinal photoreceptors than light that passes through the pupil center. The Stiles-Crawford effect of the second kind is a phenomenon where the observed color of monochromatic light entering through the periphery of the pupil is different compared to the same wavelength light entering through the center of the pupil. [5] Figure 2.15 illustrates the effect of eccentricity of a pencil of light on normalized efficiency of photoreceptor response.

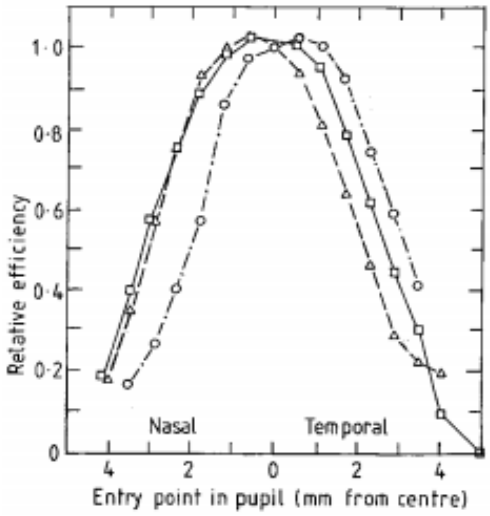

Figure 2.15: Photoreceptor relative efficiency as a function of light entry eccentricity [5]

2.3 **Medical Treatment of AMD**

Although non-exudative AMD is the more common variety of the disease, there are currently no methods to treat or cure this form of AMD. The exudative form of AMD, however, has many current treatment methods; of these, the main goal is to slow or stop the progression of neovascularization within the retina and seal off leaking from these blood vessels. The main types of treatments for wet AMD include anti-angiogenic medications, laser photocoagulation, and photodynamic therapy (PDT).

Anti-angiogenic medications such as Macugen, Lucentis, and Eylea have a primary mechanism of action through binding with, and inhibiting, subtypes of vascular endothelial growth factor (VEGF). VEGF may trigger the growth of blood vessels within the retina, which in turn may leak blood into the eye causing wet AMD. Administered by intravitreal injection at differing intervals, anti-angiogenics may stop, and reverse some of the effects of wet AMD by blocking the

growth of new blood vessels within the eye. Figure 2.16 illustrates the injection of an anti-angiogenic medication, and its intent to stop, and possibly reverse neovascularization. [27]

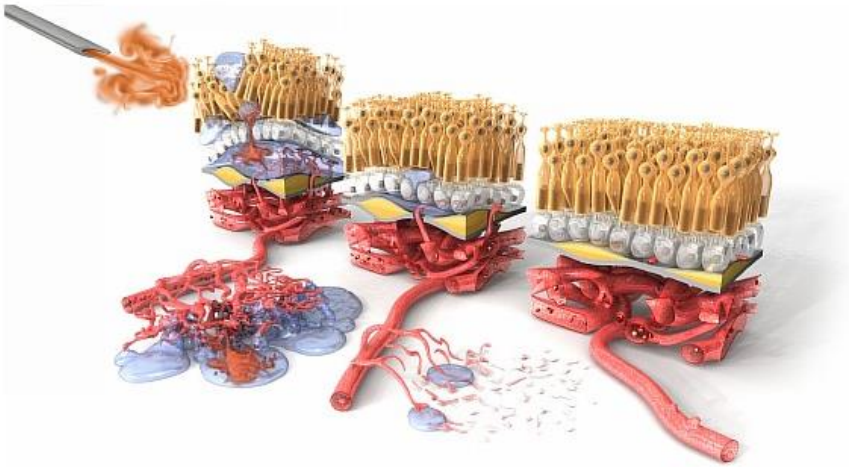

Figure 2.16: anti angiogenic medication [28]

Laser photocoagulation, a type of laser surgery, is a medical procedure that uses a thermal laser to cauterize ocular blood vessels in an attempt to stop neovascular growth and blood leakage, as shown in Figure 2.17. Before the approval of anti-agiogenic medications (circa 2004), photocoagulation was the main treatment method for exudative AMD. However, due to the fact that damage to nearby tissue is inevitable during the process due to coagulation necrosis, other treatments are typically sought out as a first course of action. [29]

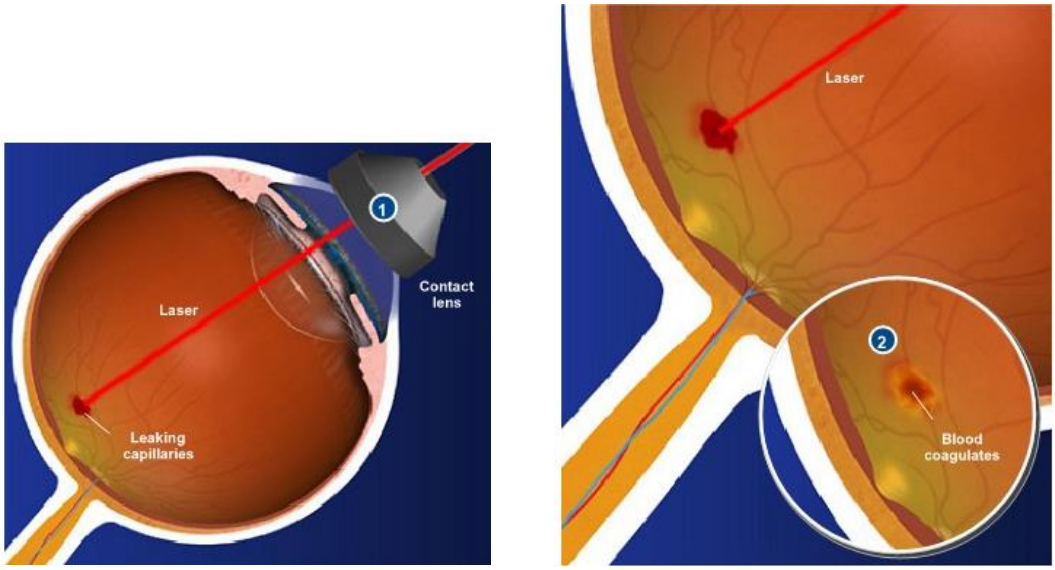

Figure 2.17: Focal Laser Photocoagulation [29]

Photodynamic therapy is a treatment process in which verteporfin, marketed as Visudyne, a light sensitive medication, is injected into an individual's bloodstream. The medication collects in the abnormal and leaking blood vessels in the macular region, at which point 693 nm wavelength (red) laser light is shown into the patient's eye. The medication reacts to non-thermal laser light by creating reactive oxygen radicals, which result in local damage to the endothelium, in turn causing a blockage of the abnormal blood vessels. [30]

Another medical treatment to provide symptomatic relief, as opposed to treating the disease directly as the interventions above do, is the Intraocular Lens for Visually Impaired Patients (IOL VIP). IOL VIP relies on the surgical implantation of an intraocular lens system that both magnifies and translates images formed on the retina using a Galilean telescope created by the implanted intraocular lenses. By appropriately arranging the lenses, it is possible to redirect the location of image formation to a different portion of the retina, other than the affected fovea. A schematic of the implanted intraocular lenses is shown in Figure 2.18; to date, very few studies have been performed on the efficacy of this intervention. The main pilot study on this operation

concluded that of 35 patients, all showed an improvement in visual acuity, with a mean postoperative best corrected visual acuity (BCVA) of 0.77 LogMAR (logarithm of the minimum angle of resolution), with a preoperative mean BCVA of 1.28. Additionally, it was noted that reading distance improved in all cases. [31]

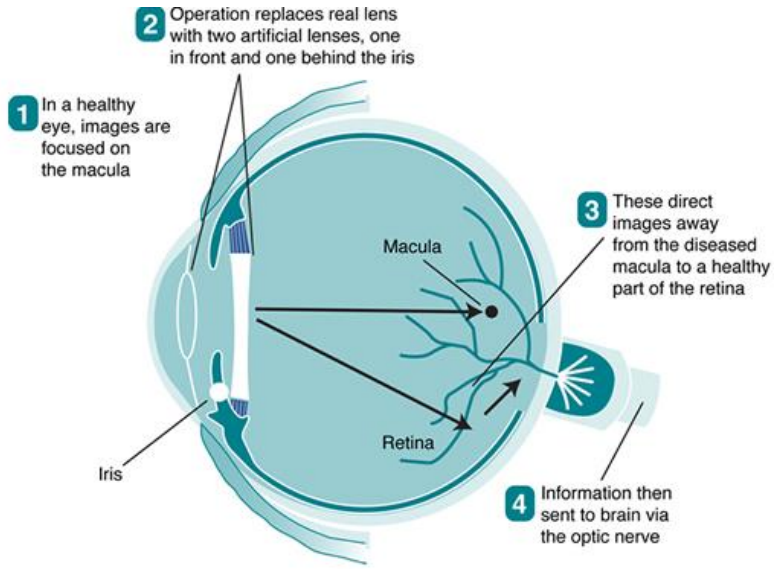

Figure 2.18: IOL-VIP Procedure [32]

Similar to the IOL-VIP procedure is that marketed by CentraSight, which uses VisionCare Ophthalmic Technology's Implantable Telescope Technology. As the aforementioned procedure's name alludes, this technique also operates with an implantable telescope, as shown in Figure 2.19. [33] In contrast to the IOL-VIP procedure, no image relocation is performed, only a 2.2x or 2.7x magnification is induced in an attempt to reduce the perceived size of the scotoma to the patient.

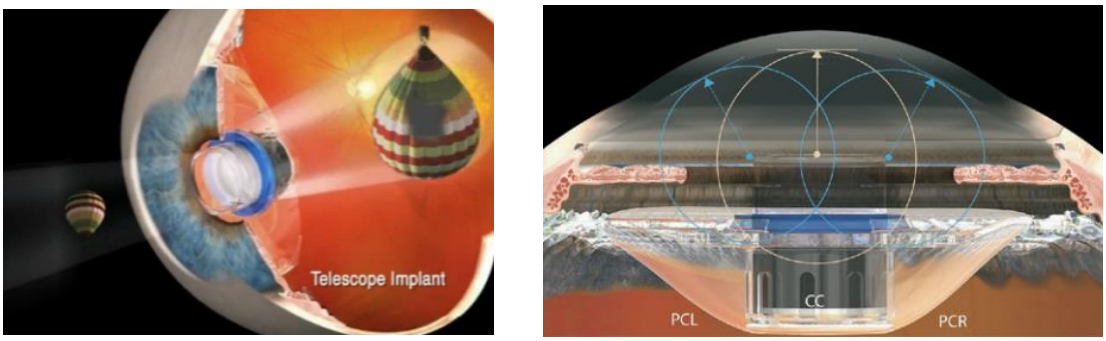

Figure 2.19: Implantable Telescope [34] [35]

This procedure involves the patient learning to use the implanted eye for central vision, with the other eye being used for peripheral vision. Hudson et al indicate that the mean improvement in BCVA for patients two years after implantation is 3.6 lines on an ETDRS (early treatment diabetic retinopathy study) chart. [35]

2.4 **Low Vision Aids for Macular Degeneration**

In addition to the aforementioned medical interventions, a number of coping methods have been created to help improve the quality of life of individuals living with AMD. Of these methods, the most common form is in enhanced magnification of text while reading, utilizing the theory that magnifying an image will reduce the size of the patient's perceived scotoma relative to objects in the patient's central field of view. Simplistically this means that if the text is enlarged and an individual has a loss of central vision, a smaller portion of the characters will be lost as the text size increases. Often time's patients will meet with low vision occupational therapists to assign magnification aids ranging from hand held magnifying glasses to CCTVs that magnify the text of items placed on their reading platforms. CCTVS such as the MagniSIGHT Explorer Classic CCTV device for assisting AMD patients, having a retail value of $2495.00, are shown in Figure

2.20, below. [36] Desk mounted CCTVs have the benefit of utilizing a translating stage to smoothly change the camera position relative to the text being read.

Figure 2.20: Magnisight CCTV

In addition to CCTV magnifiers, there are portable electronic magnifiers that plug into a laptop via USB or VGA, such as the Transformer portable electronic magnifier shown in Figure 2.21. These magnifiers have the benefit of being much more mobile, typically weighing less than 3 pounds, can be plugged into any existing computer, and can digitally magnify images up to 30x. Furthermore, since the user must provide their own display screen, portable electronic magnifiers are typically cheaper than desk mounted ones, with the Transformer retailing for $1999.95. [37]

Figure 2.21: Transformer portable electronic magnifier

Some commercially available devices attempt to assist AMD patients by performing retinal image relocation by means of ophthalmic prisms. The notion is that if the image being formed on the fovea is lost due to a central scotoma, prismatically translating the image formed to a healthy area of the retina will allow the patient to see the image successfully. Some devices that operate using this principle include the Gottlieb Visual Field Awareness System (VFAS) [38], where a prism is fit on a spectacle lens corresponding to the affected eye, the Chadwick Hemianopsia Lens (INWave lens) [39], where the prism is incorporated into the lens itself, and the Peli Lens, which uses two Fresnel press on prisms above and below the pupil; these devices are shown in Figure 2.22. These aforementioned devices are primarily marketed for individuals with hemianopsia, a condition in which half of the visual field suffers decreased function or blindness, typically on one side of the vertical midline, but operate on the same principle.

Figure 2.22: Gottlieb visual field awareness system (left), Chadwick hemianopsia lens (middle), Peli lens (right)

Macular Eyewear markets a device that is used to adjustably magnify an image, as well as employs prism to assist in reducing the vergence necessary for the eyes to see the highly magnified image, thereby reducing eye strain. [40] The prism enables reading material to be held at a closer distance, due to the fact that it reduces the required vergence, in this case convergence, of the eyes. Logically, the higher the magnification of an image, the closer the image must be held to the eyes, which for binocular viewing, means the eyes must turn in to a large degree,

which the prism counteracts. These eye glasses are sold for $130.00 and are shown in Figure 2.23.

Figure 2.23: macular eye wear

Designs for Vision inc. markets a product known as E-Scoop glasses, clip on glasses to go over an individual's prescription eye glasses, that incorporate a yellow tint to filter out blue light (which may be responsible for greater light diffusion in cases of cloudy ocular media), base in prism ranging from 4 Δ to 8 Δ to alleviate eye strain from the high vergence necessary to view highly magnified objects, and enhance magnification of images formed on the retina. [41] Note that the aforementioned Δ designates units of prism diopters, defined as the ability of an ophthalmic prism to laterally translate an image one centimeter at a distance of one meter. Therefore, a 4 Δ prism would translate a point 4 centimeters in the specified base direction, if formed on a surface one meter away. The E-scoop clip on lenses are shown in Figure 2.24.

Figure 2.24: E-scoop clip-on lenses

A fiberscope low-vision reading aid has been proposed by Pelli, Legge and Schleske, whereby a portable, low-resolution fiberscope provides magnification up to 40x (160 diopters), as shown in Figure 2.25. [42] This reading aid has the downfall of only having an array of 125x125 fibers, making the image displayed to the user very low resolution. Benefits of such a device over typical hand held magnifiers include that it allows for a natural reading posture, as high magnification hand held magnifiers must be held within a few inches of the individual's eye, and typically result in postural issues. However, Legge found that visual requirements for effective reading are a four-character visual field and a 2 cycle / character resolution, with which the fiberscope was designed. This serves as a good example that devices for low vision need not achieve high resolution. Engineers must become comfortable with this as the images produced by the developed device may look blurry to them, but will not appear different to individuals with low vision. Further considerations are the dexterity required to operate the device, as rather precise movements at the input of the device are required with such high magnifications. At the end of the trial, the experimenters determined that the design should allow for reading at a rate of 67 words per minute. Ultimately, the fiberscope was discontinued after being developed by an outside engineering company that developed consumer versions that were overly robust, causing for unnatural reading postures and inflexibility with the optical fibers. [43]

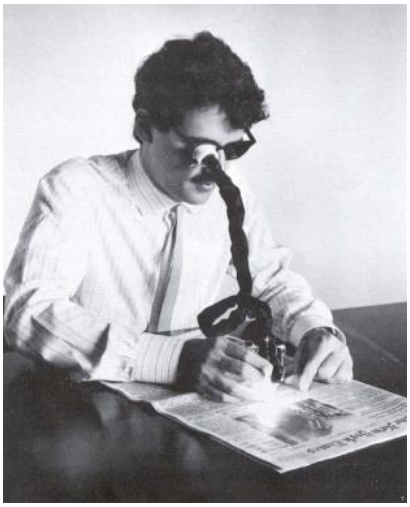

Figure 2.25: Fiberscope low vision aid

Further low vision aides for macular degeneration include spectacle miniature telescopes (SMTs), as shown in Figure 2.26, whose mechanism of action is identical to that of the implantable telescopes described above, with the obvious exception that these telescopes are spectacle mounted. The benefit of having an implanted telescope instead of a spectacle mounted one is that fixation stability is enhanced due to the telescope rotating with the eye. Further benefits of SMTs are that reading viewing distance is often increased compared to other magnification devices. [44]

Figure 2.26: Spectacle Miniature Telescope [44]

Hand held optical magnifying glasses are the classical approach, and often the first device used for assisting reading for AMD patients. As in the other magnification based approaches, the

larger an image is made, less of it will be lost behind the scotoma; a hand held optical magnifying glass is the easiest way to achieve this. Typically patients will have multiple magnifying glasses for differing tasks, as shown in Figure 2.27. The magnifying glasses often incorporate a standoff that correctly sets the height the glass should be held from the reading surface, at which point it is the user who must lean in close to the magnifying glass, often positioning their eye inches from the refractive surface.

Figure 2.27: Large variety of hand held optical magnifying glasses [44]

Within the past few decades a large amount of work has been done in the area of Electronic Vision Enhancement Systems (EVES) for the visually impaired. A limiting factor of EVES, that is slowly diminishing, is that due to limited technology and computational power. Furthermore, EVES have historically not been very portable, and are more expensive than classical optical aids. [45] EVES technology mainly focuses on enhanced magnification, altering of field-of-view, contrast enhancement, and image enhancement. EVES may be desk mounted, in the case of CCTV devices like that shown above, hand held, or head mounted.

When CCTVS are used it has been shown that reading speed increases as working distance increases, but reading speed decreases as both effective and linear magnification are increased. [46] Alternatively, it has been concluded that reading speed increases with increases in

magnification, up to some maximal value, followed by a plateau or decrease with further increases; Legge calls this the critical print size for eccentric reading. [47] [48] As reading eccentricity increases, reading speed decreases, and critical print size increases. Of additional concern, when dealing with eccentric reading, is the notion of window size. It has been shown that a maximum of approximately four characters may be resolved well when eccentrically reading. [49] In terms of optical transfer functions, readers with central visual field defects lose sensitivity to spatial frequencies higher than 10 cycles per degree as a result of parafoveal fixation. [45] Increased magnification of text causes a shift to lower spatial frequencies, which are significantly more visible, but have the detriment of decreased field of view.

Reading performance with an EVES has been proven to be related to contrast sensitivity. [46] Furthermore, there have been numerous records of individuals preferring contrast polarity reversal (white on black print). [50] This preference may be due to many reasons including cloudy ocular media, glare reduction and less noticeable picture flicker than conventional contrast polarity. [51]

Image enhancement via digital image processing can greatly augment the quality of an image formed on the retina of patients with low vision. Digital image processing techniques can be used to alter contrast, luminance, change color spaces, magnify or warp images, especially in ways that are unachievable by conventional optical devices. A simple head mounted display that is capable of simple image processing, such as color inversion and magnification, is the Vuzix Sightmate, which was launched in 2007 and retailed for $1999.00. [52] The Sightmate was largely unsuccessful due to the limited number of features and cost, although it was more portable than a standard CCTV; the Vuzix Sightmate is shown in Figure 2.28.

Figure 2.28: Vuzix Sightmate [53]

More experimental devices that perform image enhancement may be described as ones utilizing image warping (re-mapping) algorithms. Although no commercially available devices such as these exist, a handful of articles from the late 1980's describe using the Programmable Video Image Remapper at NASA's Johnson Space Center. A certain subset of these image remapping algorithms was quickly tested for low vision, but ultimately testing was abandoned. [54] In early testing of static images that were remapped, patients indicated that certain remapped images "looked better". [55] Although this is far from a concrete value such as BCVA, it sheds light on the fact that remapping is a possible means to rehabilitate individuals with central vision loss due to AMD.

2.4.1 Prismatic Image Relocation for AMD

A historically accepted means to treat some of the symptoms of AMD within the medical community has been to prescribe an ophthalmic prism that translates the image formed on the fovea to a parafoveal region that is undamaged. There are numerous publications examining the effectiveness of such an intervention, but it has been revealed that care must be taken when evaluating the claims made by these publications. There have been many metrics proposed to evaluate the meaningfulness of claims in medical journals, of which the Downs and Black

Quality Assessment Index has been used to compare articles. [56] The Downs and Black Quality Assessment Index consists of a 27 question assessment used to measure the methodological quality of studies of health care interventions.

Hooper et al. used the Downs and Black index to evaluate rehabilitation methods for AMD, concluding that, of the articles reviewed in favor of prismatic image relocation, none were of good quality. [57] The authors concluded that image relocation with prisms as a successful treatment option was supported by weak evidence from two studies of fair quality on the Downs and Black scale [58] [59], and one poor randomized controlled trial on the Downs and Black scale [60]. Furthermore, the authors concluded that strong evidence from one excellent randomized study [61] indicated that prismatic image relocation is no more effective than conventional glasses. Of all the articles reviewed, selection bias is severe, with the exception of one [61]. [57]

When a Downs and Black quality assessment index was assigned to other articles relating to the efficacy of prismatic image relocation, one poor study was found in favor of prismatic image relocation [62], and one acceptable study in favor of prismatic image relocation was identified [63]. The general consensus within the medical community therefore is a wash between image relocation via prisms being acceptable, while in the psychology community the general consensus appears to be that prismatic image relocation is not an acceptable form of treatment [43], with concerns that individuals will simply foveate at a different location to accommodate the translation of image formation. It would therefore be required for such a therapy to be dynamic, and react to the individual's foveal location.

With the above Downs and Black quality assessment treatment, it is therefore believed that prismatic image relocation for the treatment of AMD is not an avenue worth pursuing.

2.5 **Related Work**

Everingham, Thomas and Troscianko have described a head mounted mobility aid for low vision that operates using scene classification techniques. [64] [65] In their work, a head mounted display is used in conjunction with software that segments images and fills them in with solid colors, as shown in Figure 2.29. Object segmentation is performed via edge detection. By performing the above segmentation and filling in, high spatial frequency objects are removed leaving the scene much less confusing for individuals with low spatial bandwidth capabilities.

Figure 2.29: Scene Classification and Filling in approach

Prothero [66] demonstrated a way to use a display in which virtual images are overlaid over a real scene to provide cues to attempt to provide enhanced mobility of patients with akinesia due to Parkinson's disease.

Massof and Rickman [67] describe their low vision enhancement system, LVIS, which utilizes forward facing cameras mounted on a head mounted display that magnifies video feed captured by the cameras. The HMD system, shown in Figure 2.30, weighed 800 grams and was first available in 1994 with a retail value of $5000.00.

Figure 2.30: LVIS HMD System

Peli [68] used a head mounted display with binary monitors to display images with variable brightness, contrast, and magnification. Peli [69] has further studied the influence of vision multiplexing as an approach to rehabilitating visual disorders. Vision multiplexing consists of sending multiple images to the eye that in some way compensate for information that would normally be lost. Examples of this include bioptic telescopes which provide temporal and bi-ocular multiplexing, micro telescopes providing spatial multiplexing, and minifying augmented view algorithms to provide spatial multiplexing for compensation of loss of peripheral vision. Peli and Lou [70] have employed an augmented vision device that utilizes vision multiplexing for individuals with peripheral vision impairments.

Goodrich and Zwern [71] used a commercial HMD that was capable of delivering enhanced contrast and magnifying images presented to the wearer. Wolffsohn [72] used edge detection filters, such as a Sobel filter and Canny edge detector, to overlay a high contrast image outline over television images to enhance perceptibility of differing objects in low vision patients, as shown in Figure 2.31.

Figure 2.31: Normal image (L), Sobel edge detection (M), Wolffsohn edge detection and enhancement approach (R)

Vargas-Martin et al. [73] have described a head mounted display system coupled with a PC that enhances images with digital zoom and edge enhancement via edge detection algorithms.

Atabany and Degenaar [74] utilized a scene classification approach that also simplified the scene using smoothing kernels as shown in Figure 2.32. Scene classification is again performed using edge detector kernals such as a sobel filter, with smoothing performed by operations akin to gaussian convolution.

Figure 2.32: Atabany approach to scene classification and simplification

The above Figure illustrates, from left to right, the Atabany approach to scene classification and simplification using edge enhancement alone, edge enhancement and Gaussian filtering, edge enhancement and median filtering, and edge enhancement and anisotropic diffusion filtering.

Juday et al. [75] [76] [77] have described an approach that utilizes the Programmable Remapper at NASA's Johnson Space Center to remap images in a manner that compensates for central visual field defects. These remapping algorithms include a conformal fourth-degree transcendental polynomial map to compensate for maculopathy, a parametric function to compensate for retinitis pigmentosa, two quasi-conformal mappings to compensate for central visual field defects, conformal annular and conformal complex arcsine warpings to compensate for central visual field defects, and a handful of mappings that vertically translate image data to

avoid central visual field defects in accordance to a cosine, Gaussian or elliptical function, as shown in Figure 2.33.

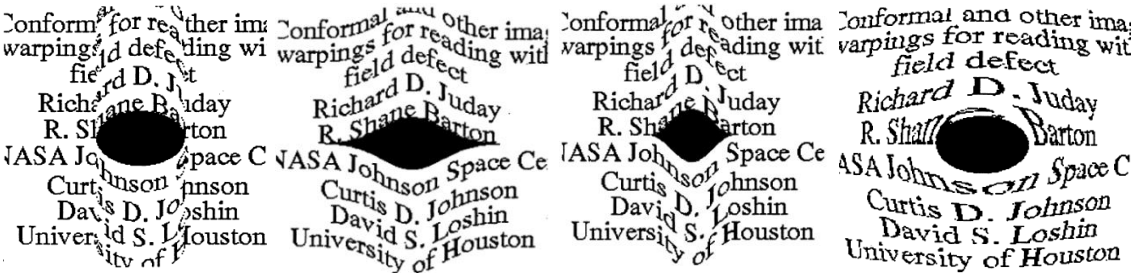

Figure 2.33: Juday image remappings, from left to right: Column Elliptical Bump, Gaussian bump, Column cosine bump, conformal annular region warp

2.6 **Refractive Errors of the Eye**

Although AMD is the major disease being designed around, other conditions of the human eye must be taken into consideration. Of these, refractive errors such as presbyopia, myopia, hyperopia and astigmatism must be considered. Presbyopia, myopia and hyperopia are related to the ability of the eye to carry out accommodation, the process by which the vertebrate eye changes optical power. Accommodation is performed by altering the shape of the eye's crystalline lens to form a sharp image on the retina as the distance to that object varies. Accommodation acts as a reflex, whose mechanism of change is an altered zonular tension induced by ciliary muscle contractions. [1]

Accommodation is measured in units of diopters, which are a unit of measure of the optical power of a lens, equal to the reciprocal of the focal length measured in meters. Individuals are typically born with the ability to achieve accommodation equal to a change of 20 diopters at birth, which gradually declines during the course of one's life due to loss of elasticity of the eye's

crystalline lens, and eventually settles around 1 diopter by the age of 60. These respective dioptric accommodation powers correspond to the ability to focus on objects 50mm (1/20 m) away and 1 meter (1/1 m) away respectively. The progressive inability of the eye to focus on near objects as an individual ages is known as presbyopia. [78]

Related to presbyopia, hyperopia, also called farsightedness, is the inability of the eye to focus on objects relatively close to the individual due to the anatomical shape of the eye causing images to be formed behind (posteriorly to) the retina. Hyperopia is often the result of the eyeball itself being too "short" for the amount of refraction within the eye, causing images to be formed behind the retina.

The opposite of hyperopia is known as myopia, or nearsightedness, and is the inability of the eye to focus on objects relatively far from the individual. This is the result of faraway objects forming in front of (anterior to) the retina, due to the eye being too "long" given the amount of refraction present in the eye.

Myopia and hyperopia are commonly corrected with the use of corrective lenses, or contact lenses, which compensate for the excessive positive number of diopters, or negative number of diopters, of the eye corresponding to myopia and hyperopia respectively. Myopia and hyperopia prescriptions are measured in diopters, and typically vary between 1.00 and 3.00 diopters for "low degree" forms.

Like myopia and hyperopia, presbyopia may also be compensated for with corrective lenses commonly known as reading glasses. Typical corrective lenses for use with presbyopia will have dioptric powers ranging from +1.00 to +4.00 diopters, but are only necessary when attempting to image objects that are close to the wearer, such as when reading. Figure 2.34 illustrates a simple ray tracing of images formed on the retina for the aforementioned refractive errors.

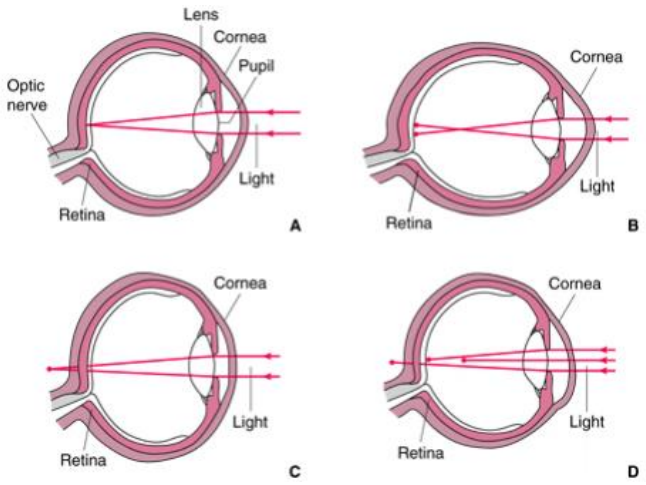

Figure 2.34: Refractive Errors (A): Emmetropic Eye, (B): Myopic Eye, (C): Hyperopic Eye, (D): Astigmatic Eye [79]

Unrelated to the refractive power of the human eye, astigmatism, so called because it causes the optical aberration known as astigmatism, is a disorder where rays that propagate in perpendicular planes have distinctly different foci. In terms of the human eye, this is the inability of the eye to focus a point object into a sharp image, focused on the retina, due to an irregular curvature of the cornea or crystalline lens. In what is known as regular astigmatism, the condition is often compensated for by prescription of toric corrective lenses, which are characterized by two radii of differing lengths. In the case of irregular astigmatism, which is often attributable to scarring of the cornea or optical scattering in the crystalline lens, corrective contact lenses are prescribed, as regular eye glasses cannot compensate for such irregularities. [78] Astigmatism correction complicates corrective lens design as more parameters are needed than accounted for in the simple thick lens maker's equation, which is the common method of designing corrective lenses, as indicated equation 2.1.

$$P = \frac{1}{f} = (n-1)\left[\frac{1}{R_1} - \frac{1}{R_2} + \frac{(n-1)d}{nR_1R_2}\right] \tag{2.1}$$

In the above thick lens maker's equation, P is the power of the lens in diopters, f is the focal length of the lens, n is the index of refraction of the lens material (assumed to be a constant but in actuality is a function of the frequency of the electromagnetic wave passing through it), R_1 is the radius of curvature of the lens surface closest to the light source, R_2 is the radius of curvature of the lens surface furthest from the light source, and d is the thickness of the lens along the lens axis.

The above conditions are important because they too must be taken into consideration when creating a device to help compensate for AMD. An ideal device would be capable of compensating for the above conditions, as well as assisting individuals cope with AMD, as many individuals with AMD have one of the above eye conditions as well.

2.7 **Optical Aberrations**

Optical aberrations are departures in performance of a designed optical system from that predicted by paraxial optics. Paraxial optics, so called because it utilizes ray tracing of paraxial pencils of light, effectively linearizes the optical system using small angle approximations. Such an approximation is used in Gaussian optics and many ray tracing algorithms. Mathematically, paraxial approximations are those when a first, or sometimes third, order approximation of a Tayler series expansion is performed to linearize the nonlinear optical system described by Snell's law, as indicated in equation 2.2. Most importantly, small angle assumptions allows for the following linearizations: $\sin\theta \approx \theta$, $\tan\theta \approx \theta$, and $\cos\theta \approx 1$.

$$\frac{\sin\theta_1}{\sin\theta_2} = \frac{\theta_1 - \frac{{\theta_1}^3}{3!} + \frac{{\theta_1}^5}{5!} - \frac{{\theta_1}^7}{7!} \cdots}{\theta_2 - \frac{{\theta_2}^3}{3!} + \frac{{\theta_2}^5}{5!} - \frac{{\theta_2}^7}{7!} \cdots} = \frac{v_1}{v_2} = \frac{n_2}{n_1} \approx \frac{\theta_1}{\theta_2} \tag{2.2}$$

In the above equation, θ_1 is the angle of incidence of light, θ_2 is the angle of refraction, v_1 is the velocity of light propagation in the first medium, v_2 is the velocity of light propagation in the second medium, and n_1 and n_2 are the indices of refraction for the first and second medium respectively. Figure 2.35 illustrates Snell's law.

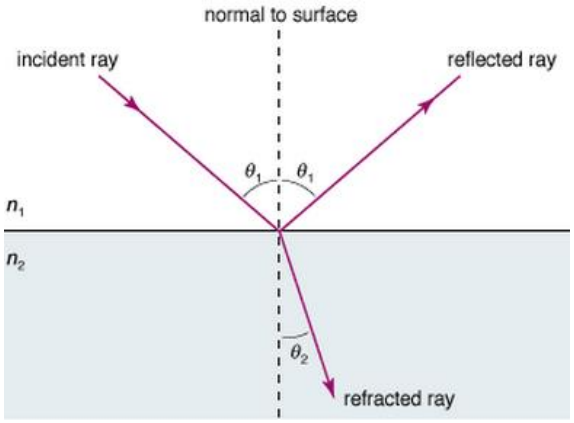

Figure 2.35: Snell's Law [80]

The aberrations that result from the above approximations are known as distortion, spherical aberration, coma, astigmatism, curvature, chromatic aberration, defocus and tilt.

Of special importance to this project are the notions of defocus, distortion, astigmatism, and chromatic aberration. Defocus is the most simple of these aberrations, and is simply the term used to describe when an image appears out of focus. This optical aberration is the result of translations along the optical axis away from the imaging plane of best focus, as is the case in hyperopia and myopia. Such concerns come into play in the human eye due to refractive errors, but also when adjusting the f-number of a camera lens used to create images in the final device, and also when the wearer's eyes are located at a variable distance from the eye tubes of the HMD.

Distortion, a deviation from an expected rectilinear image formed on an imaging surface, typically appears as a radially symmetric aberration as the result of using zoom lenses in imaging systems. The most common forms of distortion are barrel distortion and pincushion distortion, as shown in the Figure 2.36.

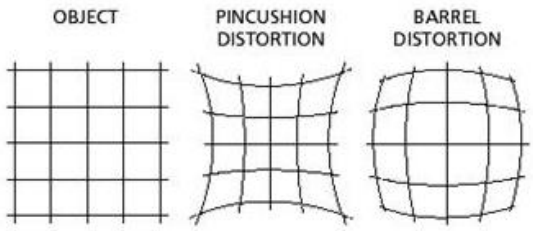

Figure 2.36: Pincushion and Barrel Distortion [81]

Barrel distortion, which is named due to the appearance of a flat object being mapped around the surface of a barrel, is apparent in fisheye and wide angle lenses. This type of distortion can be corrected for by utilizing commands within OpenCV where a checkerboard pattern is used as a rectilinear map to fit radial symmetric distortion parameters. These parameters are then inverted to correct the incoming images. The opposite of barrel distortion, where images appear expanded at the center of the image, is pincushion distortion, where images appear compressed in the center of the image. This type of distortion is typically present at the telephoto end of a zoom lens' spectrum of zoom. These distortions will likely need to be compensated for when capturing video from an environment using wide angle lenses.

Astigmatism is the optical aberration that results from rays propagating in two planes of differing foci. Astigmatism results in images being formed at differing focal points depending upon the point where they passed through a refractive surface. This aberration is present in many man-made optical systems with malformed refractive surfaces, but also appears in ophthalmic astigmatism, where the degree of refraction in the tangential and sagittal meridians of the eye is

different. Ophthalmic astigmatism is typically the result of an aspherical cornea; this may be corrected using toric eye glasses, contact lenses, or refractive surgery. Astigmatism will result in a blurring of images being formed due to portions of them being out of focus; the circle describing the focal plane of best imaging is known as the circle of least confusion. Astigmatic aberrations are shown in Figure 2.37 below.

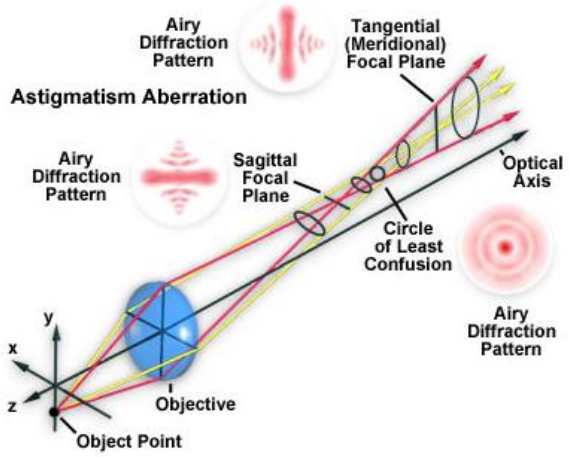

Figure 2.37: Astigmatism Aberration [82]

Chromatic aberration is the phenomenon where refractive elements fail to focus differing wavelength light at the same point. There are two manifestations of chromatic aberration, namely longitudinal and lateral chromatic aberration. Longitudinal chromatic aberration occurs when light passing through a refractive surface results in differing focal lengths dependent upon wavelength. If chromatic light is obliquely incident to a refractive surface, or if that surface is an ophthalmic prism, lateral chromatic aberration is likely to occur. This is a situation where the focal points of differing wavelength light lie on the same plane, but are refracted by differing amounts, as shown in Figure 2.38.

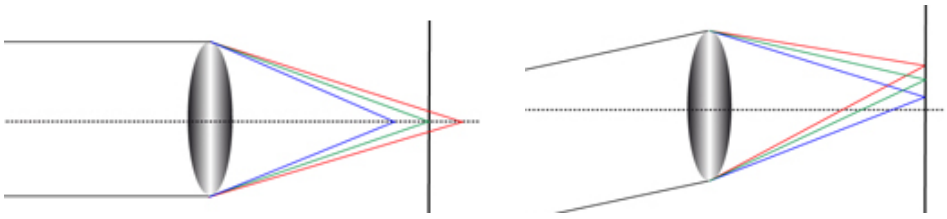

Figure 2.38: Longitudinal Chromatic Aberration (L), Lateral Chromatic Aberration (R) [83]

Longitudinal chromatic aberration is typically characterized as the dioptric difference between blue wavelength light, F_f, and red wavelength light, F_c. A formulization of this is as follows:

$$longitudinal\ CA = F_F - F_C \tag{2.3}$$

It is important to note here that all optical media have indices of refraction that are wavelength dependent; the nominal value specified in look up tables, unless otherwise noted, corresponds to that of yellow wavelength light. A more rigorous way of defining the longitudinal chromatic aberration resulting from a refractive surface is the dispersive power, which may be derived from the thin lens maker's equation, indicated below in equation 2.4.

$$dispersive\ power = \omega = \frac{n_F - n_C}{n_D - 1} \tag{2.4}$$

In the above equation, n is the wavelength dependent index of refraction, with subscripts F, C, and D denoting wavelengths corresponding to the Fraunhofer F, C, and D spectral lines. These lines coincide with blue, 486.1 nm, red, 656.3 nm, and yellow, 589.3 nm, wavelength light respectively.

The inverse of the dispersive power of a transparent material, ω, is known as the Abbe number. The Abbe number, V_d, is a universal measure of a material's dispersion in relation to its refractive indices, and is indicated in equation 2.5 below.

$$V_d = \frac{n_D - 1}{n_F - n_C} \tag{2.5}$$

The Abbe number is an important parameter in designing ophthalmic prisms used to relocate images, as discussed in later sections, and in designing achromatic doublet lenses to compensate for chromatic aberration. [84]

Similar to the difference in indices of refraction for red and blue light to characterize longitudinal chromatic aberration, lateral chromatic aberration may be described by the difference in prismatic deviation between blue and red wavelength light. Lateral chromatic aberration, lateral CA, specified in prism diopters, Δ, can be calculated with equation 2.6.

$$Lateral\ CA = \frac{prism}{V_d} \tag{2.6}$$

In the above equation, prism is either specified in prism diopters, if the refractive surface is an ophthalmic prism, or decentration of a refractive lens, in centimeters, multiplied by the power of the lens. The lateral chromatic aberration directly impacts any kind of prismatic retinal image relocation, as discussed in further sections. Meslin and Obrecht have predicted degradation in Snellen visual acuity as a result of lateral CA, which is tabulated in Table 2.2. [85]

Table 2.2: Effect of Lateral Chromatic Aberrations on Snellen Visual Acuity

LCA	VA
0.05 Δ	20/21
0.10 Δ	20/22
0.15 Δ	20/24
0.20 Δ	20/26
0.25 Δ	20/28
0.30 Δ	20/31
0.35 Δ	20/34
0.40 Δ	20/39
0.45 Δ	20/44
0.50 Δ	20/51
0.55 Δ	20/60
0.60 Δ	20/75

Chapter 3

A Digital Image Warping Prosthesis for AMD

3.1 **Design Goals**

Initial design goals were to improve upon the notion of prismatic image relocation to force eccentric viewing for AMD patients, while maintaining a forward gaze. In such a design, image relocation to a prescribed, or user defined, PRL would be adjustable. As the project progressed from incipient stages, the design goal of dynamically following the user's pupil location was added. Ideally, such a system would be light weight, robust, capable of being worn for long periods of time, would not invoke adverse side effects that would counterbalance the benefits of the device, and successfully relocate images to undamaged regions of the patient's retina coinciding with their PRL. Furthermore, the ability to correct for common refractive errors would be necessary. Success would be evaluated based on experimental evidence suggesting an increased monocular reading rate, and/or visual acuity, as increased reading capability is the main goal sought after during occupational therapy for AMD.

3.2 Methodology Selection

At the incipient stages of the project nine design routes were considered with one finally being chosen. These distinct design routes and mechanisms of action are discussed in the follow subsections.

3.2.1 Adjustable Prism Spectacle

The most basic, and most previously investigated option, is that of prismatic image relocation. In the conceived embodiment, a fixed prism spectacle would be created in such a manner that the prism is capable of being rotated to the patient's preference, therefore accommodating adjustable ophthalmic prism base direction. In addition, a means to periodically adjust the prism orientation and prism diopter strength with a physician's prescription is envisioned.

As previously discussed when regarding the quality of medical publications, it has been determined that the creation of a set of eye glasses with a fixed, or adjustable prism, would not be worth the development time due to research already invested in this area. As such, this method of image relocation was ruled out as a possible device to rehabilitate AMD patients.

3.2.2 Fluid Filled Lens

The second envisioned design encompasses a fluid filled lens, consisting of a distensible bladder, which is capable of changing dioptric power of the prism by varying the amount of fluid inside the bladder.

This method is an extension of the SuperFocus lens available at superfocus.com [86], and is shown in Figure 3.1. The lens works as a dual lens pair, one flexible lens in the rear, and a rigid prescription lens in the front. The flexible lens has a transparent distensible membrane attached to a clear rigid surface. The pocket between them holds a small quantity of clear fluid; as the slider on the bridge is moved, it forces fluid into the lens and alters its shape. Changing the shape in turn changes the correction; this approximates the reshaping of the lens in the primate eye to provide distance correction.

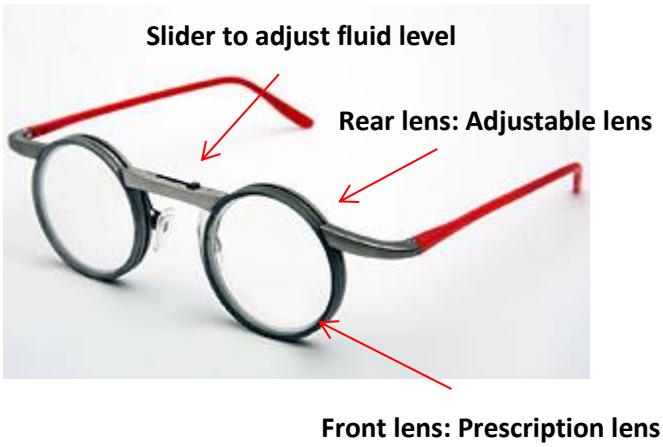

Figure 3.1: SuperFocus Eye Glasses

The proposed device would consist of a distensible prism, which when filled with fluid, would increase the dioptric prism power by increasing the length of the prism base. Ultimately, this approach was deemed less flexible than other options and was not investigated further.

3.2.3 Electro-optic Kerr or Pockels Lens

A design utilizing an electro-optic lens operating using the Kerr or Pockels effect, wherein the birefringence of the lens material is changed with the application of an electric field was conceived. As a pre-requisite to utilizing these electro optic effects, incident light must first be polarized, therefore exacerbating the issue of achieving sufficient lighting for AMD patients. [8]

This method relies on either the linear or quadratic electro-optic effect, where an applied electric field changes the birefringence of the optical material, effectively changing the index of refraction. A material is said to be birefringent if it displays two unique indices of refraction, dictated by polarization of incident light. With a birefringent material, the index of refraction can be selected by an appropriate selection of incident light polarization, and if that material exhibits properties similar to a Kerr or Pockels cell, this birefringence is a function of an applied electric field. These polarization planes correspond to being parallel or perpendicular to the applied electric field. Birefringence is schematically represented in Figure 3.2, where the o-ray is the ordinary, expected path for a ray to take, and the e-ray is the extraordinary, differing path for the ray to take.

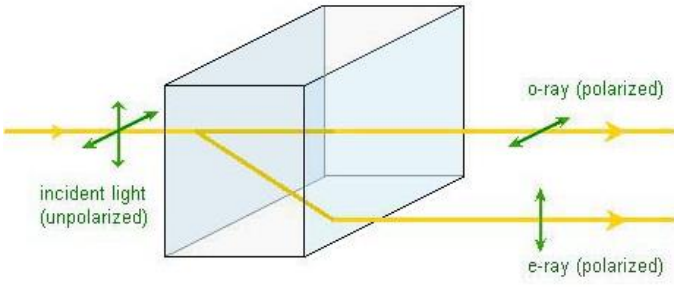

Figure 3.2: Birefringence [87]

The difference in the index of refraction for parallel and perpendicular directions, Δn, is the birefringence, and in the case of the Kerr effect, the quadratic electro-optic effect is known to be:

$$\Delta n = \lambda_0 K E^2 \tag{3.1}$$

In equation 3.1 λ_0 is the wavelength of incident light, K is the Kerr constant, and E is the magnitude of the electric field in statvolts per cm. Most materials (liquids) that exhibit the Kerr effect are known to be poisonous to humans.

The Pockels effect (proportional electro-optic effect) is known to be:

$$\Delta n = \lambda_0 r E \tag{3.2}$$

Where again, in equation 3.2, Δn is the birefringence, λ_0 is the wavelength of incident light, r is the Pockels coefficient and E is the magnitude of the electric field in statvolts per cm. Of the 32 crystal symmetry classes, 20 of them exhibit the Pockels Effect, which also correspond to the same 20 classes that exhibit the piezoelectric effect. [88]

One further complication to this method, other than the inherent toxicity concerns, is that the number of prism diopters achievable are quite few, resulting in a device that does not relocate the image to a significant degree, and one that is not very adjustable. Furthermore, the power supply required to quickly relocate images could become quite large. Due to these concerns, this design idea was not further pursued.

3.2.4 Electro-optic Liquid Crystal Lens

Similar to the aforementioned electro-optic lens, this lens would differentiate itself by utilizing colloidal liquid crystals whose crystal structure changes with the application of an electric field,

thereby changing the refractive index of the lens material. Similar to the other conceived electro-optic lens, this method would require the polarization of incident light.

This method of image relocation is similar to the approach taken by LifeActivated who make the EmPower glasses, formerly available from lifeactivated.com, which are currently produced for presbyopia. These glasses consist of a thin layer of nematic liquid crystals that change orientation when an electric field is applied, therefore changing the birefringence of the material and changing the dioptric power of the lens. These glasses have received generally poor reviews and have been considered to be unreliable, easily broken, and expensive, costing around $1200.00 [89]; however, they are included in Figure 3.3.

Figure 3.3: EmPower glasses [90]

3.2.5 Wearable Digital Light Processing Device

This method entails the hypothetical creation of a custom digital micromirror device (DMD), utilizing digital light processing technology (DLP) to reproduce or redistribute light that would normally be incident upon the fovea to other portions of the eye.

The notion of using DLP technology to manipulate how an image would be formed on the retina, after some investigation, appears incapable of the proposed usage. The only use for such technology would be in the formation of an already captured image, as an alternative to a liquid crystal or similar display. DLP's operate in a television or projector using a myriad of 16 μm square mirrors in an array such that each mirror corresponds to a single pixel to be created. The micromirrors rapidly pivot between ±10 degrees, the more time a mirror is toggled in the "on" position, the lighter the corresponding pixel appears. Therefore, DLP's may not be used to transform an image given the micromirror's limited range of motion, they are only used to recreate an image with desired gray scale values, and is not a feasible solution at the current time.

3.2.6 **Diffraction Grating Spectacles**

This method entails the creation of a set of diffractive optic lenses used to achieve an optical coordinate transformation. Such a set of gratings would first manipulate the incident light, e.g. its phase, and the second would collect and focus the light to be imaged on healthy portions of the retina.

This above method of achieving an optical coordinate transformation via diffractive optical elements would be a compromise between diffractive limits on the small end, and optical aberrations on the large end. Additionally, the initial tooling would consist of ion mills, or machinery equivalent, and would have a cost on the order of hundreds of thousands of dollars, but thereafter would be relatively cheap to manufacture. These elements would not be capable of being adjusted. This methodology currently appears outside the scope and timeline of the proposed project, and will not be investigated further as part of this project.

3.2.7 Head Mounted Digital Image Warping Prosthesis

The seventh conceived method entails the usage of a head mounted display (HMD), wherein a camera, or two, captures images in the forward facing direction, a computer processes the captured frames from the camera, remaps the images according to a function designed to accommodate for the user's scotoma. The post-remapping image would then be sent to displays within the HMD to be viewed by the user. This device has the potential to track eye movements, thereby increasing the percentage of time that light is focused on the patient's PRL. This method also has the marked advantage of being able to manipulate the image being formed in more extreme fashions than conventional optical physics will allow. Additionally, digital image processing techniques can be applied to enhance the image, such as contrast inversion to assist with cloudy ocular media, for easier viewing by the wearer.

This method would be the easiest to implement, as all optical manipulations would be done in the digital domain, and simply displayed to the wearer via a display screen internal to the HMD. Due to this fact, any type of image manipulation is achievable, whereas the other approaches are extremely limited by physical phenomena. This method also has the capability of tracking the wearer's eye saccades and adjusts the output image correspondingly. Given current technological limitations, this approach would physically be on the large end, but would easily be the most adjustable. In addition to these benefits, the aforementioned device would easily be capable of enhancing contrast while reading low contrast publications such as newspapers via optical thresholding, or display a negative gray scale image to further increase ease of reading in the case of cloudy ocular media.

3.2.8 Retinal Image Relocating Contact Lens

This method would be similar to 3.2.1 with the exception that the refractive media would rotate with the eye, thereby ensuring the image is relocated to the PRL at all times. After further investigation this method is likely to be far too bulky to be comfortably worn in contact with the wearer's cornea. Due to this predicted bulk, this method was not pursued further.

3.2.9 Phakic Intraocular Lens for Retinal Image Relocation

Phakic intraocular lenses (PIOLs) are a kind of intraocular lens that is surgically implanted into the eye, historically used to correct myopia. In contrast to traditional IOLs that are implanted during cataract surgery, phakic lenses allow for the eye's natural lens to be left untouched. The conceived method would allow for the creation of a PIOL used to achieve retinal image relocation. This could be achieved using either a diffractive grating, or small prisms such as Fresnel prisms. As mentioned previously, a device that moves with the eye, or tracks the eye's movement, would not be severely impacted by the orientation of the wearer's eye.

This approach would be somewhat similar to the two previously mentioned implantable telescopes, with the exception that it would focus on retinal image relocation, not just image magnification, and would not require the removal of the patient's natural lens. This method, however, would require a large amount of scrutiny as it is an implantable device, which makes it a less favorable option.

3.3 Head Mounted Display Prosthesis and Hardware

After appropriate exclusions, the determination that the method consisting of the head mounted display and corresponding digital image warping, would be the best approach with which to construct a prototype. The marked advantages of the device being completely adaptable, following the human eye and adjusting accordingly, and image relocation not being limited by the laws of physics, make it a much more attractive option than the others.

The decided upon path of constructing a head mounted display that operates using appropriate image warping algorithms was determined to consist of the following major parts:

1) Computer on which developed software performs the image warping
2) Designed software to perform the image warping
3) The head mounted display
4) A camera to capture forward facing images
5) A designed mount for the aforementioned camera
6) An eye tracking system

The final parts list deemed necessary for the project, with the exception of mount materials and cost of manufacturing are included in Table 3.1.

Table 3.1: HMD Low Vision Prosthesis Parts List

Item	Qty.	Part	Price per unit
1	1	Arrington Research Monocular Eye Tracker (MAU-Zsight)	14,088.00
2	1	Sensics Zsight HMD	12,545.00
3	1	Asus G750JW Laptop	1,399.00
4	2	3 meter USB 3.0 cable	35.00
5	2	IDS USB 3.0 "CP" series camera tripod adapter	35.00
6	2	IDS USB 3.0 camera (IDS-UI-3240CP-C-HQ)	767.00
7	2	6mm KOWA machine vision lens	123.00
		5% educational discount from 1st vision	-96.00
Total			**29,856.00**

3.3.1 Sensics zSight HMD

The Sensics zSight HMD was decided upon because it was the best combination of achievable field of view (larger than 60 degrees, diagonal), price and screen resolution. Further influences were University of Minnesota Psychology professor Dr. Steven Engel's previous experience and satisfaction with the Sensics brand. Additionally, Arrington Research makes a model of their eye tracker to be installed directly into this model without additional custom work; it was therefore deemed the best use of time and money to buy the items that were designed for each other. Furthermore, when investigating eye trackers, the application programming interface (API) accompanying the Arrington Research brand appeared to be the easiest to use and fit the application the best.

The Sensics zSight head mounted display is a professional quality HMD with two full color, SXGA (1280 x 1024) OLED micro displays, refreshing at 60 Hz. More specifically, the OLED displays within the zSight have a contrast ratio of 10,000:1, a luminance of 150 fL, and a 24 bit color depth. The zSight creates a 60^{o} diagonal field of view (46.9^{o} horizontal, 37.5^{o} vertical) with 100% binocular overlap. The normal human visual system accommodates up to approximately a

180^o (lateral) field of view with 100^o of binocular overlap (50^o to each side of the nose). The visual binocular overlap is the region in which parallax is achievable to create the sensation of depth perception. Additionally, at 400 grams the zSight is lightweight compared to many HMDs. It is capable of accepting single or dual HDMI inputs and has an eye tracking option specifically designed for it. [91]

The zSight supports 2D and 3D viewing modes, 2D with one input of either SXGA (1280x1024) or 720p (1280x720) resolution, or 3D with two of these inputs (one for each eye). The above resolution results in a very good 20 pixels / degree view. 3D viewing may be achieved using two HDMI inputs by sending two 1280x1024 images to the HMD in what is known as "horizontal span mode", or with one input by sending two side by side images of 640x1024 resolution. When two 640x1024 images are sent, using what is known as a "side-by-side" 3D signal, the zSight reconstructs the full 1280x1024 resolution, thereby resulting in a less than optimal resolution. In order to change these modes the zSight Control program must be launched, "displays" window selected, and "Side by Side 3D" toggled.

The adjustability of the zSight set it apart from many, less expensive, HMDs. The zsight offers an interpupillary distance (IPD) adjustment mechanism, which is capable of ranging the IPD from 52mm to 72mm. Additionally, each eye tube rotates in order to change the focus for each eye; the range of focus adjustment is ± 4 diopters. The variable dioptric power of the eye tubes is important as most individuals with AMD additionally suffer from presbyopia, a result of aging in which the eye exhibits a diminished ability to focus on near objects, and will need additional dioptric power to focus on objects near the eye. As discussed in the section regarding other eye conditions, these adjustable eye tubes would allow many individuals with hyperopia, myopia, and presbyopia wear the HMD without the use of their prescription corrective lenses. If other eye

disorders are present, such as astigmatism, however, their prescription lenses would be required to be worn underneath the HMD.

Additionally, as opposed to many HMDs with only a head strap tensioner, the zSight offers a head strap height adjustment to more securely attach the HMD to the wearer's head. Figures 3.4 and 3.5 illustrate the adjustable elements of the HMD.

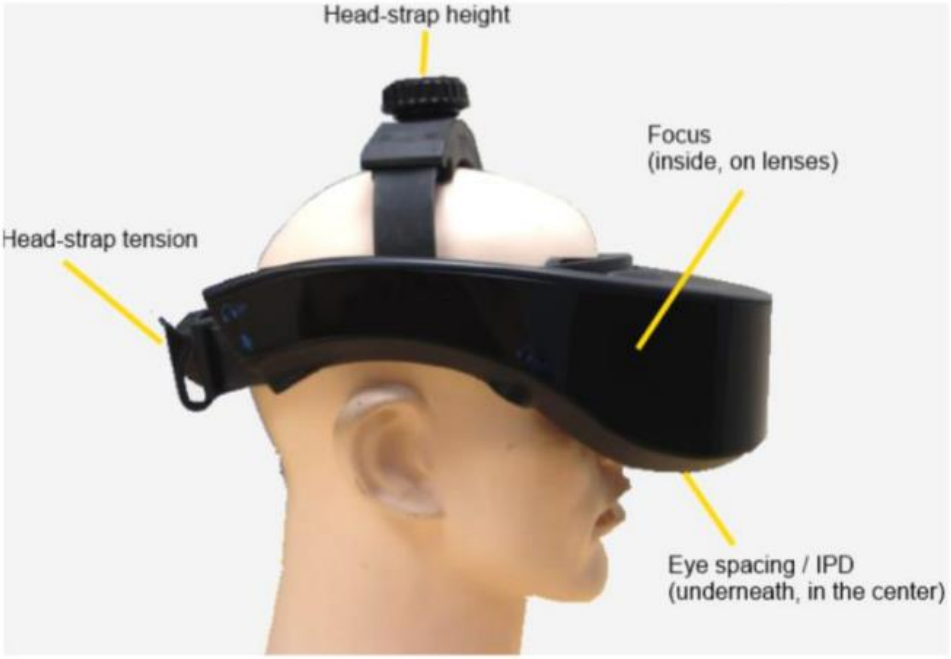

Figure 3.4: zSight HMD Adjustments

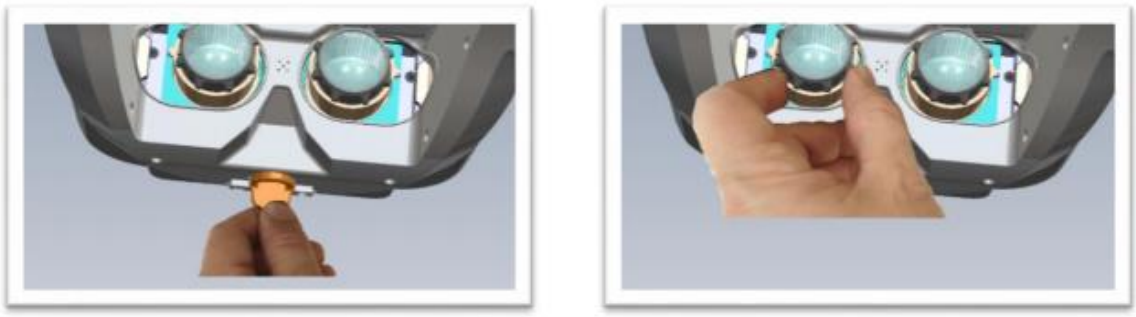

Figure 3.5: zSight IPD and Correction adjustment

3.3.2 **Eye Tracking**

Historically, eye tracking has been approached using many differing methodologies which may be partitioned into electrical methods and optical methods. Electrical methods include electro-oculography (EOG), a process where the electrical potential between the front and back of the eye is recorded. This approach has been proven to be imprecise and is time invariant as the amount of potential has been recorded to be a function of time during the day. [92] Additional electrical methods take advantage of electrical induction. One of the most precise ways of measuring eye position employs implanted coils within the sclera of the eye, termed scleral search coils, in conjunction with a magnetic field. When the eye is moved electrical currents are induced and easily measured.

Optical methods include reflection tracking, dark pupil tracking, limbus tracking, bright pupil tracking, corneal bulge tracking and vector differences. A ubiquitous and very sensitive way of

determining gaze direction employs tracking of Purkinje images. Purkinje images are reflections off of different refractive elements of the eye: first occurring at the interface between air and cornea, second at the interface between cornea and aqueous humor, third at the interface between aqueous humor and crystalline lens, and fourth at the interface of the crystalline lens with the vitreous humor. These are commonly referred to as the first through fourth Purkinje images, and are illustrated in Figure 3.6.

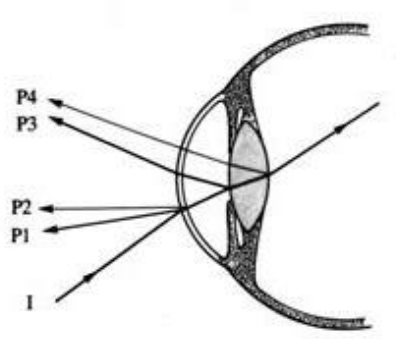

Figure 3.6: Purkinje Images: [93]

Commonly, the first Purkinje image is used to track eye location, as it is the most easily detected. Some eye tracking algorithms track the location of the 1st and 4th Purkinje images as a means to accurately determine gaze direction, which is known as a vector difference method.

Dark pupil tracking utilizes an uncollimated infrared light source to illuminate the eye. This attempts to brightly illuminate the iris, but leaves the pupil dark as the light is absorbed in the retina. Simple segmentation techniques, or a Hough transform, are then used to determine the pupil location. Limbus tracking, as the name implies, tracks the eye's limbus. This is performed using the differences in reflectivity of the smooth cornea and relatively rough sclera. The bright pupil method uses collimated infrared light that is reflected off the retina, which is then detected

and used to locate the pupil's location. In the corneal bulge method, an array of detectors is used to capture variations in total infrared light reflection in all directions. Using this information, the corneal bulge, and therefore the pupil, can be located. Another vector based approach is one which may be used by the ViewPoint eye tracker if selected: the pupil-corneal complex method. In this method the dark pupil is located using the dark pupil method described previously, and the 1st Purkinje image is located, thereby creating two reference points to attempt to make a refined pupil location estimate. The ViewPoint eye tracker by default uses the dark pupil method described previously.

In the ViewPoint eye tracking system the eye is imaged using a series of mirrors attached to a two bar linkage anchored to the HMD, as shown in Figure 3.7, which directs the image to a miniature camera within the mount. The mounts for the mirror also contain two small uncollimated infrared light sources that illuminate the eye. With the eye imaged, the program performs pupil location, and then maps the rotation of the eyeball to the coordinate system of the internal displays of the HMD.

Figure 3.7: ViewPoint EyeTracker internal mirror and IR light sources (white squares)

Video feed from the miniature camera is sent to the PC using a BNC connector in conjunction with a Sensoray s2255 framegrabber, which allows for transmission to the PC using a USB 2.0 connector. The sensoray s2255 is capable of capturing uncompressed frames from up to four NTSC or PAL video sources, performs digital signal processing, and then sends them to an output source over USB 2.0. Frames are capable of being capture from all four channels simultaneously with a maximum aggregate frame rate of 60 fps (NTSC), or 50 fps (PAL). [94] Furthermore, the s2255 offers deinterlacing to eliminate motion artifacts and its own API for developers to manipulate. The s2255 is shown in Figure 3.8.

Figure 3.8: Sensoray s2255 Frame Grabber [95]

3.3.3 Other Selected Components

The IDS u-eye camera was specified to match the resolution of the screens inside the HMD, as well as provide for a relatively small form factor that was capable of high data transmission rates and power through one USB 3.0 connection. The 6mm Kowa machine vision lens was specified to capture the same field of view that would be seen from within the HMD by the wearer.

With parts purchased, the large design thrust would be to create the image remapping software. OpenCV 2.4.6 (open source computer vision library) was decided upon to be used in conjunction with the C++ programming language in order to create the simplest, yet fastest, program possible. OpenCV is largely regarded as the main library to use when performing image processing and computer vision tasks within the C++ environment.

3.3.4 Camera Mounting System

Last items include the design and fabrication for a camera mount with which to attach the purchased machine vision cameras to the head mounted display. SolidWorks CAD models were obtained from Sensics that were used to perform top-down design of the mounts, a process where the features in the existing models are used to design new parts. With these files, two different mounts were designed, one for attaching a single camera, and one for attaching two cameras, where the mounts attached to the HMD by utilizing existing screw patterns used to secure the HMD's external housing. Furthermore, CAD models were obtained from IDS of the uEye 3240CP machine vision camera so that the mounting screw pattern at the underside of the cameras could be matched to the mounting platform of the camera mount.

Mechanical design of the mount did not include any exhaustive structural analysis due to the fact that the weight of the camera being attached was only 0.091 lbs. Although structural analysis was not performed, good engineering design principles were observed, as can be seen by thickening the periphery of the mounting surface to effectively increase the area moment of inertia of the cantilevered mounting platform, as well as the rib underneath to further inhibit strain from induced bending stresses.

The camera mount was designed using transition fit tolerances (+0.05”) over the nominal values specified within the SolidWorks assembly. The transition fit specification results in a close mate between the HMD housing and the mount, without causing unnecessary bending of the mount to fit over portions of the HMD that may be larger than the nominal value. The mounting platform elevation was designed such that the height of the visual axes of the cameras matches exactly that of the eye tubes within the HMD.

For initial testing, only the single camera mount will need to be created as all initial testing will be performed monocularly. With this in mind, only the single camera mount was created using VeroWhite Polyjet Resin in the University of Minnesota Medical Devices Center’s Objet260 multi-material 3D printer. The elapsed time for creation of the rapid prototype was approximately 4 hours, with a total price of labor and materials being nearly $130.00. The mount may be seen in Figures 3.9 and 3.10.

Figure 3.9: Single Camera Mount

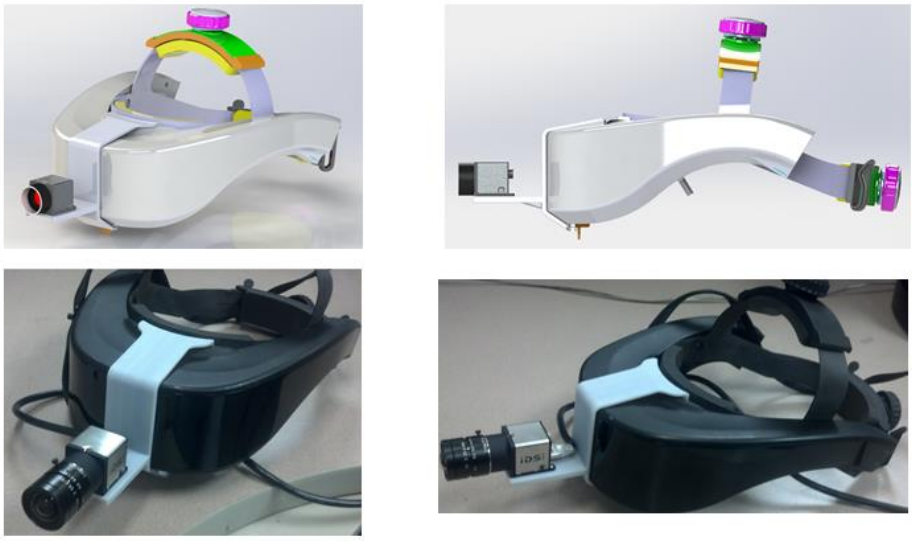

Figure 3.10: Single Camera Mount Assembly

The camera mount designed for two cameras, although not manufactured, attaches to the HMD in the same way that the single camera mount does, but differs in the fact that there are two forward facing cameras with an adjustable interpupillary distance to replicate the IPD set by the user inside the HMD. The interpupillary distance is adjusted by an opposing threaded lead screw, which when turned changes the distance between the two cameras. The platforms on which to mount the cameras are attached to two square nuts which ride on the lead screw. The last piece is a stabilizing bar to ensure that the cameras remain facing forward, without tilting, when the lead screw is turned. The double camera mount is shown in Figure 3.11.

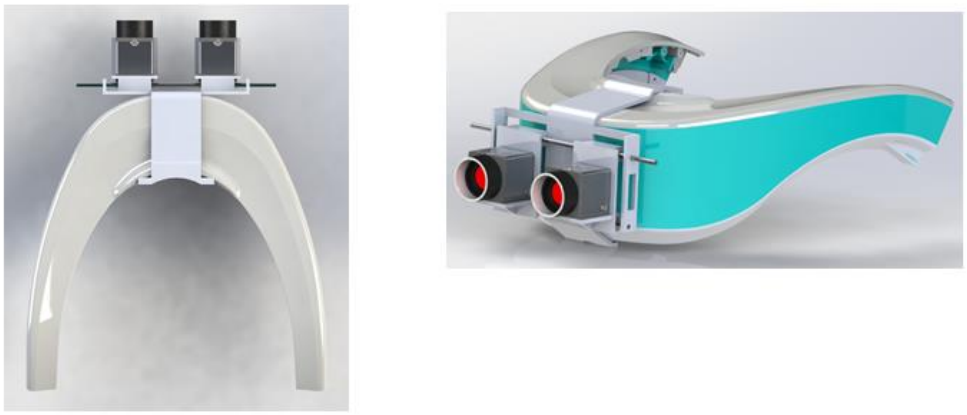

Figure 3.11: Double Camera Mount

3.4 **Image Warping (Spatial Transformations)**

A spatial transformation, alternatively called a geometric transformation, defines a mapping between the point (u,v) of some input image matrix and point (x,y) in some output image matrix. Spatial transformations were originally developed as a means to compensate for optical aberrations, such as barrel distortion accompanying a wide angle lens, by inverting the equations used to model the phenomena. Generally, the mapping functions are given in one of two forms: either relating the output coordinate system to that of the input, known as an inverse or reverse mapping, or relating the input pixel coordinate system to that of the output, known as forward mapping. The respective models for such mappings can be expressed as either

$$[x, y] = [X(u, v), Y(u, v)] \tag{3.3}$$

Or

$$[u, v] = [U(x, y), V(x, y)] \tag{3.4}$$

Where [u,v] refers to the input matrix coordinates, [x,y] refers to the output pixel coordinates, X,Y are the forward mapping functions used to uniquely identify the output pixel location, and U,V are reverse mapping functions that are used to uniquely specify the corresponding spatial transformation. In the case of forward mappings, discrete input pixels are mapped to output positions, and when performed as a point-to-point operation, can result in holes and overlaps in the output image. Methods such as the four-corner mapping paradigm exist to circumvent these artifacts by employing accumulator arrays which are capable of transforming pixels represented as square patches to arbitrary quadrilateral shapes. [96] Alternatively, super sampling the input image can remedy the aforementioned artifacts, but both methods are unnecessarily computationally expensive. The forward mapping procedure is schematically represented in Figure 3.12, below.

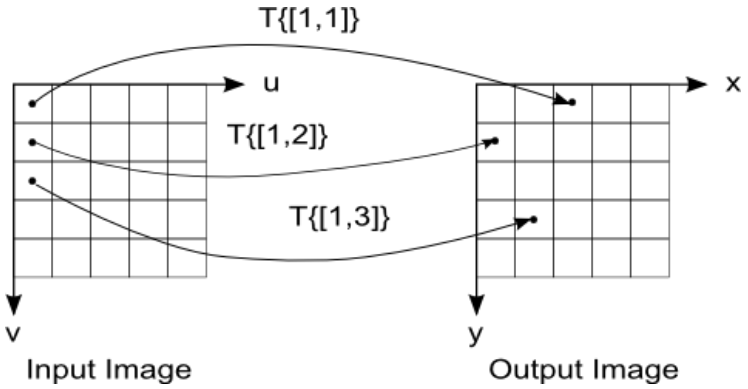

Figure 3.12: Forward Mapping Procedure

In the case of inverse mappings, discrete output pixels are mapped to input positions, which may result in the problem of undefined input positions. To remedy this, an interpolation strategy is required to retrieve input values at positions that are undefined. Contrary to the point-to-point forward mapping scenario described above, the inverse mapping procedure guarantees that every

pixel in the output image is computed. The notion of holes and overlaps for forward mappings can still be applied to inverse mappings, but these holes now are associated with the input image, allowing for certain data from the input image to not be sampled and presented in the output image.

An inverse mapping has been employed throughout the course of this project to ensure that all points are correctly mapped and that no output holes or overlaps exist. Accordingly, a horizontal mapping matrix, U, and a vertical mapping matrix V are employed to dictate, on a pixel by pixel basis, for every output image pixel [x,y], which input image pixel, [u,v] is to be sampled. A schematic of the operation described is included in Figure 3.13.

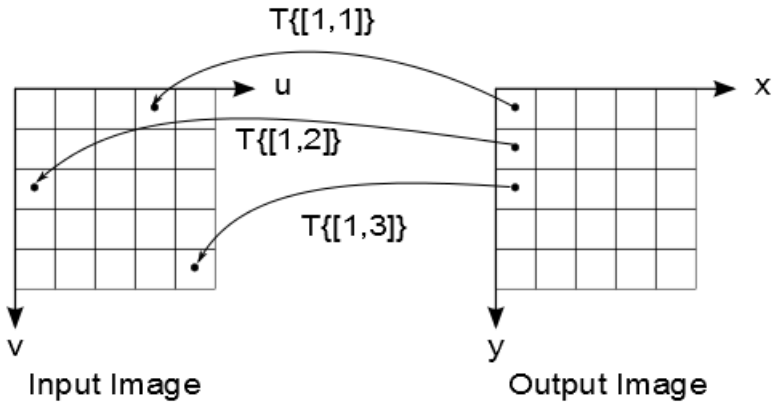

Figure 3.13: Inverse Mapping Procedure

The inverse mapping procedure can be represented in equation form as:

$$dst(x,y) = src\left(f_x(u,v), f_y(u,v)\right) \tag{3.5}$$

Image warping algorithms that were first considered were those proposed by computer scientists for use in what is known "Focus + Context" applications. These types of problems consist of obtaining some fine detail within an environment, all the while retaining where this fine detail is

situated within a large set of data. A subset of solutions to these problems is known as fisheye-view warping. [97] [98] [99] This fisheye view warp is so called because it is based on how a fish would see an ultra-wide hemispherical view from beneath the water. This results in items near the center of the screen appearing large, with items nearing the periphery of the screen becoming smaller in a nonlinear fashion.

A similar approach to a fisheye warping is a barrel distortion warping. First attempts at creating an inverse mapping algorithm included the application of Brown's distortion model to approximate barrel distortion created by wide angle optical lenses. To perform this mapping procedure, normalization is first performed to relocate the origin of the image matrix to the center of the image, as indicated in equations 3.6 and 3.7 for the horizontal and vertical coordinates.

$$t_x = scale_x * (x - \left[\frac{width}{2}\right]) \tag{3.6}$$

$$t_y = scale_y * (y - \left[\frac{height}{2}\right]) \tag{3.7}$$

Second, the algorithm obtains the transformed radius via a Euclidian norm:

$$r_t = \sqrt{{t_x}^2 + {t_y}^2} \tag{3.8}$$

Population of the mapping matrix via u, the horizontal mapping components, and v, the vertical mapping components is then performed. This mapping matrix instructs the output matrix which locations in the input matrix to map to according to equations 3.9 and 3.10.

$$u = t_x(1 + K_1{r_t}^2) + [width/2] \tag{3.9}$$

$$v = t_y(1 + K_1{r_t}^2) + [height/2] \tag{3.10}$$

The above is a first order, symmetric (e.g. neglects tangential components), approximation to Brown's distortion model [100] indicated in the equations below:

$$u = (x_d - x_c)(1 + K_1 r^2 + K_2 r^4 + \cdots) + (P_1(r^2 + 2(x_d - x_c)^2) + 2P_2(x_d - x_c)(y_d - y_c))(1 + P_3 r^2 + \cdots) \quad (3.11)$$

$$v = (y_d - y_c)(1 + K_1 r^2 + K_2 r^4 + \cdots) + (P_1(r^2 + 2(y_d - y_c)^2) + 2P_2(x_d - x_c)(y_d - y_c))(1 + P_3 r^2 + \cdots) \quad (3.12)$$

Where, (x_d,y_d) are the distorted image points as projected on an image plane using the distortion applying lens, (x_u,y_u) are the undistorted image point as projected by an ideal pin-hole camera, (x_c,y_c) are the coordinates for the distortion center, K_n is the n^{th} radial distortion coefficient (which is truncated beyond the squared radius term in the algorithm), P_n is the n^{th} tangential distortion coefficient (absent from the symmetric approximation), and r is the Euclidian norm (distance from the center of distortion). The mappings above create images such as the ones in Figure 3.14, dependent upon the magnitude of the radial distortion coefficient:

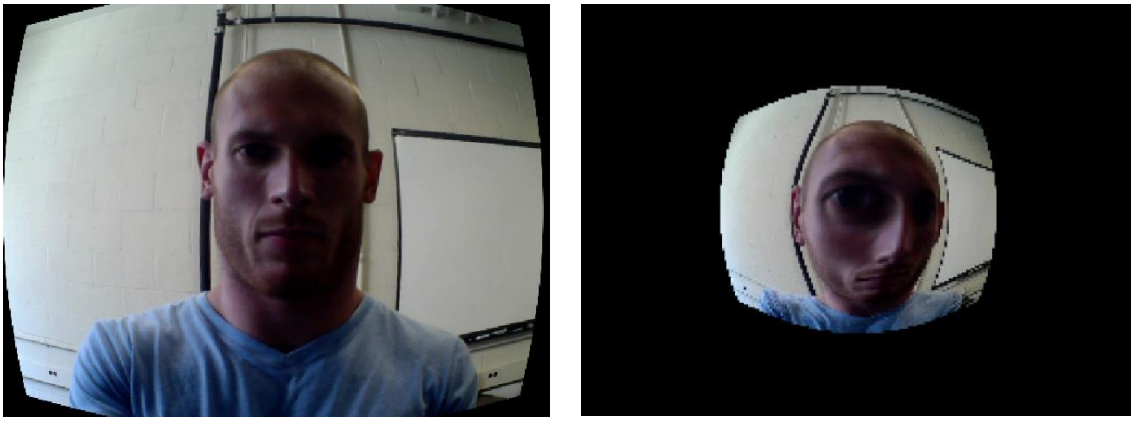

Figure 3.14: Warping with Brown's Distortion Model

These mapping algorithms marked the first successful remapping programs created for this project, albeit very slow, achieving frame rates only on the order of 1-2 frames per second. Although the remapping algorithms described above were successfully created, their use for rehabilitation of AMD is inappropriate due to the severe distortions created; reading text

remapped according to the above equations was nearly an impossible task. The degree of distortion and magnification caused by remappings can be quantitatively described by performing eigenvalue decomposition on the matricial relationship between input and output pixels, as described in section 3.5, and will be an important tool in developing and analyzing remappings for use in visual field defects.

More appropriate remapping algorithms for the compensation of visual field defects in AMD patients were deemed to be of a Column Gaussian Bump and Column Gaussian Squeeze variety. [75] In these algorithms, an inverse remapping is carried out such that pixels in the output image are spatially re-distributed according to a Gaussian, about some mean pixel value corresponding to the normalized center of the image. The Column Gaussian Bump algorithm results in a "bump" corresponding to the height and standard deviation of the Gaussian, causing some information from the input image to not be sampled and mapped into the output image. Alternatively, the Column Gaussian Squeeze algorithm "squeezes" the column above and below the normalized image center proportional to the pixel distance from the image edge. This algorithm therefore results in a sampling of all input data, but creates for additional distortions in the output image. The mapping functions for the Column Gaussian Bump are indicated in equations 3.13 and 3.14, while those for the Column Gaussian Squeeze are shown in equations 3.15 and 3.16.

$$u = x \tag{3.13}$$

$$v = t_y - \left\{ b * exp\left(\frac{-{t_y}^2}{a^2}\right) * sgn(t_y) \right\} + \frac{height}{2} \tag{3.14}$$

$$u = x \tag{3.15}$$

$$v = t_y - \left\{ b * exp\left(\frac{-{t_y}^2}{a^2}\right) * sgn(t_y) * \left[1 - \frac{2|t_y|}{height}\right]\right\} + \frac{height}{2} \quad (3.16)$$

In the above equations the parameters a and b correspond to the semi-major and semi-minor elliptical axes, respectively, which are fit to a simulated scotoma used to replicate the patient's actual scotoma. Note that in equation 11 the mapping is squeezed according to the difference between the integer 1 and twice the ratio of the transformed height and absolute height of the image. These mappings are illustrated in Figure 3.15.

Additional mapping algorithms investigated were column elliptical bump and column cosine bump, of which these mapping types proved to be very difficult to read with due to the fact that they created a discontinuity at the edges of the column in which the text is "bumped" vertically to avoid the wearer's scotoma.

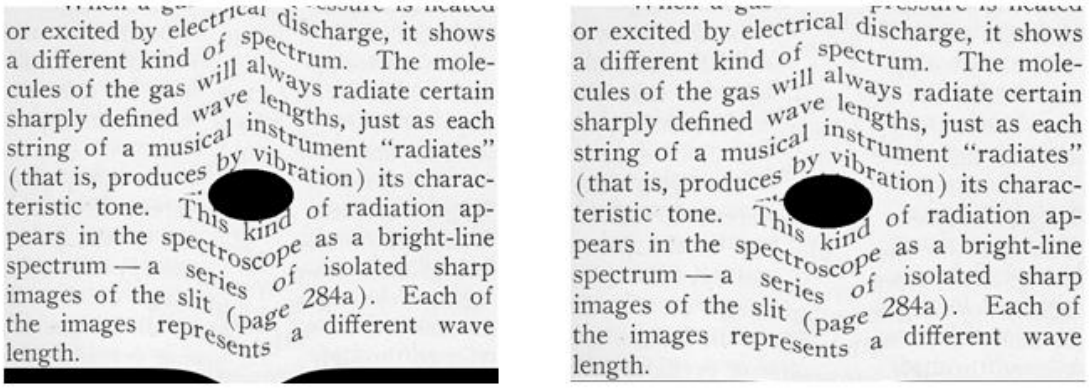

Figure 3.15: Column Gaussian Bump (left), Column Gaussian Squeeze (right)

The artifacts at the center of the images above correspond to an ellipse fit to the wearer's anatomical scotoma. Ellipses are chosen due to the fact that they have one more degree of freedom than a circle and are negligibly more computationally expensive to create. The notion is that the ellipse adheres to the wearer's scotoma, and translates with the wearer's visual gaze point

by use of the installed eye trackers. The parameters of this ellipse additionally dictate the height and variance of the Gaussian distribution. The remapping then provides a way to redistribute information that would normally be incident upon the user's fovea, to the parafoveal region corresponding to their PRL.

The remapping itself is carried out with the creation of OpenCV 2.x Mat type containers created to contain pixel information for the input image frame, output image frame, and remapping data in the horizontal and vertical directions. Every pixel in the horizontal and vertical remapping matrices are iterated through, and the remapping functions described in equations 8 and 9 are evaluated, thereby creating a map from output pixels to input pixels. Since the remapping operation is a simple assignment operation, the remapping process itself is performed on the GPU, which is optimized for carrying out many small operations simultaneously. Correspondingly, these matrices are written to GPU memory, using the gpu::GpuMat container types. The OpenCV function gpu::remap then performs the matrix product operation to write pixel blue, green and red values in the input image to the output image. As mentioned previously, some kind of interpolation is required since non-integer pixel values may be mapped to. OpenCV's remap function is capable of doing this without any additional steps by setting the interpolation input flag to the appropriate value. Bilinear interpolation is used by default, which appears to have good performance, with other interpolation methods available being nearest-neighbor, pixel area relation, bicubic interpolation over a 4x4 pixel neighborhood, and a Lanczos interpolation over an 8x8 pixel neighborhood. These more computationally expensive interpolation methods appear to have no benefit over the more simple bilinear method. [101]

3.4.1 **Digital Image Processing Capabilities**

In addition to complex remapping algorithms, other capabilities have been added to the program including Gaussian pyramiding, color inversion, BGR to grayscale conversion, and image thresholding, as shown in Figures 3.16 a – d.

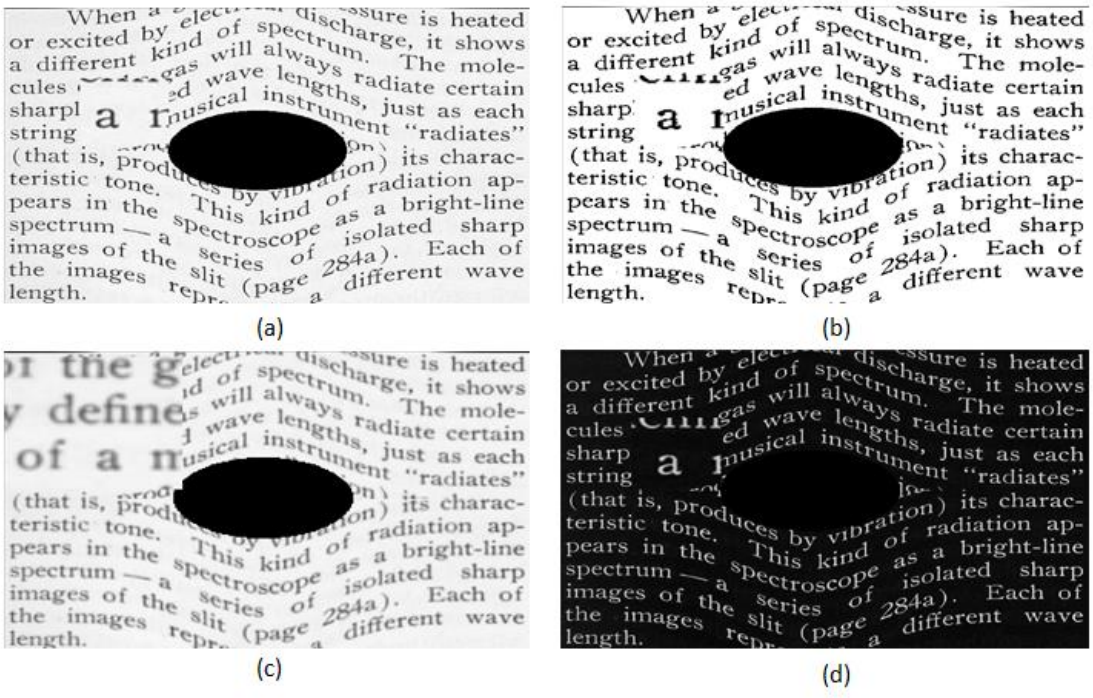

Figure 3.16: (a) Normal Gaussian Bump Remapping, (b) Intensity Thresholding, (c) Gaussian Down Pyramiding, (d) Color Inversion

When Gaussian pyramiding is implemented, as shown in Figure 3.17, the algorithm "moves up" or "moves down" one layer of the image pyramid, thereby down or up-sampling the image respectively. This is done by first convolving the source image with a Gaussian kernel, then selectively removing even or odd numbered columns and rows and resampling the image. This has the benefits of utilizing all elements of the camera sensor, leaving the field of view unchanged, while decreasing the number of pixels needed to be remapped. Pyramiding then has

the benefit of increasing achievable frame rate, with the corresponding downfall of decreasing image resolution, which will be of lesser concern for low vision patients than normally sited individuals.

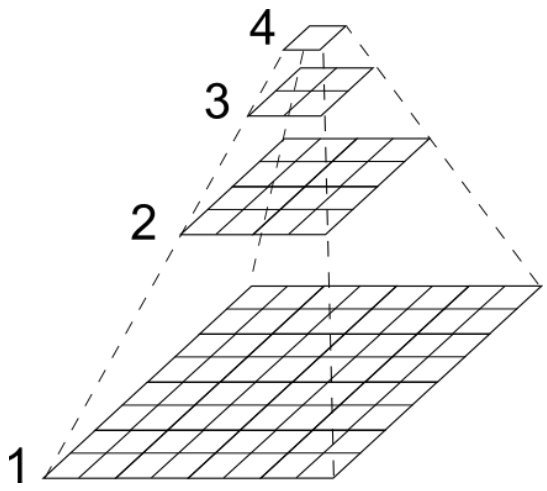

Figure 3.17: Four Layer Gaussian Pyramid

3.5 **Eigenvalue Decomposition of Image Warping Matrices**

A useful tool for studying the properties of created mapping matrices will be the use of eigenvalue decomposition of the Jacobian matrix resulting from the matricial relationship between (u,v) and (x,y), or alternatively analyzing maximum and minimum singular values obtained via singular value decomposition. Eigenvalue decomposition has been used in this case to study the distorting and magnifying properties of remapping algorithms. The local distortion is defined as unity subtracted from the absolute value of the ratio of the first and second eigenvalues, and provides a quantitative measure of how the output image is distorted, or more intuitively how stretched out it becomes. The local distortion is defined in equation 3.17, where

λ_1 and λ_2 represent the maximum and minimum eigenvalues respectively. Dependent upon an individual's field of study this may be more commonly referred to as unity subtracted from the condition number.

$$local\ distortion = \left|\frac{\lambda_1}{\lambda_2}\right| - 1 = condition\ number - 1 \tag{3.17}$$

The local distortion is zero for equal magnitude first and second eigenvalues, which is a global property of conformal mappings. Conformal mappings, also referred to as angle-preserving transformations or biholomorphic maps, are transformations that preserve local angles. By definition, an analytic function is conformal at any point that it has a nonzero derivative, or if it is a complex valued function, any function that has nonzero partial derivatives. [102] As conformality of mappings is lost, and as curvature of straight lines, unequal magnification, and spectral dispersion occurs, user adaptation has been shown to occur more slowly and to a lesser degree. [77]

It is presumed that local distortions nearer to zero are desirable, but not necessary, as the relationship between points in the image plane will remain nearly the same, i.e. the letters of text will not appear much differently to the wearer. If the local distortion is not equal to zero, a spatially invariant relationship would result in easier immediate reading without user adaptation.

Another quantitative metric to evaluate mapping matrices is the local magnification. The local magnification is defined as the absolute value of the product of the first and second eigenvalues. As the name suggests, the local magnification gives a quantitative measure of how enlarged the output image will become as a result of the remapping. The local magnification is defined in equation 3.18.

$$local\ magnification = |\lambda_1 \cdot \lambda_2| \tag{3.18}$$

If the Gaussian bump remapping described above was changed to be area preserving, the local distortion and magnification would be changed due to the fact that a fixed amount of information would be forced to be conveyed in a smaller image space. Therefore, for area preserving mappings, the local distortion and magnification will be dependent upon the size of the simulated scotoma.

For the case of the Gaussian bump remapping, if we were to describe the mapping in matricial form we would obtain the follow equation:

$$\begin{bmatrix} u \\ v \end{bmatrix} = \begin{bmatrix} 1 & 0 \\ 0 & \dfrac{(y - src\_height) - b * exp\left(-\dfrac{(x - src\_width)^2}{a^2}\right) * sgn(y - src\_height)}{y} \end{bmatrix} \begin{bmatrix} x \\ y \end{bmatrix} \tag{3.19}$$

And upon performing eigenvalue decomposition of the resulting Jacobian matrix, the eigenvalues and eigenvectors are shown to be:

$$\lambda_1 = 1, \qquad \lambda_2 = 1$$

$$V_1 = \begin{bmatrix} 0 \\ 1 \end{bmatrix}, \qquad V_2 = \begin{bmatrix} 1 \\ 0 \end{bmatrix}$$

From the above result we can easily see that scaling remains the same for the Gaussian bump remapping, the local distortion is 0, and that the output directions of significance are the x and y principal directions. For future use, if other remapping types are to be studied, the corresponding local distortion and local magnification, as a function of spatial location, should be used as parameters to characterize the remapping. As an illustration of this, it is easily shown that for the first order approximation to Brown's distortion model, as indicated in section 3.4, the eigenvalues are a function of spatial location, and the local magnification decreases as a function of radial

location.

3.6 **Magnified Region of Interest**

The use of a PRL by individuals affected by AMD is well documented, and it has been shown that decreased cone density results as a function of retinal eccentricity, therefore eccentric reading requires text magnified to a certain critical print size, but will always be of functional benefit. [103] Due to these observations a magnified region of interest that is tailored to the wearer's PRL has been envisioned, as shown in Figure 3.16.

The region of interest (ROI) can either be placed by experimentation with the user's preferences, or by recommendation from an ophthalmologist after performing scanning laser ophthalmoscope (SLO) macular function testing. It has been shown that the vast majority of unconsciously developed PRL's are located near the periphery of dense scotomas, as determined by SLO. [104] [105] There appears to be no tendency for PRL location, although PRLs above the scotoma are more common than below as reported at being 46% and 28% respectively, [106] so user's preference or SLO testing would be recommended as opposed to arbitrarily choosing a quadrant to represent the ROI in.

Scotomas are defined as areas of the retina that exhibit reduced light sensitivity in comparison to normally sighted subjects. Dense scotomas, sometimes referred to as absolute scotomas, are those that are insensitive to very bright objects, e.g. those that result in a large irradiance, while relative scotomas are less insensitive. [104] [107] [108] In order to delineate dense and relative scotomas, microperimetry may be performed using a scanning laser ophthalmoscope, in which

stimuli are projected into the center of the fovea with decreasing intensity. The first stimulus not recognized is then used as the threshold stimulus used to describe the affected area of the macula. Absolute scotoma size has a recorded mean of 1.299 mm^2, while relative scotoma size has recorded mean of 8.943 mm^2. [109] These results are somewhat arbitrary as scotomas may take any size, but these mean values will be used as testing parameters for the efficacy of the remapping application in later sections.

Due to perceptual completion, many scotomas are not detected; for scotomas of 6^o or less in diameter, as many as 77% may not be detected by Amsler grid testing. [110] Amsler grids are generally a very fast and easy way to evaluate metamorphopsia, warping of the visual field, in patients with visual field defects, generally within the central 10^o of view, as described previously.

Individuals with scotomas resulting from AMD typically report that reading is one of the life activities most impacted, and improved reading capability is often the primary rehabilitation goal. [111] Therefore, it is appropriate to test the impact any rehabilitation device may have on reading speed and comprehension. Difficulties often encountered when reading with AMD include very slow reading rates [49], inaccurate reading, often times missing portions of words or skipping lines of text [112], reduction in reading comprehension [113], fixation variability [114] [115] and typically exhibit a decreased endurance for reading when compared to normally sighted individuals [116]. Fixation variability has been reported to be on average 128 times (6.67 deg.) the BCEA (bivariate contour ellipse area) of normally sighted individuals. [115]

3.7 Software Concerns and Cyber Sickness

One of the major concerns associated with the remapping type, as well as remapping application frame rate, is cyber sickness. Cyber sickness, which shares a number of symptoms that are characteristic of motion sickness, has symptoms including: eye strain, headache, pallor, sweating, dryness of mouth, fullness of stomach, disorientation, vertigo, ataxia, nausea, and vomiting. Oftentimes motion sickness is the result of vestibular stimulation, sometimes acting concurrently with visual stimuli. Cyber sickness on the other hand is attributable solely to visual stimulation. In extreme cases, the symptoms of cyber sickness can linger for hours, and up to days. [117] These observations have resulted in regulations regarding virtual environment (VE) technologies, such as the mandatory grounding of pilots on air force bases for 12 to 24 hours after participating in VE training.

Of the numerous theories which exist that attempt to elucidate why motion sickness, and cyber sickness, occurs, the sensory conflict theory is the most widely accepted. The theory is based on the premise that discrepancies between vestibular sensory input and visual sensory input cause a perceptual conflict that the body does not know how to handle. In the case of motion sickness, this can be visualized with the scenario of an individual on a large ship at sea. When inside the ship, because the individual is moving with the local reference frame of the ship, one does not visually perceive the motion of the ship, but due to the vestibular system, the individual will still perceive the motion of the ship as it is moved by waves. Therefore, the individual's visual system informs them that they are not moving, but their vestibular system informs them that they are. Similarly, cyber sickness may result if the individual's visual sensory input informs them that they are moving, while their vestibular system does not. [118]

Factors that contribute to the onset of cyber sickness include position tracking error, where the information presented to the user does not accurately track their movements, lag, where there is a noticeable time delay between initiating an action and the presentation of that action to the user, and flicker, which is caused by slow display screen refresh rates and may cause eye fatigue. Relatedly, since rod photoreceptors are more sensitive to low intensity light, and therefore small changes in lighting intensity, the wider the field of view of the display is, the more likely it will be that flicker is perceived, and correspondingly, the more likely that cyber sickness may ensue. Furthermore, since woman have been recorded to have, on average, a wider field of view than men, they will be more likely to perceive flicker than men.

In addition to gender, another individual factor that affects the onset of cyber sickness is age. It has been reported that below age 2, individuals are generally immune to motion sickness and cyber sickness. Susceptibility peaks between the ages of 2 and 12, with a rapid decline between ages 12 and 21, which slowly continues through adulthood until approximately 50. After the age of 50 motion sickness and cyber sickness occurrences are both very rare. [118] These findings directly impact the scope of this work, as most individuals with AMD are typically 65 or older, and are therefore not very susceptible to cyber sickness. Nonetheless, best efforts should be made to reduce the likelihood that cyber sickness will be induced in any individual, regardless of age, gender, or any other attributing factors.

3.8 System Modulation Transfer Function

The optical transfer function, or modulation transfer function, is the transfer function of an optical system, which is used to describe the relationship between input to an optical system and the

resulting output that is imaged. Similar to Bode plots of transfer functions in classical control, the optical transfer function specifies the gain and phase vs. spatial frequency relationship of an optical system, as shown in Figure 3.18. In the case of an optical system, the use of the term "gain" is rather ambiguous, and instead the contrast, or sometimes the modulation, is used. Therefore, the spatial frequency response of the modulation transfer function dictates how well an optical system can resolve images as a function of spatial frequency. Modulation is defined as follows:

$$modulation \equiv \frac{I_{max} - I_{min}}{I_{max} + I_{min}} \tag{3.20}$$

In equation 3.20 I_{max} and I_{min} are the maximum and minimum irradiance either being fed into the system, or coming out of it. The optical transfer function (OTF) is therefore composed of the modulation transfer function (MTF) and phase transfer function (PTF), which dictate the gain and phase response of the system to frequency dependent inputs. [8] The OTF is then simply the MTF phase shifted by the PTF, as indicated below in equation 3.21.

$$OTF = MTF \cdot e^{i\varphi(\omega)} \tag{3.21}$$

The MTF has become a ubiquitous means of specifying the performance of optical systems, ranging from optical lenses, magnetic tape, telescopes, the Earth's atmosphere and the human eye. The modulation transfer function then must be taken into consideration when designing any optical system as it dictates the spatial cutoff frequency at which point the system can no longer resolve images successfully.

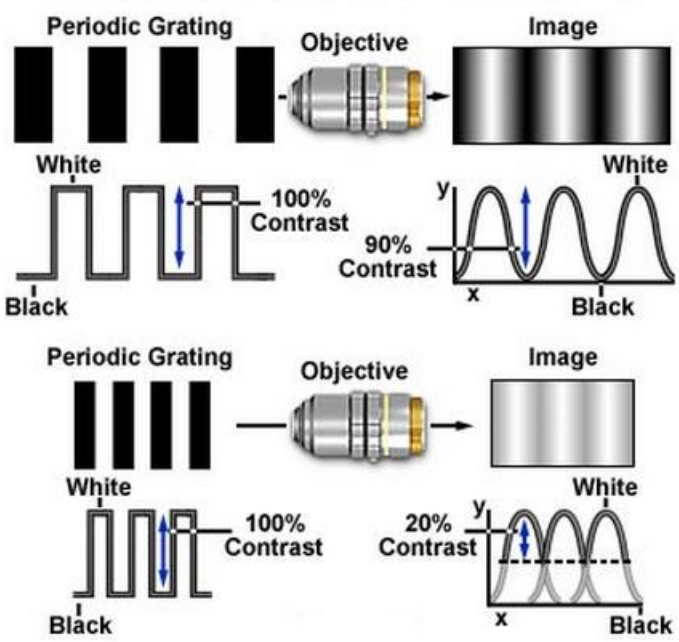

Figure 3.18: Modulation and Contrast Transfer Function [119]

Typically the spatial cutoff frequency is taken to the frequency at which the contrast goes to 0. The Kowa lens purchased has a spatial cutoff frequency greater than 60 line pairs per millimeter (lp/mm), while the display screens within the HMD are limited by half the number of pixels per millimeter, as two pixels are needed to image a line and the corresponding white space following it. [120] The cutoff frequency of the monitors can be assumed to be less than half that of the lens, which still largely exceeds that capable of being distinguished by low vision patients. The MTF for the human eye is show in Figure 3.19. [121]

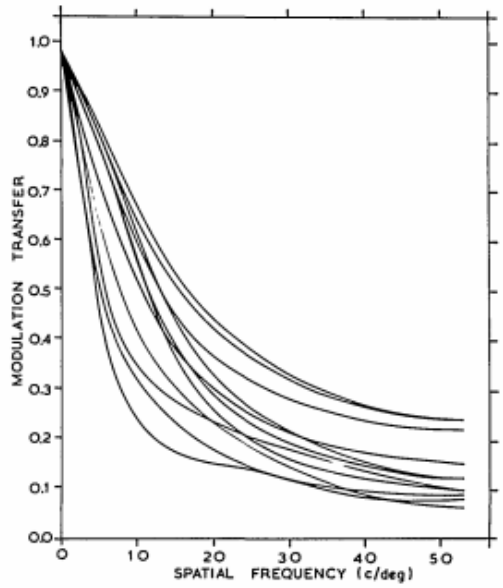

Figure 3.19: MTF of 10 human eyes

Spatial resolution for achromatic images forming on the fovea reach a limit of 60 cycles / deg of visual arc, which approximates the acuity limit theoretically imposed by the Nyquist sampling rate possible due to distributions within the cone mosaic. [122] At approximately 8 degrees of eccentricity spatial resolution limits decline to 10 cycles / deg. Comparing this to the limits set by the screens of the HMD, which are advertised as 20 pixels / deg, or 10 cycles (line pairs) / deg, we see that in the near periphery the spatial resolution of the retina equals that of the HMD. At the present time an MTF has not been calculated, as such calculations are lengthy, and high resolution is of no benefit to low vision patients. If at some point in the future contrast as a function of spatial frequency was a concern, an MTF should be calculated.

Chapter 4

Image Warping Performance

4.1 **Image Warping Optimization for Frame Rate**

A notable characteristic of the early version of programs developed was the very slow frame rates achievable, especially at full SXGA resolution, which averaged 0.4311 frames per second. Frame rate is determined using the OpenCV functions cv::getTickCount() and cv::getTickFrequency(), the former returning the number of system clock ticks since a certain epoch, typically computer start, and the latter returns the clock frequency (the number of clock ticks per second, in this case the clock frequency is 2338.250 KHz). With these functions it is easy to obtain the elapsed time, in seconds, for a portion of code by retrieving the tick count at the beginning of the code segment of interest, then again retrieving the system tick count at the end of the code segment of interest, taking the difference between these two values, then dividing by the system clock frequency, as noted in equation 4.1.

$$\Delta t = \frac{Clock\ Tick\ Count_2 - Clock\ Tick\ Count_1}{Clock\ Frequency} \tag{4.1}$$

This method is capable of determining the elapsed time for a code segment, or the entire code. Taking the inverse of the elapsed time then is a simple measure of frame rate for the code segment or entire code.

With the process described above, early versions of the Gaussian bump remapping program were partitioned in an attempt to identify which code segments were the slowest to evaluate. Table 4.1

illustrates the evaluation time breakdown for different portions of the original code written, with remappings being performed on a 640 x 480 chromatic image.

Table 4.1: Initial Time Breakdown of Remapping Program

Code Segment Description	**Percentage of Total Time**
Initializing, creating containers, switch statement	0.0006
For loops populating mapping matrices	**85.459**
Write mapping matrices to gpu	1.6247
Performing remapping	0.7365
Writing gpu mat dst to cpu mat dst	0.4414
Flipping matrix for opposite origin	0.2756
Creating ellipse	0.2756
Col min/max and following conditionals	0.0748
Copying region of interest data to destination	0.0001
Displaying destination image	0.4401
Check for esc key	3.0869
Output statements	1.5435
Total	**93.6968**

From the table above we see that over 85% of the time was allocated to populating the horizontal and vertical mapping matrices, with approximately 6% of the time unaccounted for. From this conclusion a main thrust of the project became decreasing the amount of time needed to populate the mapping matrices, with the goal of obtaining frame rates greater than VHS quality (24 fps).

The first attempt to decrease matrix population time was to partition the screen space to an area that required remapping, with areas outside of this remapping area requiring none. With this approach, different widths, corresponding to differing multiples of the standard deviation of the Gaussian remapping function were tested to see if changing only a portion of the input image

would result in an adequate speed increase. An illustration of this method is shown below in Figure 4.1.

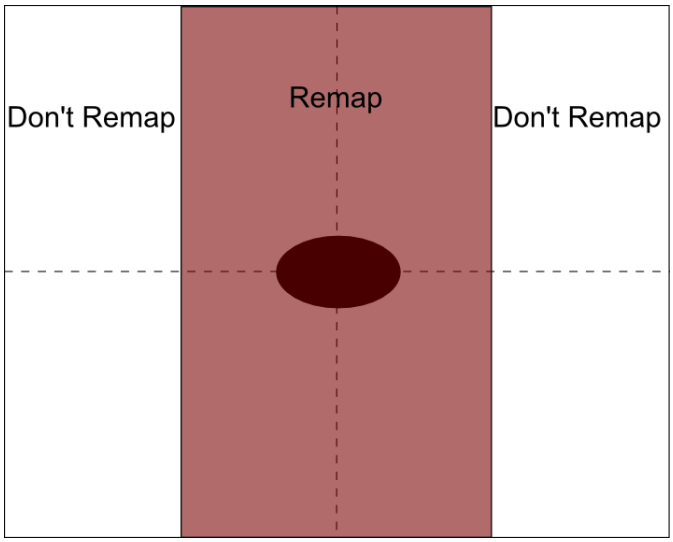

Figure 4.1: Partitioned Reverse Mapping

This partitioned remapping resulted in moderate speed increases, with the disadvantage that it left portions of the destination image distorted and discontinuous due to the fact that quick eye saccades would leave portions of the image unchanged that needed to be. This method was soon abandoned due to the jagged artifacts that it left behind due to quick eye saccades, and negligible speed increases.

The second attempt to increase mapping matrix population was the observation that the mapping between horizontal pixels in the source and destination matrices was a one to one relationship. Therefore, the horizontal locations could be mapped once, outside the scope of the continuous while loop, and merely assigned once every loop iteration. This operation alone reduced the mapping matrix population time by approximately 20%, but due to the fact that the computation of the vertical mapping component is much more computationally expensive, a large slowdown was still present. It is important to note that if a remapping were to be employed that was radially

symmetric this population outside the scope of the while loop would be invalid and would have to be returned to within the scope of the loop.

The next attempt to increase frame rate was to split the main process thread into multiple, parallel threads, execute the matrix population piecewise with each slave thread, then recombine the numerous slave threads again into the single main thread. This parallel for loop evaluation is depicted in Figure 4.2, where the slave threads are enumerated 1 through N.

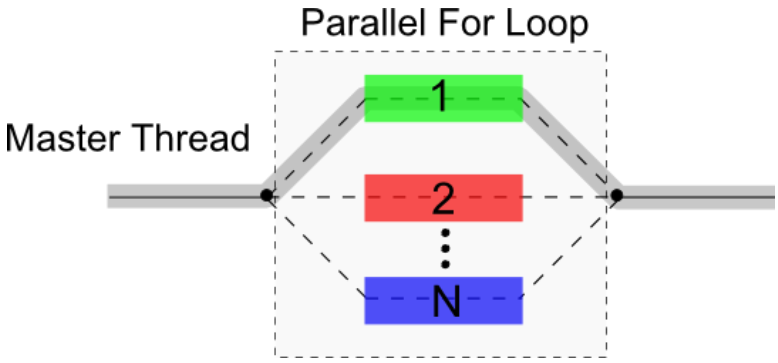

Figure 4.2: Parallel For Loop Thread Tracking

The number of threads created is dependent upon CPU usage, and is specified to create as many threads as possible until CPU usage is maximized. This effectively evaluates the embedded for loops that populate the mapping matrices as quickly as possible given the computing power available. This approach has the downfall of decreasing scalability to other devices, but for the purpose of prototyping a device is deemed sufficient.

The parallel for loop requires the enablement of OpenMP, the open source multi-processing API available with Microsoft Visual Studio. OpenMP allows programmers to easily implement multi-threading in programs created by splitting the process' master thread into multiple slave threads. When the multi-threaded task is completed the multiple slave threads recombine into the single master thread. The parallel for loop specified by OpenMP requires a pragma directive call before

evaluation and has the form: "#pragma omp parallel for ()". Following the parallel for call is a statement declaring variables that are private to each parallel for loop, "private (tx, ty, v)". Declaring these variables as "private" to the for loops is necessary in order to keep the order of evaluation, and thread recombination, consistent. If these variables are not declared as private, the matrices will be populated in a completely random fashion, and all meaning to data represented in the destination matrix will be lost. This is due to the fact that u and v, the remapping functions which populate the matrices, will be evaluated in a completely random order, and not in a numerical sequence corresponding to the index of the for loop. After creating the multi-threading capability within the program the code segment speed breakdown was as follows:

Table 4.2: Speed Break Down With Parallel For Loop Utilization

Code Segment Description	**Mean Time (s)**	**Percentage of Total Time**
Initializing, creating containers, switch statement	0.000055	0.0940
Reading source image	0.013800	23.6234
Write mapping matrices to gpu	0.000973	1.6653
Gazepoint operations	0.000002	0.0038
Creating ellipse and copying region of interest	0.000004	0.0065
Resize and write to ROI	0.000283	0.4845
For loops populating mapping matrices	**0.023500**	**40.2282**
gpu remapping	0.002500	4.2796
create ellipse, display image, check for esc key	0.017300	29.6148
calculated total	0.058417	100.0000
FPS	17.1183698	

The multi-threading described above resulted in a doubling of the performance of the for loops populating the mapping matrices, with an execution time consuming 40% of the total time compared to 85% of the total time. The multi-threading capability resulted in a new high for frame rate achieved of just over 17 frames per second.

In order to further make the program less computationally expensive, unnecessary pixel entries were removed from the iterative for loops which populate the mapping matrices in an attempt to decrease the number of floating point operations per while loop iteration. To further increase performance it was noted that the vertical remapping is indeed static, although the mean value in the Gaussian functions translates to match the user's gaze point as dictated by the eye trackers. To circumvent a complete repopulation of these matrices, a remapping method consisting of a fixed (global) mapping matrix was conceived, in which the fixed matrix is created to be of dimensions twice that of the incoming video frame. Every element within this matrix is populated with instructions to remap according to a Gaussian Bump distribution, with Gaussian mean at the center of the global matrix, i.e. corresponding to the point (src.cols, src.rows), where src.cols and src.rows are the width and height of the incoming video frame respectively. In this context cols and rows are members of the object src, which is of type cv::Mat, which has had the incoming video frame, or source image, assigned to it.

A secondary, local, mapping matrix is then defined within the limits of the global matrix. This local mapping matrix translates within the global matrix and samples elements from it such that the users gaze point coincides with the location of the Gaussian mean, i.e. it translates in response to the gaze point data sent from the ViewPoint eye tracker. It is this local mapping matrix that dictates what the user sees; in Figure 4.3 the user would be looking at the lower left hand portion of the screen. This has the considerable advantage of not needing to evaluate the equation for a Gaussian for every pixel (12 floating point operations per pixel); instead, it simply assigns pixel values from the global matrix to the local matrix (1 floating point operation per pixel). Figure 4.3 illustrates the two matrix remapping process. It should be noted that this algorithm is not restricted to the Gaussian Bump remapping currently being used; any point-to-point inverse, or forward, remapping may be used. In the case a different remapping was to be tested, all that

would be required is changing two lines of code assigning the horizontal and vertical remapping components of the mapping matrix.

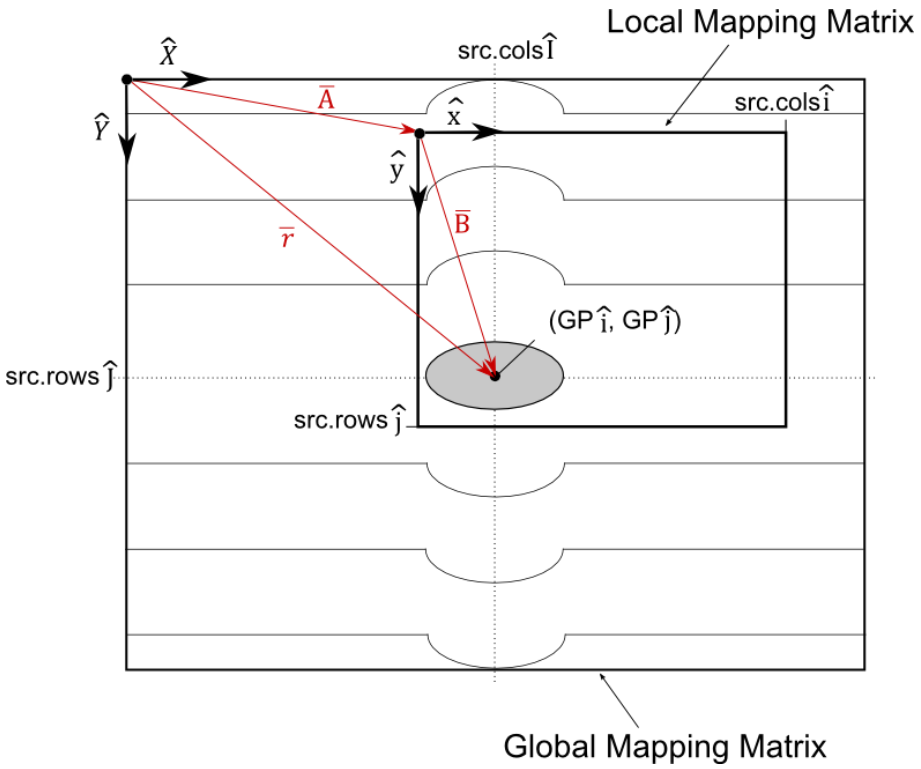

Figure 4.3: Two Matrix Gaussian Bump Remapping Algorithm

In Figure 4.3 above, $\hat{X}$, $\hat{Y}$ are the coordinate axes for the fixed, global, coordinate frame, $\hat{x}$, $\hat{y}$ are the coordinate axes for the local, translating coordinate frame, (GP $\hat{\imath}$, GP $\hat{\jmath}$) are the coordinates of the users gaze point in the local frame, $\bar{r}$ is the position vector from global origin to elliptical center in the global frame, $\bar{A}$ is the position vector from the global coordinate frame origin to the local coordinate frame origin, and $\bar{B}$ is the position vector of the users gaze point within the local coordinate frame. Due to the fact that global and local coordinate frame axes are always aligned, as noted in equations 4.2 and 4.3, the three position vectors easily create a closed vector loop of aligned, but offset, coordinate frame vectors, where the algorithm is capable of solving for position vector $\bar{A}$ with the known algebraic relations noted in equations 4.4 through 4.6.

$$\hat{X} \cdot \hat{x} = 1 \tag{4.2}$$

$$\hat{Y} \cdot \hat{y} = 1 \tag{4.3}$$

$$\bar{r} = src.cols\, \hat{I} + src.rows\, \hat{J} \tag{4.4}$$

$$\bar{B} = GP\hat{\imath} + GP\, \hat{\jmath} \tag{4.5}$$

$$\bar{A} = \bar{r} - \bar{B} \tag{4.6}$$

The frame rate benefits provided by this method of remapping used with the IDS UEye 3240CP machine vision camera are illustrated in Table 4.3 below. It should be noted that full resolution of the Sensics zSight head mounted display is 1280 x 1024.

Table 4.3: Frame Rate Comparison Using Two Matrix Remapping and Pixel by Pixel Remapping (grayscale)

Video Resolution	Frame Rate Using Two Matrix Method (FPS)	Frame Rate Using Pixel By Pixel Evaluation (FPS)	Frame Rate Performance Increase
1280 x 1024	10.1122	0.4311	2345.67 %
1280 x 960	11.0026	0.3881	2834.99 %
1024 x 768	16.4372	0.4176	3936.11 %
960 x 720	17.5302	0.4222	4152.11 %
800 x 600	22.5044	0.4646	4843.82 %
640 x 480	34.959	0.4724	7137.85 %
480 x 360	34.8764	0.4839	7003.06%
320 x 240	64.3256	0.5053	6815.86 %
240 x 180	67.2061	0.5341	6374.76 %

4.2 Noise and Disturbance Characterization and Removal

With a remapping algorithm created, a large problem facing the usefulness of the program was the large amount of noise corrupting the data sent by the eye tracker, as well as discontinuities in gaze point data resulting from wearer blinks. Disturbances due to blinks are attributable to the eye tracking software incorrectly identifying other parts of the eye as the pupil when it disappears behind the wearer's eyelids. First approaches to ameliorate the noise issue were to attempt to characterize the noise corrupting the position information and to then create an appropriate low pass filter to denoise the position signal.

Noise characterization was performed by taking series of discretely sampled position data in the time domain and performing a discrete Fourier Transform to obtain frequency domain data. Representative, low bandwidth, plots of this process are shown below in Figure 4.4.

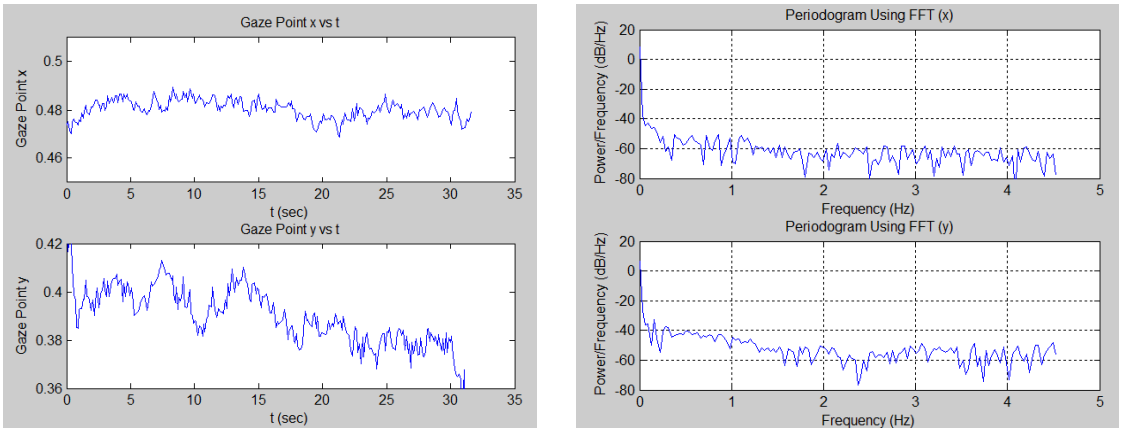

Figure 4.4: Sample Periodograms

As can be seen from the above representative figures, the noise appears to be white. With this being the case, it is difficult to set a desired cut off frequency for a filter being designed to denoise the position data. Without appropriate noise characterization, filter creation was based

around second order models of the human eye. Such models represent the human saccadic eye movement by fitting a second order system to obtained data. The maximum -3dB bandwidth for small, 5 degree, eye saccades was deemed to be approximately 17 Hz. [123] With this in mind, initial low pass filters created had a cutoff frequency of approximately 17 Hz.

4.2.1 Filtering Approach

Filter design was performed using Matlab's FDAtool filter creation tool. Initial filters were of the finite impulse response type due to their inherent bounded input – bounded output stability and linear group delay. FIR filters evaluated were equiripple, least-squares, windowed, complex equiripple, maximally flat, least Pth-norm and other equiripple variants. All of these FIR filters created exhibited a large group delay, albeit a desirable linear one. The delay introduced by these filters caused gaze point data to lag behind the user's actual gaze point so significantly that real time eye tracking became ineffective.

To obtain less delay, infinite impulse response low pass filters were subsequently evaluated. Of these, Butterworth, types I and II Chebyshev, elliptic, and maximally flat filters were designed. Minimum order realizations were created in an attempt to minimize group delay. Using maximally flat IIR filters, a minimum delay of approximately 3 samples was obtained. Second Order Section matrices and output gain values were created with FDATool to form these maximally flat filters. Difference equations corresponding to the cascade of the second order subsystems (biquad filters) were realized in the C++ workspace. With these classes of filters, delay was not very noticeable, but noise was not successfully attenuated from the signal, regardless of cutoff frequency designed for. Such a conclusion is not surprising due to the previous observation that the noise appears white.

4.2.2 Discretization Based Noise Rejection

Secondary, albeit very crude, approaches to rejecting noise corrupting gaze point data were to artificially discretize the amount that the elliptical simulated scotoma could translate in the user's window. This was achieved by setting a low and high threshold to the amount that the scotoma could translate in the horizontal and vertical directions, effectively creating a pass band. The magnitude of horizontal and vertical translation of the simulated scotoma between frames was then computed and compared against these high and low thresholds. If the translation was below the low threshold, the simulated scotoma would remain at the previous while loop iteration's location.

To remove high frequency component noise, the time history of gaze point data was analyzed and the magnitude of average noise in the vertical and horizontal directions was determined to be 0.0122 and 0.0144 respectively. It should be noted that these values are normalized values, ranging from 0 to 1, and are the ratio of position vector length from image origin to gaze point to total display window width and height. Therefore, a value of 0.01 in the horizontal direction represents a position looked at that is $1/100^{th}$ of the total width of the window. The nominal noise magnitude values of 0.0122 and 0.0144 were then used as a threshold to compare the change in gaze point position data from the previous frame to the current frame. If the change in position data is not larger than these thresholds, the new position data is discarded and the previous frame's position data is used to update the mapping matrices. This effectively re-discretizes the window to 82 points in the horizontal direction and 70 points in the vertical direction, as opposed to its native 1280 points in the horizontal direction and 1024 points in the vertical direction. These thresholds were then tuned from their nominal values until oscillations of the simulated scotoma were not perceived by wearers.

Similarly, if the difference between gaze point data between iterations was larger than the high threshold, the gaze point data would not be updated; this case was designed to eliminate discontinuities in scotoma location caused by blinking. In order to obtain a quantitative upper limit on the magnitude of scotoma translation for data of good quality, data was collected with the eye repeatedly saccading between the horizontal limits of the screen as quickly as possible. This type of saccade corresponds to that of repositioning the eye to the next line of text. Evaluation of this data determined that an approximate upper bound, given the frame rate, for eye saccades would be between 0.3 and 0.4, normalized to the width of the screen. Therefore, approximately $1/3^{rd}$ of the screen was measured to be capable of being traversed by the eye between while loop iterations. With this in mind, the upper limit on gaze point was nominally set to 0.3 and tuned thereafter.

This methodology was semi-effective at removing noise presented to the user, but resulted in a noticeable discretization as the simulated scotoma would no longer translate smoothly. Ultimately, this proved to be a rather large downfall for the ability to only reject some blinks, just over half, but effectively removed most noise by masking it. Due to these shortcomings other approaches were investigated.

4.2.3 Histogram Comparison Techniques

After attempting numerous lowpass filters of differing cutoff frequency and artificially masking the noise, other methods of ensuring the quality of the gaze point data sent to the program were investigated. These approaches were aimed at rejection of data with quality representative of an inappropriate pupil fit due to a blink. Of these methods, multiple programs were created utilizing the API corresponding to the Sensoray s2255 frame grabber to gain direct access to the camera

feed facing the wearer's eye. Once video feed was accessible, numerous comparison techniques were coded in the C++ language to compare images of the wearer's open eye. Seven techniques were developed that consisted of saving an image of the user's open eye and comparing them in different ways to the current video frame being sent from the camera inside of the HMD. Four of these techniques consisted of creating an image histogram of the open eye image and the current video frame pixel intensities and comparing the histograms using one of four different comparison metrics. The four histogram comparison metrics evaluated were correlation, chi-square, intersection and Bhattacharyya distance as indicated in equations 4.7 and 4.9 through 4.11 respectively. [101]

$$d(H_1, H_2) = \frac{\sum_I (H_1(I) - \bar{H}_1)(H_2(I) - \bar{H}_2)}{\sqrt{\sum_I (H_1(I) - \bar{H}_1)^2 \sum_I (H_2(I) - \bar{H}_2)^2}} \tag{4.7}$$

$$\bar{H}_k = \frac{1}{N} \sum_J H_k(J) \tag{4.8}$$

Where N is the total number of histogram bins

$$d(H_1, H_2) = \sum_I \frac{(H_1(I) - H_2(I))^2}{H_1(I)} \tag{4.9}$$

$$d(H_1, H_2) = \sum_I \min(H_1(I), H_2(I)) \tag{4.10}$$

$$d(H_1, H_2) = \sqrt{1 - \frac{1}{\sqrt{\bar{H}_1 \bar{H}_2 N^2}} \sum_I \sqrt{H_1(I) \cdot H_2(I)}} \tag{4.11}$$

The simple correlation method returns 1 for a perfect match, -1 for a perfect mismatch, and 0 for perfectly uncorrelated data. The chi-square method returns 0 for a perfect match between kernel and source image, with a theoretically unbounded maximum, dependent upon image size and data type, returned for mismatched data. Pragmatically the chi-square method will simply return a large number for mismatched data, in the case of an open and closed eye comparison of a 320 x

240 monochromatic image, the resolution of the forward facing camera, this value had a mean of 910,775. The intersection method returns 1 for a perfect match and 0 for a perfect mismatch. The final method, Bhattacharyya distance, returns 0 upon a perfect match, with a perfect mismatch returning 1.

The above comparison methods all proved successful at detecting wearer blinks, with the chi-square type having the highest resolution and greatest resolving power in detecting a blink from an open eye. This very high resolution is due to the theoretically unbounded value returned by mismatched objects. When 40 blinks were presented to the program utilizing the chi-square histogram comparison method, all 40 blinks were detected.

4.2.4 L_1 and L_2 Error Norm Approach

Due to the fact that histogram comparison does not directly measure the difference between two images, it measures the difference between the histogram of image intensities, other comparison techniques were investigated. Of these, L_1 and L_2 error norms, alternatively known in the computer science field as sum of absolute differences and sum of squared differences, were computed on a pixel by pixel basis. Additionally a normalized cross-correlation approach was investigated; this and the aforementioned norm based approaches are described in equations 4.12 through 4.14 respectively.

$$SAD(I_1, I_2) = \|I_1 - I_2\|_1 = \sum_i |I_{1i} - I_{2i}| \tag{4.12}$$

$$SSD(I_1, I_2) = \|I_1 - I_2\|_2^{\,2} = \sum_i (I_{1i} - I_{2i})^2 \tag{4.13}$$

$$R(I_1, I_2) = \frac{\sum_{x,y} I_1(x,y) \cdot I_2(x,y)}{\sqrt{\sum_{x,y} I_1(x,y)^2 \cdot \sum_{x,y} I_2(x,y)^2}} \quad (4.14)$$

In the above equations I_1 and I_2 are pixel intensities at the corresponding location in the first and second image (the template image and current video frame).

These error norm based approaches proved to also be successful in detecting blinks, when the template presented was an image of the wearer's open eye, with 38 out of 40 blinks being detected. The run time for the histogram based approaches, although not measuring differences between images on a pixel by pixel basis, proved to be much faster than the pixel by pixel approaches.

4.2.5 Data Quality Code Approach

Ultimately, comparison methods utilizing video feed from the HMD's internal camera were abandoned due to the fact that the video feed thread could not be shared between the eye tracking software and the developed comparison program. When this thread was forced to be shared between the different programs, dependent upon which was opened first, one would malfunction, or the computer would dump to a "blue screen of death". If the eye tracking program was run first, then the remapping program executed, the computer would dump. If the remapping program was running before the eye tracking program, the eye tracking window would have duplicate video feeds displayed, and no output would appear to the user from the remapping program. In the future, if blink detection is required, the above methods have proved to be an accurate and effective means to detect when a user blinks, so long as video feed is not required to be shared.

After observing the behavior of the ellipse / oval fit to the wearer's pupil it was concluded that much of the noise was the result of uncertainty within the program as to where the pupil was actually located. Parameters that were influential to the determination of the pupil, which is performed using a Hough transform, were noted and operating limits that would prevent location uncertainty were conceived. The aforementioned notion lead to the last approach, that of tuning parameters set within the ViewPoint workspace to send data quality codes that can be interpreted by the developed application as detected wearer blinks. These parameters are coded using the viewpoint command line interface (CLI), and were tuned based on relationships made between blinks and the values these parameters took. These values include the type of shape fit to the pupil, in this case an oval as opposed to an ellipse, the minimum pupil width searched for, the maximum pupil width searched for, the minimum ratio of pupil height to pupil width (known as the pupil aspect ratio), maximum measured pupil velocity, the geometric window size and location in which to search for the pupil, and infrared brightness and camera contrast of the camera facing the wearer's eye.

The oval pupil fit method returns data better suited to evaluation of pupil aspect ratio. [92] For optimal data quality codes, the maximum pupil width has been set to 0.20, the minimum pupil width set to 0.07, the minimum pupil aspect ratio set to 0.59, and maximum pupil velocity set to 0.10. Further changes can be observed in the settings file, written using the viewpoint CLI instruction language, entitle "settings.txt", which are automatically loaded upon launching the viewpoint eye tracker. As part of calibrating the eye tracker to new users, the minimum and maximum pupil widths should be calibrated based on photopic and scotopic situations respectively, the pupil window should be selected based on how the HMD fits on the wearer's head, making efforts to only make the rectangle as large as needed to capture the pupil throughout its range of motion and avoiding features of the eye that can lead to false information about the

pupil's location such as the lacrimal caruncle. The pupil aspect ratio should be set to accommodate the perspective the eye tracker camera has of the user's eye, and the brightness and contrast set dependent upon the contrast between the user's pupil and iris; this contrast will become an issue for user's with a darkly colored iris.

With these values, data quality codes, which vary from 0 to 5 corresponding to the conditions set by the settings file, are shown below:

0: VPX_QUALITY_GlintIsGood, indicating that the glint and pupil fit are acceptable.

1: VPX_QUALITY_PupilOnlyIsGood, indicating that only the pupil fit is acceptable.

2: VPX_QUALITY_PupilFallBack, indicating the application wanted to use glint data, it was bad, but pupil data was good and that is being used instead.

3: VPX_QUALITY_PupilCriteriaFailed, indicating the pupil fit was bad because it exceeded operating criteria limits.

4: VPX_QUALITY_PupilFitFailed, indicating that the pupil could not be fit with an ellipse at all.

5: VPX_QUALITY_PupilScanFailed, indicating that the pupil scan threshold failed.

The viewpoint API command VPX_GetDataQuality2 (int EYE, int *data_quality), returns the appropriate integer corresponding to the conditions above. Corresponding to these codes, if VPX_GetDataQuality2() returns any integer larger than 2, the current gaze point data being sent to the application is not used as there is something fundamentally wrong with it. Upon setting these parameters and thresholds, nearly all high frequency noise was removed from the user's perception, and in a test of 40 blinks, none were sent to the screen as a discontinuity in gaze point position. With these conclusions, the error code based approach using parameters tailored to the

individual wearer of the device will be the method used to remove noise and ensure accurate pupil location.

4.2.6 Kalman Filtering

To further ameliorate gaze point measurement uncertainty, a Kalman filter has been designed to operate in conjunction with measurements from the eye tracker. The Kalman filter provides a recursive statistical framework for the estimation of an unknown system state, provided a given mathematical model of the system and noisy measurements. For the Kalman filter to be an optimal solution to the estimation problem noise must be Gaussian, zero-mean, uncorrelated, and white, i.e. having a constant spectral density. [124] It has been concluded from the creation of Periodograms, such as that included in Figure 4.4, that the Kalman filter is indeed an appropriate estimator choice with the noise meeting these statistical criterion.

The Kalman filter obtains an optimal estimate of a desired system state by minimizing the covariance of the estimation-error covariance, P_k,

$$P_k = E[(x_k - \hat{x}_k)(x_k - \hat{x}_k)^T] \tag{4.15}$$

where E is the expectation operator.

The state estimate is denoted $\hat{x}_k$, with the *a priori* state estimate denoted $\hat{x}_k^-$, and the *a posteori* state estimate denoted $\hat{x}_k^+$.

The eye tracker – eye system was modeled as an unforced linear discrete-time system as follows:

$$x_k = F_{k-1}x_{k-1} + w_{k-1} \tag{4.16}$$

$$y_k = H_k x_k + v_k \tag{4.17}$$

The noise processes w_k and v_k are assumed white, zero-mean, uncorrelated and with known covariance matrices Q_k and R_k, corresponding to the system process noise and system measurement noise respectively:

$$w_k \sim (0, Q_k) \tag{4.18}$$

$$v_k \sim (0, R_k) \tag{4.19}$$

where Q_k is the covariance matrix of the white acceleration defined as:

$$Q_k = E[w_k {w_k}^T] \tag{4.20}$$

For translational motion of constant velocity and random acceleration, Kohler [125] derives:

$$Q_k = \frac{\boldsymbol{a}^2 \Delta t}{6} \begin{bmatrix} 2\mathbf{I}(\Delta t)^2 & 3\mathbf{I}\Delta t \\ 3\mathbf{I}\Delta t & 6\mathbf{I} \end{bmatrix} s \tag{4.21}$$

where **I** is the 2x2 identity matrix, **a** is representative of the spectral amplitude of white noise, and s is indicative of units being in seconds. Empirically, Grindinger [126] has determined that for a similar eye tracking system a value of a = 100 appears adequate.

R_k, the covariance of the measurement noise, v_k, is defined as:

$$\begin{aligned} R_k &= E[v_k {v_k}^T] \\ &= \begin{pmatrix} E\left[X_{e,x}(t_k) X_{e,x}(t_k)\right] & E\left[X_{e,x}(t_k) X_{e,y}(t_k)\right] \\ E\left[X_{e,x}(t_k) X_{e,y}(t_k)\right] & E\left[X_{e,y}(t_k) X_{e,y}(t_k)\right] \end{pmatrix} \end{aligned} \tag{4.22}$$

where $X_{e,x}(t_k)$ and $X_{e,y}(t_k)$ denote random variables that describe the measurement error. For the assumed case of horizontal and vertical measurements being independent of one another, the off diagonal elements of R_k become zero, leaving:

$$R_k = \begin{bmatrix} {\sigma_{e,x}}^2 & 0 \\ 0 & {\sigma_{e,y}}^2 \end{bmatrix} \tag{4.23}$$

In the case of the Arrington Research eye tracker, the measurement error appears to be directly related to the known accuracy of the eye tracker, characterized as 0.5^{o} of visual angle. When compared to the 46.9^{o} horizontal and 37.5^{o} vertical field of view of the Sensics HMD, this accuracy is equivalent to 1.066% and 1.333% in the respective horizontal and vertical directions. Taking into consideration the screen resolution of 1280x1024 pixels, these error percentages result in an approximate pixel accuracy of ±14 pixels in both the horizontal and vertical directions. This pixel uncertainty then yields:

$$E\left[X_{e,x}(t_k)X_{e,x}(t_k)\right] = \frac{1}{29}\sum_{i=-14}^{14} i^2 \approx 70 \tag{4.24}$$

and

$$R_k = 70 \cdot \begin{bmatrix} 1 & 0 \\ 0 & 1 \end{bmatrix} \tag{4.25}$$

This formulation for the covariance of the system measurement noise is theoretically sound, but empirical results indicate that using

$$R_k = \begin{bmatrix} 1 & 0 \\ 0 & 1 \end{bmatrix} \tag{4.26}$$

yields better results.

The state vector, x_k, was chosen to be the horizontal and vertical position and their respective time derivatives, with the measurement vector, y_k, populated only by the horizontal and vertical position:

$$x_k = \begin{bmatrix} x_e \\ y_e \\ \dot{x}_e \\ \dot{y}_e \end{bmatrix} \quad , \quad y_k = \begin{bmatrix} x_m \\ y_m \end{bmatrix} \tag{4.27}$$

where the subscript ‘e’ denotes the estimated state, and the subscript ‘m’ denotes the measured value.

The F matrix, which is the discrete-time state transition matrix relating states x_k to x_{k+1}, was found using a simple linear integration scheme to propagate states forward in time:

$$F = \begin{bmatrix} 1 & 0 & \Delta t & 0 \\ 0 & 1 & 0 & \Delta t \\ 0 & 0 & 1 & 0 \\ 0 & 0 & 0 & 1 \end{bmatrix} \tag{4.28}$$

where Δt represents the sampling time of the eye tracker.

The observation matrix, H, provides the ideal (noiseless) mapping between the measurement vector and the state vector at time t_k, which takes the form:

$$H = \begin{bmatrix} 1 & 0 & 0 & 0 \\ 0 & 1 & 0 & 0 \end{bmatrix} \tag{4.29}$$

With the framework of the Kalman filter laid out, the filter is initialized with the initial state estimate being the center of the screen with zero velocity, and initial estimation-error covariance as unity along the diagonals, as follows:

$$\hat{x}_0{}^+ = [0.5 \quad 0.5 \quad 0 \quad 0]^T$$
$$P_0{}^+ = \mathbf{I}_4 \tag{4.30}$$

where $\mathbf{I}_4$ denotes the 4x4 identity matrix.

After the filter has been initialized, the Kalman recursion process takes place which evaluates the following set of equations at each time step, t_k:

$$
\begin{aligned}
P_k^- &= F_{k-1} P^+_{k-1} F^T_{k-1} + Q_{k-1} \\
K_k &= P^-_k H^T_K (H_k P^-_k H^T_k + R_k)^{-1} \\
\hat{x}^-_k &= F_{k-1} \hat{x}^+_{k-1} \\
\hat{x}^+_k &= \hat{x}^-_k + K_k (y_k - H_k \hat{x}^-_k) \\
P^+_k &= (I - K_k H_k) P^-_k
\end{aligned}
\tag{4.31}
$$

where K_k is the Kalman gain. The Kalman gain acts as a blending factor that weighs the quantity $(y_k - H_k \hat{x}^-_k)$, known as the innovations. The Kalman gain is inversely related to the measurement covariance, thereby reducing the weight on the innovation term if the measurement covariance is large, which is indicative of a poor quality measurement. Therefore, if the measurement covariance is large, the Kalman gain places a large emphasis on the value predicted by the dynamic model. Conversely, if the covariance is very small, the Kalman gain places emphasis on the value obtained by the measurement.

For a representative 37 second test period the Kalman filter resulted in the smoothing of data as indicated in the Matlab simulation shown in Figure 4.5.

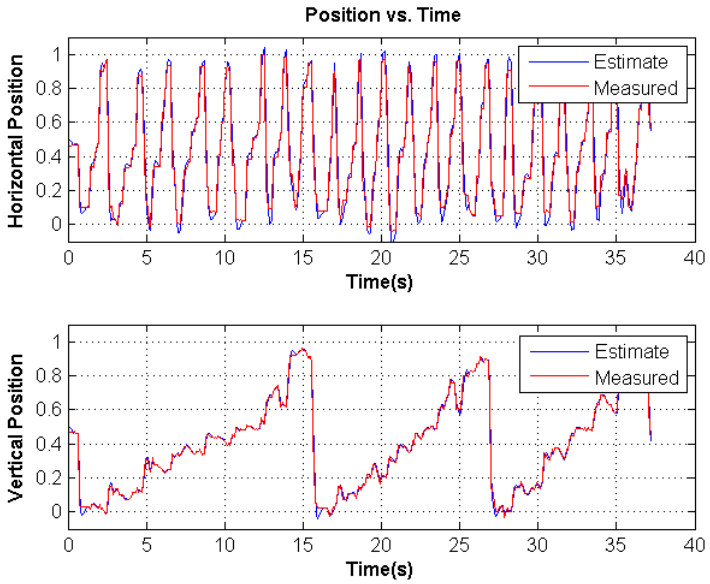

Figure 4.5: Kalman Filter Position Measurement and Estimate

4.2.7 Advanced Approaches

More advanced approaches investigated to detect user blinks included scale-invariant feature transforms, or SIFTs [127], Haar features, adaptive background mixture models [128], a non-dimensional, bounded symmetric agreement coefficient [129], Bhattacharyya distance based feature extraction [130], the Δ metric for grey-scale image comparison [131], a modified Hausdorff distance locally measured in an adaptive manner [132], and particle filters [133]. The majority of these approaches were not investigated further due to computational complexity and expense, although most are known to yield accurate results.

Chapter 5

Experimental Validation

5.1 **Experimental Design**

Initial pilot trials were run on normally sighted individuals using the Minnesota Low-Vision Reading Test, often simply called the MNRead test. [134] The MNRead visual acuity test is a continuous-text reading-acuity test used to evaluate reading acuity, critical print size, and maximum reading speed in low-vision and normally sighted individuals. [135] Reading acuity is a measure of one's ability to read decreasingly sized print until significant errors are made, critical print size is the smallest print the individual can read while maintaining maximum reading speed, and maximum reading speed is measured by the reading speed when not limited by reduced print size. Visual acuity is a measure of the spatial resolution of a human's visual processing system. A normally sighted individual, at a distance of 20 feet, will be able to resolve distinct contours that are approximately 1.75mm apart. The typical Snellen visual acuity chart, used as a cursory means to evaluate acuity at a primary care physician's office, defines normal vision as the ability to recognize an optotype, in this case the optotype is a letter, which subtends 5 minutes of arc.

Test sentences are designed to contain 60 characters each, including spaces, printed as three lines with even margins. The vocabulary of these sentences is selected based on frequency of use in 2^{nd} and 3^{rd} grade reading materials. Text is printed using a proportionally spaced font, in this case Times New Roman. Print size is measured using the height of a lower-case 'x' on a logMAR

scale as defined below. LogMAR charts derive their name from an acronym formed by the phrase “logarithm of the minimum angle of resolution”. LogMAR visual acuity is specified as the base 10 logarithm of decimal visual acuity, as indicated in equation 5.1, and is often the preferred method to measure visual acuity in research settings.

$$LogMAR := \log_{10}\left[\frac{(angle\ subtended\ by\ x - height)}{(5\ arc\ min)}\right] \tag{5.1}$$

A conversion chart from the typical visual acuity presented as a fraction in feet is presented in Table 5.1 below.

Table 5.1: Visual Acuity Conversion Chart

Foot	Meter	Decimal	LogMAR
20/200	6/60	0.1	1
20/160	6/48	0.125	0.9
20/125	6/38	0.16	0.8
20/100	6/30	0.2	0.7
20/80	6/24	0.25	0.6
20/63	6/19	0.32	0.5
20/50	6/15	0.4	0.4
20/40	6/12	0.5	0.3
20/32	6/9.5	0.63	0.2
20/25	6/7.5	0.8	0.1
20/20	6/6	1	0
20/16	6/4.8	1.25	-0.1
20/12.5	6/3.8	1.6	-0.2
20/10	6/3	2	-0.3

In order to calibrate the test sentences created to subtend the correct visual angle, relations to the visual field of view of the head mounted display and visual angle subtended were made, as described below. First, it was noted that the relation between visual angle and object height is:

$$\theta = 2\tan^{-1}\frac{S}{2D} \tag{5.2}$$

Where S in equation 5.2 is the distance from the corneal surface to the object being imaged, D is the height of the object being imaged and n is the distance from the corneal surface to retina, as shown in Figure 5.1. From table 2.1 n may be taken as 22.22

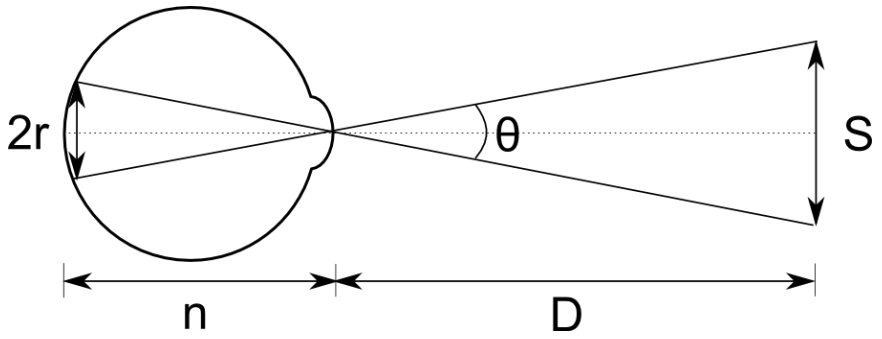

Figure 5.1: Visual Angle Schematic

Additionally, given the HMD's 46.9° horizontal field of view and 1280 pixel width, a geometric relation can be formulated using the visual angle subtended as follows:

$$\frac{\theta}{2} = \frac{46.9}{2} = 23.45 \tag{5.3}$$

$$\theta_{des} = 10^{logMAR}\left(\frac{5}{60}\right) \tag{5.4}$$

$$D = \frac{\frac{S}{2}}{\tan\frac{\theta}{2}} = \frac{640}{\tan 23.45} = 1475.42\ pixels \tag{5.5}$$

In equation 5.4 θ_{des} indicates the desired visual angle subtended by an object of size logMAR, corresponding to the logMAR number of the object.

The use of pixels in equations 5.3 through 5.5 refers to the distance from the corneal surface to the HMD internal displays, and is rather arbitrary; it is only used so that the height of the object imaged is also in the units of pixels.

We then have the relation between visual angle (deg) and pixel height stated in equation 5.6, where D is given in units of pixels, and θ_{des} is the desired visual angle subtended.

$$D \cdot \tan\theta_{des} = 'x' pixel\ height \tag{5.6}$$

Using the above relation, the height of the letter 'x' in pixels was tabulated as a function of visual angle, as indicated in Table 5.2

Table 5.2: Tabulated Values Relating Visual Angle (degrees) within the HMD to the Letter 'x' Pixel Height

LogMAR	Visual Angle	'x' Pixel Height
1.5	2.635	67.872
1.4	2.093	53.909
1.3	1.663	42.820
1.2	1.321	34.012
1.1	1.049	27.016
1	0.833	21.459
0.9	0.662	17.046
0.8	0.526	13.540
0.7	0.418	10.755
0.6	0.332	8.543
0.5	0.264	6.786
0.4	0.209	5.390
0.3	0.166	4.282
0.2	0.132	3.401
0.1	0.105	2.702
0	0.083	2.146
-0.1	0.066	1.705
-0.2	0.053	1.354
-0.3	0.042	1.076

With the rounded ‘x’ pixel heights listed above as goals, the letter ‘x’ was represented in Microsoft Word using Times New Roman font. Screen shots were taken of different point sizes, which were then magnified and the pixel height counted and recorded until the correct relationship between point size and pixel height was found. It is important to note that this was performed using the 1920 x 1080 display on an Asus G750JW laptop. A simple linear relationship was discovered between the point size and letter x height in pixels for the 1920 x 1080 display, as indicated in equation 5.7.

$$point\ size = \left(\frac{4}{3}\right) \cdot desired\ pixel\ height \tag{5.7}$$

With the correct Times New Roman point sizes identified to correspond to the range of logMAR values being tested, 44 sentences were created in Microsoft Word corresponding to these point sizes. Screen shots were taken of these sentences, which were then cropped to contain only the text.

Following the screen shots of the MNRead test sentences, a C++ program was created which programmatically accesses all images in a file folder, pads the image with white space so that the text is centered in the image such that output image is 1280 x 1024 in dimension (corresponding to the screen resolution of the HMD). Additionally, copies of these images are saved in a different file folder after Gaussian down pyramiding by a factor of 2 has been performed. Down pyramiding is used as a means to reduce the size of the image in an attempt to increase frame rates from just over 10 fps at full resolution, to just over 30 fps at half resolution. The latest frame rate tests recorded an average of approximately 33 frames per second for the MNRead tests with resolutions of 640 x 512.

Subrahamian and Pardhan showed that the MNRead test procedure has a coefficient of repeatability of ±0.05 logMAR when measuring visual acuity, ± 0.12 logMAR when measuring

critical print size, and ± 8.6 words per minute when measuring reading speed. [136] Furthermore, the authors concluded that no statistically significant changes in reading speed were observed as a result of altering the testing distance. It is therefore concluded that the MNRead test can be used reliably to measure reading acuity, critical print size, and reading speed.

Print subtending a visual angle equivalent to 1.0 logMAR was selected for use in the first round of experimentation on normally sighted individuals in order to minimize the perception of pixilation caused by Gaussian down pyramiding. This is equivalent to sampling every other pixel in the original image, then displaying this image in a way corresponding to every pixel being sampled twice. Experimentation participants were informed about eccentric reading prior to experimentation, and were given a maximum of 5 minutes to practice such techniques with the simulated scotoma toggled on. Additionally, participants were instructed to refrain from operating machinery or driving any vehicles for 30 minutes after experimentation to allow any symptoms of cyber sickness to fade.

As mentioned previously, absolute scotoma size has a recorded mean of 1.299 mm^2, while relative scotoma size has recorded mean of 8.943 mm^2. These two retinal areas were mapped to the HMD in a manner that would allow for the simulated scotoma to subtend the same visual angle that a circular scotoma with these areas would. These configurations will be known as the simulated dense scotoma, and simulated relative scotoma. Curcio et al. determined that a linear retinal length of 0.29mm could approximate 1 degree of visual span. With the approximation that the retina is a flat surface, the radii corresponding to 1.299 mm^2 and 8.943 mm^2 are 0.643 mm and 1.687 mm, which respectively subtend radii approximately 2.2^o and 5.8^o of visual span. [137] A simple geometric optics approach gives slightly smaller, but negligibly different, visual angles.

5.2 Experimental Setup and Procedure

With the concepts outlined in section 5.1, experimentation began by fitting the HMD on the participant's head, correctly adjusting the head strap height to align the HMD eye tubes with the participant's visual axes, and also correctly adjusting the head strap tension to constrain motion in the transverse plane. Calibration text was then presented in the HMD, at which point the internal correction of the HMD was altered by the participant, as well as the interpupillary distance, until the text appeared to be at its clearest. The Viewpoint eye tracking program was then launched, the selection window placed around the user's eye in a manner that minimizes the presence of shadows detected, and eye camera mode set to high precision (30Hz), as shown in Figure 5.2.

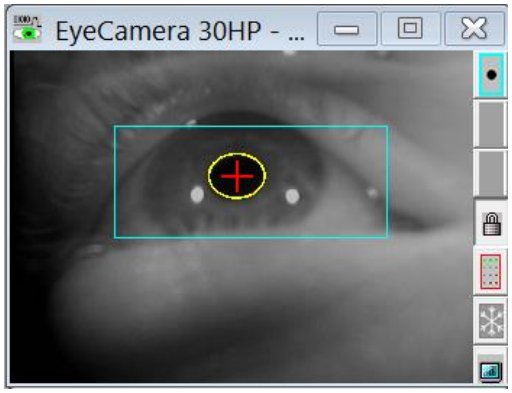

Figure 5.2: Detection window selection to minimize shadow detection

Note in the Figure above that the lacrimal caruncle, the small, pink nodule at the nasal aspect of the eye, is excluded from the selection window as it is dark and may cause pupil detection errors when the user blinks. The selection window is only made large enough to detect the pupil throughout its range of motion.

The wearer was then asked to slowly look at different corners of the display screen to ensure that thresholds on pupil fitting parameters, specifically maximum pupil width, minimum pupil width

and pupil aspect ratio, were not exceeded during normal circumstances. The calibration process was then initialized, and upon completion, the mapping between the gaze space and eye space was examined. If the mapping was not quasi-rectilinear, points were re-presented to the user until it was. A satisfactory example of a mapping relationship is shown in Figure 5.3.

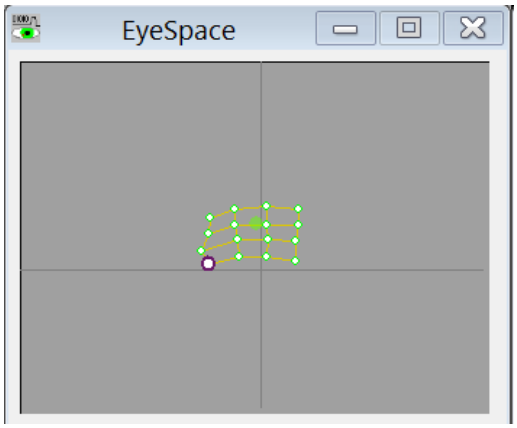

Figure 5.3: Satisfactory Eyespace mapping

Upon completion of the HMD fit and eye tracking calibration, the first MNRead sentence was displayed to the wearer, and the simulated scotoma was toggled on. The crosshairs of the curser were brought to the center of the screen and the wearer was asked to stare at them. DC biases were then removed so the user's gaze point, presumably the location of the cross hairs, was coincident with the simulated scotoma. Users were then allowed 8 slides, with a maximum time limit of 5 minutes, to try to become accustomed to reading. Additionally this allows the user to become familiar with wearing the HMD and the scotoma following their gaze point.

The participant was then instructed to read the following sentences aloud as quickly as they could. Once the new slide was presented timing began, and with completion of the last word timing was stopped. MNRead sentences 9-13 were presented such that no scotoma was present and no remapping occurred; this was recorded as their baseline maximum reading speed. Sentences 14-18 were presented with the smaller, dense, scotoma following their gaze point,

sentences 19-23 were presented with the dense scotoma following their gaze point and Gaussian bump remapping on, and 24-28 presented with the dense scotoma on, Gaussian bump remapping on, and a magnified region of interest along the periphery of the scotoma set at the user's preferred location. Similarly, sentences 29-33 were presented with the larger, relative, scotoma following their gaze point, sentences 34-38 were presented with the relative scotoma on and Gaussian bump remapping on, and sentences 39-43 with the relative scotoma on, Gaussian bump remapping on, and magnified region of interest set to the wearer's preferred location along the periphery of the scotoma. The aforementioned MNRead sentences are included in Appendix C. The scenarios of no scotoma, small and large scotoma, and small and large scotoma with remapping can be seen below in figure 5.4.

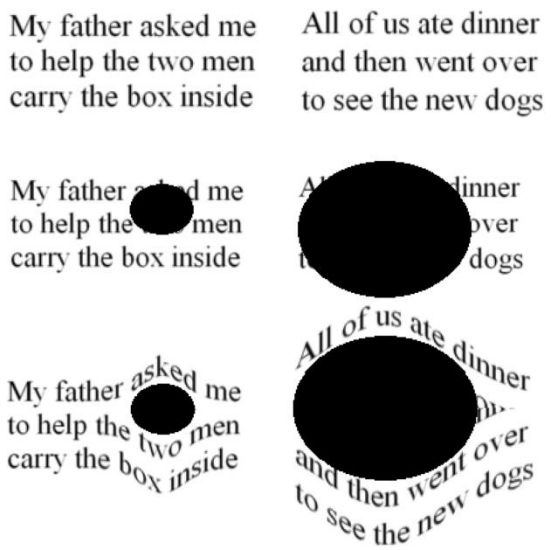

Figure 5.4: Simulated scotomas and corresponding remappings

Upon completion of the reading speed examination, participants were asked to describe any negative side effects as the result of reading with the HMD, simulated scotoma or remapping program.

Chapter 6

Results

6.1 **Experimental Results**

The primary objective of experimentation was to observe whether or not there was an immediate beneficial effect of the remapping program with a simulated scotoma on normally sighted individuals. The following two graphs, Figures 6.1 and 6.2, report the reading speeds for the two different sizes of simulated scotoma, with no scotoma, only the simulated scotoma, and the addition of the remapping to compensate for the simulated scotoma.

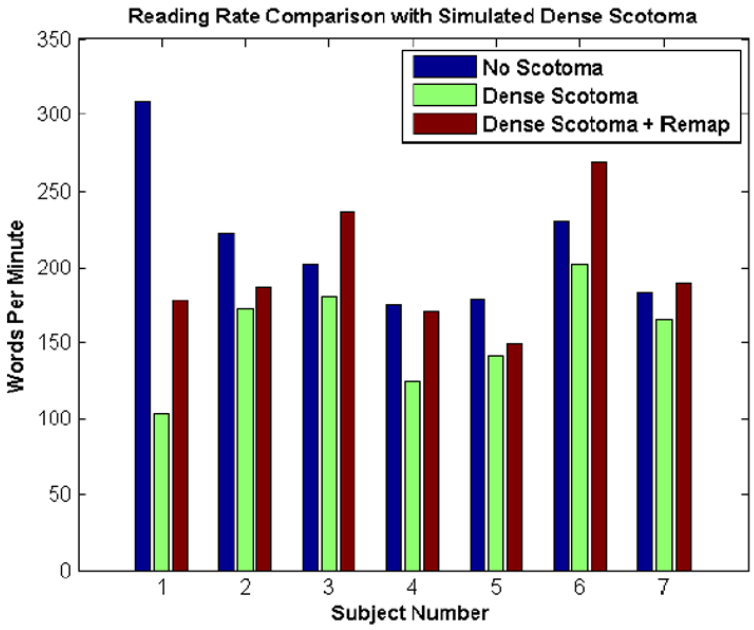

Figure 6.1: Reading rates for small sized simulated scotomas and remapping

All participants showed an increase in mean reading speed with the remapping program on to compensate for the dense scotoma. The increase in reading rate can be concluded to be due to the remapping with 99% confidence or greater ($p < 0.01$) in participants 1, 3, 4, and 6, with participant 7 having a 95% confidence interval, and participants 2 and 5 80%.

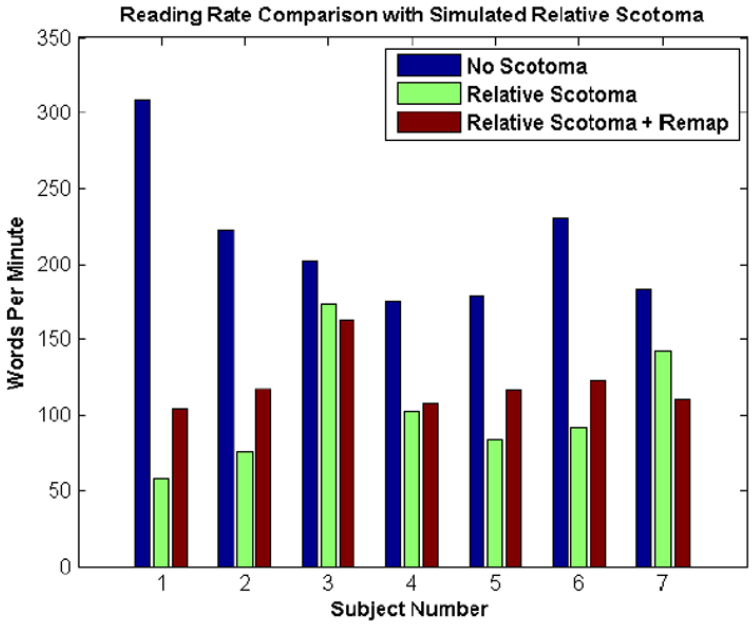

Figure 6.2: Reading rate for large simulated scotoma and remapping

With the larger of the two scotomas, all but two participants showed an increase in reading speed with the remapping. Those who experienced a decreased reading rate were observed to have difficulties with fixation stability. This fixation instability caused the words to alternate between locations above and below the simulated scotoma.

The reading rate change due to the relative sized remapping for participants 1 and 5 had confidence intervals larger than 99%, with 2 being at 95%, 6 being at 90%, and the remainder having confidence intervals of 80% or less. Overall, the remapping process resulted in a mean 31% increase in reading rate for the dense sized scotoma, and 34% increase in reading rate for the relative sized scotoma.

The secondary objective of experimentation was to determine whether or not a magnified region of interest, positioned at a preferred retinal locus, would be of benefit. It was predicted that this would serve as an impediment to normally sighted users, as it creates for a discontinuity in text flow, but could be beneficial to low vision users with training. The following two graphs, Figures 6.3 and 6.4, illustrate the relationship between reading rate with no scotoma, reading rate with an artificial scotoma, and reading with a simulated scotoma with remapping and region of interest toggled "on".

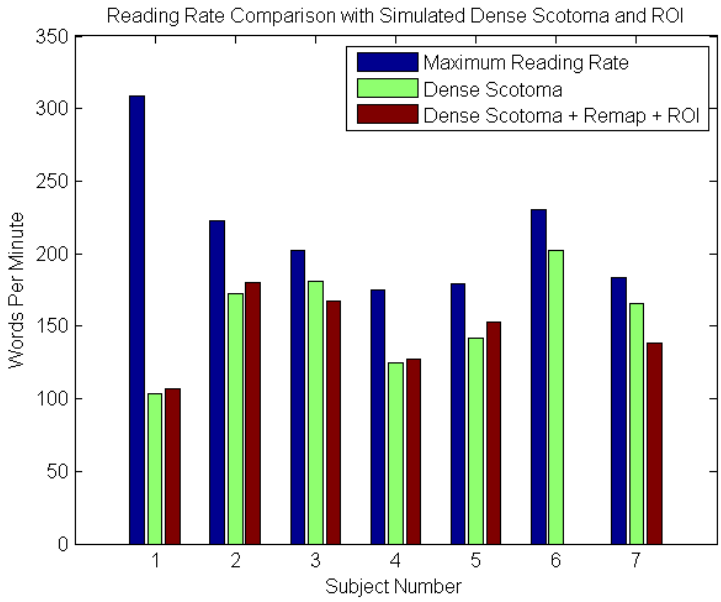

Figure 6.3: Magnified ROI at normally sighted user's preferred location, small simulated scotoma

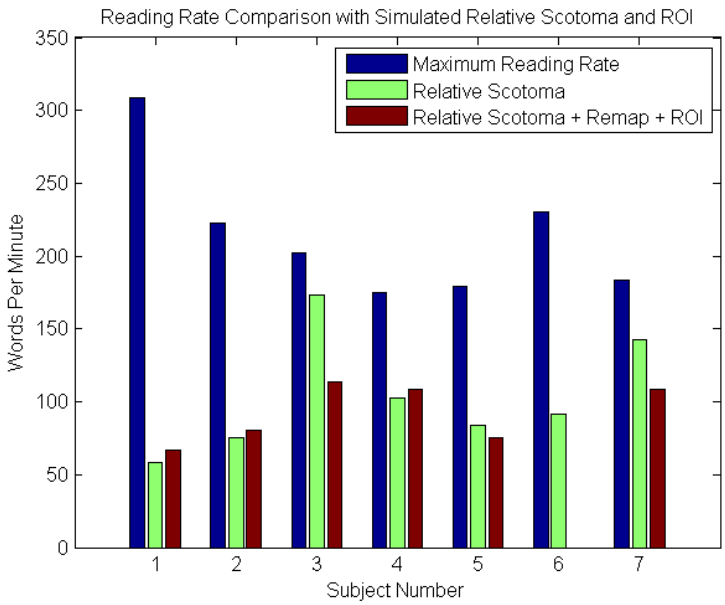

Figure 6.4: Magnified ROI at normally sighted user's preferred location, large simulated scotoma

It should be noted that participant number 6 had very dark eyes, making eye tracking using a Hough transform very difficult due to low contrast between the pupil and iris. With this difficulty present, the magnified region of interest was skipped for this individual. Participants 1, 2, 4 and 5 for the dense scotoma, showed a slight mean reading speed increase, but none of which proved to be of any statistical significance. Participants 3 and 7's pronounced decrease in reading speed can be attributed to the presence of the ROI ($p < 0.01$).

When asked to describe the qualitative difference between reading with an artificial scotoma and reading with an artificial scotoma corrected for by the remapping process, all users, excluding those who experienced fixation instability, reported that the remapping seemed beneficial due to the fact that information was not lost behind the simulated scotoma.

Fixation stability may also be used as a metric to evaluate performance. The following plots show the smoothed gaze point data for reading with no scotoma, reading with a large artificial scotoma, and reading with a large scotoma being compensated for by the remapping.

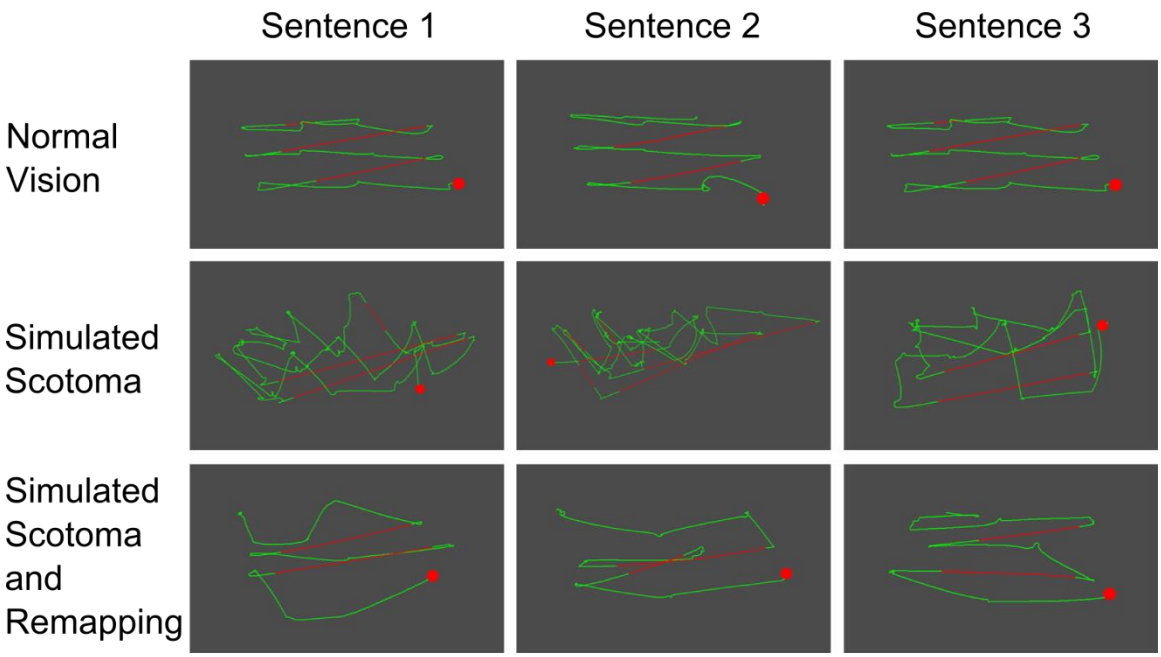

Figure 6.5: Gazepoint data plots

In figure 6.5, each column corresponds to a different MNRead sentence read, while the first row is indicative of reading with no visual field defects, the second row corresponds to reading with a simulated central scotoma, and the last row to reading with a simulated scotoma and remapping on. The red lines correspond to saccades that are associated with re-foveating at the beginning of a new line of text, while green is indicative of non-saccadic eye movements. It is easily seen that from this data that fixation stability is greatly enhanced for the normally sighted user when the remapping is on.

Representative position and acceleration data for the horizontal and vertical directions is shown in Figure 6.6. The left most series of plots corresponds to reading without any central visual field defects, the middle series of plots represents reading with a simulated large scotoma, and the last series represents reading with the scotoma being corrected for by the software developed.

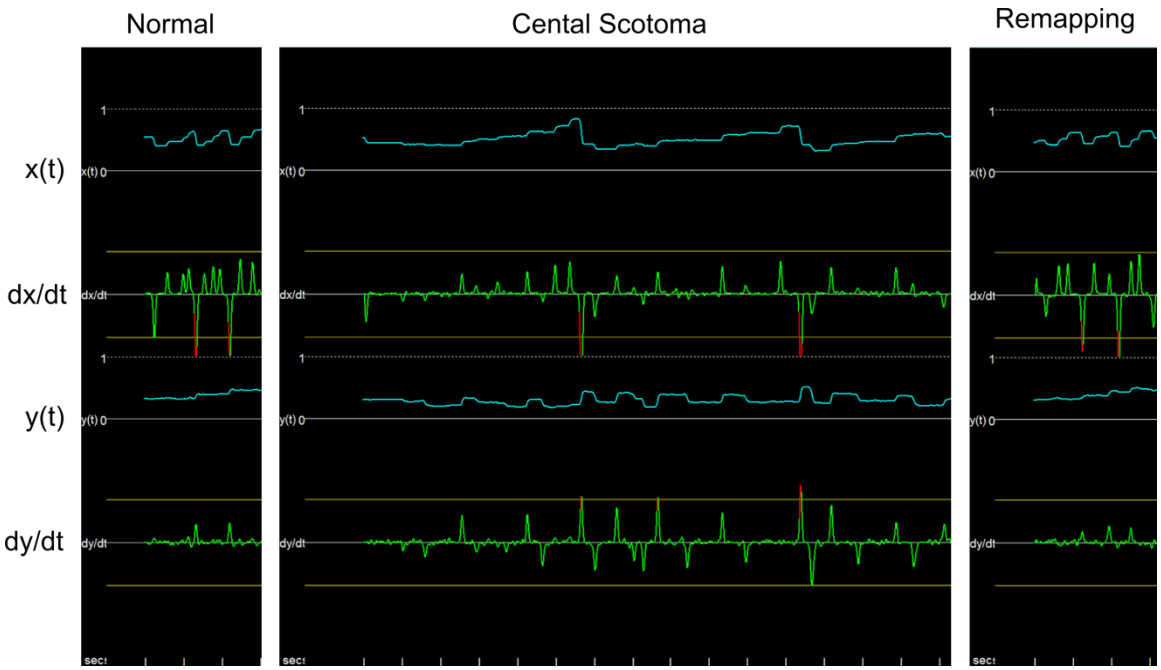

Figure 6.6: Gaze point position and acceleration data

It is interesting to note the marked difference in the vertical position data (with positive y downards) between the data from reading with no artifical scotoma, reading with a simulated central scotoma, and reading with the remapping on to compensate for the central visual field defect. The sawtooth pattern in horizontal position data (1st row) is typical for the eye scanning from left to right across text, and repositioning again at the left side of the screen to read the next line of text. As expected, there is a stepped pattern to the vertical position data (3rd row), as the eye goes from the the first line, to the second, to the third. This pattern is difficult to extract from the vertical position data from the plotted positions accompanying the plots representing reading with the simulated central scotoma due to this user's preference to try to read text below the scotoma, and then reposition the eye to foveate on the text once it is visible in their peripheral vision.

6.2 **Adverse Side Effects**

Participant number 3 complained of a headache due to the unfamiliar optics and inability to correct for astigmatism, but these side effects diminished within 10 minutes of removing the HMD. Participants 5 and 6 reported that their eyes "felt funny" after completion of the testing, but nothing more was present. The remainder of participants reported no side effects following testing.

Chapter 7

Conclusions and Discussion

7.1 **Overview of Current Methodology**

The current methodology consists of using an inverse warping procedure to remap a source image in a manner that would redistribute light normally incident upon the fovea to a parafoveal region of the retina. The current embodiment of this warping function remaps data in the source image according to a Gaussian distribution that is centered at a point coinciding with the user's mapped gaze point. The pupil segmentation and mapping between the user's detected pupil and the determined normalized screen coordinates are carried out by Arrington Research's ViewPoint Eyetracker. The remapped image is then displayed on the internal monitors of a Sensics zSight head mounted display, which is equipped with the eye tracking system.

The remapping is carried out using a fixed matrix of dimensions 2n x 2m, populated with remapping instructions, and a translating matrix of dimensions n x m that samples remapping instructions from the fixed matrix. The translating matrix dimensions n and m correspond to the vertical and horizontal resolution of the source frame being remapped. The translating matrix moves in accordance with gaze point data retrieved using the viewpoint API.

Noise removal of gaze point data has been performed using data quality codes that are flagged if parameters set to the individual's eye are not met. Such parameters must be calibrated on an individual to individual basis.

7.2 Conclusions

From the qualitative description reported from the normally sighted test subjects, a remapping according to a Gaussian distribution appears to be of benefit when presented with an artificial central scotoma. The evidence provided by the fact that all users experienced an increased reading rate with the smaller of the two simulated scotoma size, and 5 of the 7 users experienced an increased reading rate with the larger of the two sizes further supports this qualitative claim. Furthermore, fixation stability is increased when reading with the remapping program compensating for a simulated central scotoma as compared to reading with a simulated central scotoma alone.

As predicted, the use of a magnified region of interest adversely affected normally sighted individuals. This is due to the fact that no users were able to read using the ROI and it simply served as another visual field defect for them to avoid. It is still believed that this magnified ROI will be beneficial for use with low vision patients given a correct training regimen

7.3 Discussion

It appears that some individuals may have been able to cheat with the small scotoma by getting a glimpse of the word to be read before the simulated scotoma reached that point. This notion comes from the observation that some individuals showed very little decrease in reading speed with the “dense” sized scotoma on. Further evaluation of this claim will need to be performed in the future.

In a few of the participants the reading speed with the remapping process compensating for the artificial scotoma meets or exceeds their reading rates with no simulated visual defects for the case of the small sized artificial scotoma. One possible reason for this is that the user has not fully become used to reading the test sentences aloud while recording their maximum reading rate, as this is recorded first. Additionally, this observation could be a possible cue that the small sized artificial scotoma is not large enough to have enough of an effect on reading rate for the large text being used to evaluate this metric.

Further observations were that the fixation stability with the artificial scotoma appeared to progressively increase with each successive MNRead sentence presented. This observation is aligned with findings from Varsori et al. and Legge who concluded that normally sighted individuals rapidly develop a PRL to accommodate for an artificial central scotoma. [138] The PRLs developed by individuals in this study were typically below the simulated central scotoma, 5, with 2 being above; none were to the left or right of the scotoma. This observation is also reinforced by findings from Varsori et al. who concluded that most PRLs in response to an artificial central scotoma manifested above or below the scotoma.

7.4 **Future Work**

Main thrusts of future work should consist of the following:

1) Further optimize frame rates to try to achieve 30 frames per second with full resolution chromatic images. A possible means to do this would be by using a field programmable gate array (FPGA) or code written entirely in CUDA to operate on a GPU.
2) Some users complained about the physical components of the eye tracking system digging in to their cheek while trying to read. Investigation of other eye tracking systems

would be beneficial. Specifically, a more user friendly form factor and ability to accurately calculate eye position regardless of iris color (such as using Purkinje images), and effectively remove biases should be used as items of importance when looking at eye tracking systems.

3) Design for the added complexity of binocular cameras capable of adjusting to the users IPD, therefore creating 3 dimensional views of the ambient environment. A second camera brings the obvious computational burden of necessarily remapping twice as many pixels, and would therefore likely need a secondary computer to perform the remapping. Furthermore, for cameras with wide angle lens, distortions will be present. These distortions can be easily removed by calibrating the camera to a rectilinear checkerboard pattern and using OpenCV to remove bulge / barrel distortions. Of further consideration with this approach is the vergence angle to set the cameras to.
4) Create provisions for video see-through capability. Head mounted displays using the principle of "video see-through" typically replicate the distance from the display plane to the retinal plane by using mirrors that are the same distance from the camera sensor plane. In doing so, the images displayed to the user appear to be the correct distance away; as opposed to appearing like a camera is capturing the images a few inches from their eyes and then re-displaying that information to them. Publications describing these capabilities are included in references [139] and [140].
5) Create further mapping matrices and evaluate their efficacy. Again, metrics used to evaluate the mappings themselves should be those defined using eigenvalue decomposition, and metrics used to evaluate their efficacy should be reading rate, fixation stability, and perhaps an optimality condition using the path integral of the eye's gaze point.

6) Try to increase comfort in the design and reduce the form factor of the apparatus. If additional mass due to sensors are added to the front of the HMD, a simple moment balance should be performed to ensure that the user does not experience neck strain, and also prevent the HMD from sliding off the wearer's head. If additional mass needs to be added to balance moments it should be added in the respective places.

7) A differing method of removing DC biases should be conceived due to the fact that low vision users would not be able to fixate on icons that are placed in their central visual field. Similarly, calibration of the eye tracker to low vision patients may prove troublesome as they will have a pronounced difficulty in fixating on the squares used to calibrate the eye tracker to their visual space. One conceived method to ameliorate this is by creating visual cues in the user's peripheral vision that allow individuals with central visual field defects to interpolate the central point they should be fixating at. An example of this is included in figure 7.1.

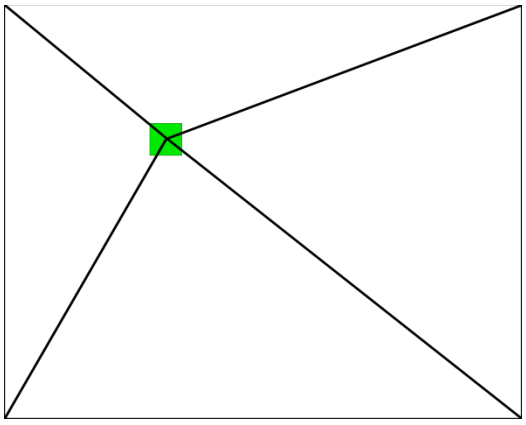

Figure 7.1: Peripheral visual cues for calibration and bias removal

Figure 7.1 depicts the screen coordinate frame viewed by the wearer, with the green square represents the calibration optotype presented to the wearer while calibrating the eye tracking system. The lines originating from the extrema of the screen space instruct the wearer to gaze

upon their interpolated intersection, even if that intersection is not visible to the wearer. This method is also a viable means to remove constant biases associated with the gaze point data.

8) During the work described in this thesis, the Oculus Rift was unavailable as a consumer product. The consumer version of the Oculus Rift is expected to have a nearly 100 degree field of view, and currently Arrington Research is developing an eye tracking system, similar to that currently used, to be used in conjunction with the Rift. Due to the fact that the Rift is reported as being light weight, comfortable, having a superior field of view, and is expected to have a retail value of approximately $300, further prototypes should look to the Oculus Rift as a potential development platform. Care should be taken to ensure that the optics and screens within the Rift are of equivalent quality to those within the zSight.
9) Integrate the designed Kalman filter into the written C++ program.

References

[1] E. Marieb, J. Mallatt and P. Wilhelm, Human Anatomy, Benjamin-Cummings Pub, 2007.

[2] University of Minnesota College of Pharmacy, "Eye Anatomy Continuing Education," [Online]. Available: http://teaching.pharmacy.umn.edu/courses/eyeAP/Eye_Anatomy/AssociatedStructures/Vitreous.htm. [Accessed 20 February 2014].

[3] National Eye Institute, "Facts about Uveitis," 2011. [Online]. Available: https://www.nei.nih.gov/health/uveitis/uveitis.asp. [Accessed 2014].

[4] C. Albarran, A. Pons, A. Lorente, R. Montes and J. Artigas, "Influence of the Tear Film on Optical Quality of the Eye," vol. 20, no. 4, pp. 129 - 135, 1997.

[5] Optical Society of America, "Handbook of Optics, Volume 1: Fundamentals, Techniques, and Design. Second Edition," in *Chapter 24: Optics of the Eye*, McGraw-Hill Professional, 1994.

[6] Y. Le Grand and S. El Hage, Physiological Optics, Springer, 1980.

[7] H. Emsley, Visual Optics, Hattan Press, 1963.

[8] E. Hecht and A. Ganesan, Optics, Fourth Edition, Pearson Education, 2008.

[9] J. L. Fitzakerley, "Vision Notes: The Eye," 2008.

[10] P. L. Penfold and J. M. Provis, Macular Degeneration, New York, NY: Springer, 2005.

[11] C. Curcio, A. Kimberly, K. Sloan, C. Lerea, J. Hurley, I. Kock and A. Milam, "Distribution and morphology of human cone photoreceptors staind with anti-blue opsin," vol. 312, pp. 610-624, 1991.

[12] Urban Eye MD Associates, "Age-Related Macular Degeneration," 2011. [Online]. Available: http://www.urbaneyemd.com/glossary_details.php?id=77#. [Accessed

2014].

[13] E. Self, "Color Vision Deficiencies," [Online]. Available: http://psych.fullerton.edu/eriko/research/ColorVision.html. [Accessed 2014].

[14] D. Friedman, B. O'Colmain, B. Munoz, S. Tomany, C. McCarty, P. de Jong and B. Nemesure, "Prevalence of age-related macular degeneration in the United States," vol. 129, no. 9, p. 1188, 2011.

[15] "Dry AMD," 2003. [Online]. Available: https://courses.cit.cornell.edu/psych431_nbb421/student2006/mpl33/dryAMD.htm. [Accessed 2014].

[16] A. Khanifar, S. Bearelly and S. Cousins, "Treatment of Dry AMD: The Next Frontier," 1 11 2007. [Online]. Available: http://www.nysoa.org/index.php?page_id=132. [Accessed 2014].

[17] "Facts About Age-Related Macular Degeneration," National Eye Institute, July 2013. [Online]. Available: https://www.nei.nih.gov/health/maculardegen/armd_facts.asp. [Accessed 20 February 2014].

[18] "The Amsler Grid," Lighthouse International, 2014. [Online]. Available: http://lighthouse.org/about-low-vision-blindness/amsler-grid/. [Accessed 20 February 2014].

[19] J. Fujimoto, C. Pitris, S. Boppart and M. Brezinski, "Optical Coherence Tomography: an emerging technology for biomedical imaging and optical biopsy," vol. 2, no. 1, pp. 9-25, 2000.

[20] D. J. Creel, "The Electroretinogram and Electro-Oculogram: Clinical Applications," 2011. [Online]. Available: http://webvision.med.utah.edu/book/electrophysiology/the-electroretinogram-clinical-applications/. [Accessed 20 February 2014].

[21] W. Seiple, R. Rosen and P. Garcia, "Abnormal Fixation in Individuals With Age-Related Macular Degeneration When Viewing an Image of a Face," vol. 90, no. 1, pp. 45-56, 2013.

[22] M. Crossland, L. Culham and G. Rubin, "Fixation stability and reading speed in

patients with newly developed macular disease," vol. 24, no. 1, pp. 327-333, 2004.

[23] F. Duret, M. Issenhuth and A. Safran, "Combined use of several preferred retinal loci in patients with macular disorders when reading single words," vol. 39, pp. 873-879, 1999.

[24] M. Crossland, L. Culham, S. Kabanaroi and G. Rubin, "Preferred retinal locus development in patients with macular disease," vol. 112, pp. 1579-1585, 2005.

[25] D. Fletcher, R. Schuchard and L. Walker, "Patient awareness of binocular central scotomas in age-related macular degeneration," vol. 89, pp. 1395-1398, 2012.

[26] R. Schurchard, "Adaptation to macular scotomas in persons with low vision," vol. 49, pp. 870-876, 1995.

[27] "Treatment Options for Wet AMD," [Online]. Available: http://www.amd.org/what-is-amd/wet-amd/what-are-my-treatment-options.html. [Accessed 20 Frebruary 2014].

[28] "Anti-Angiogenic Treatments," [Online]. Available: http://www.scienceofamd.org/treat/.

[29] "Focal Laser Photocoagulation," 2010. [Online]. Available: http://www.eyecentersofsetexas.com/plaza_10_location/treatments.php?qi=67.

[30] N. Bressler, "Photodynamic therapy of subfoveal choroidal neovascularization in age-related macular degeneration with verteporfin," vol. 119, pp. 198-207, 2001.

[31] N. Orzalesi, C. Pierrottet, S. Zenoni and C. Savaresi, "The IOL-VIP System: a double intraocular lens implant for visual rehabilitation of patients with macular disease," vol. 114, pp. 860-865, 2007.

[32] "IOL-VIP Procedure," [Online]. Available: http://www.grangeeyeconsultants.com/iolvip-procedure.htm. [Accessed 2014].

[33] "Implantable Telescope Technology," 2014. [Online]. Available: http://www.centrasight.com/technology. [Accessed 2014].

[34] "Implantable Telescope Technology," 2014. [Online]. Available:

http://www.centrasight.com/technology. [Accessed 2014].

[35] H. Hudson, R. Doyle Stulting, J. Heier, S. Lane, D. Change, L. Singerman, C. Bradford and R. Leonard, "Implantable telescope for end-stage age-related macular degeneration: Long-term visual acuity and safety outcomes," vol. 146, pp. 664-673, 2008.

[36] "Explorer HD," 2014. [Online]. Available: http://www.magnisight.com/exp_hd.html. [Accessed 2014].

[37] "Transformer USB," 2014. [Online]. Available: http://www.adaptivetr.com/transformer-usb. [Accessed 2014].

[38] "Gottlieb Visual Field Awareness System," Low Vision Centers of Indiana, 2014. [Online]. Available: http://www.hemianopsia.net/the-gottlieb-visual-field-awar/.

[39] "The Peli Lens," 2014. [Online]. Available: http://www.hemianopia.org/index_files/Prismglasses.htm. [Accessed 2014].

[40] 2014. [Online]. Available: http://www.maculareyewear.com/. [Accessed 2014].

[41] "E-Scoop Glasses," 2014. [Online]. Available: http://designsforvision.com/LVhtml/LV-E-Scoop.htm. [Accessed 2014].

[42] G. Legge, M. Schleske and D. Pelli, "Psychophysics of Reading III: A fiberscope low-vision reading aid," vol. 26, no. 5, pp. 751-763, 1985.

[43] G. Legge, Interviewee, [Interview]. July 2013.

[44] R. Kinkade, Guide for Macular Degeneration Eyeglasses: Low Vision Treatment, 2013.

[45] J. Wolffsohn and R. Peterson, "A review of current knowledge on electronic vision enhancement systems for the visually impaired," vol. 23, pp. 35-42, 2003.

[46] G. Goodrich, E. Mehr and N. Darling, "Parameters in the use of CCTV's and optical aids," vol. 57, pp. 881-892, 1980.

[47] J. Lovie-Kitchin and G. Woo, "Effect of magnification and field of view on reading speed using a CCTV," vol. 8, pp. 139-145, 1988.

[48] S. Chung, J. Mansfiend and G. Legge, "Psychophysics of Reading XVIII: The effect of print size on reading speed in normal and peripheral vision," vol. 38, no. 19, pp. 2949-2962, 1998.

[49] G. Legge, G. Rubin, D. Pelli and M. Schleske, "Psychophysics of Reading II: Low Vision," vol. 25, no. 2, pp. 253-266, 1985.

[50] G. Legge and G. Rubin, "Psychophysics of Reading IV: wavelength effects in normal and low vision," vol. 3, pp. 40-51, 1986.

[51] L. Zabel, H. Bouma and H. Melotte, "Investigation into the use of the TV Magnifier in the Netherlands: a survey," vol. 86, pp. 25-29, 1982.

[52] "SightMate LV920," [Online]. Available: http://citadel.sjfc.edu/students/scm03254/e-port/msti%20260/vuzix.html. [Accessed 2014].

[53] "Vuzix Sightmate," [Online]. Available: http://gadgets.softpedia.com/gadgetsImage/Vuzix-Eyetonomy-SightMate-LV920-Viewer--1-860.html. [Accessed 2014].

[54] T. Fisher and R. Juday, "A programmable video image remapper," vol. 938, pp. 122-128, 1988.

[55] D. Loshin and R. Juday, "The Programmable Remapper: Clinical applications for patients with field defects," vol. 66, no. 6, pp. 389-395, 1989.

[56] S. Downs and N. Black, "The feasibility of creating a checklist for the assessment of the methodological quality both of randomized and non-randomized studies of health care interventions," vol. 52, pp. 377-384, 1998.

[57] P. Hooper, J. Jutai, G. Strong and E. Rusell-Minda, "Age-related macular degeneration and low vision rehabilitation: a systematic review," vol. 43, no. 2, pp. 180-187, 2008.

[58] R. Al-Karmi and S. Markowitz, "Image relocation with prisms in patients with age-related macular degeneration," vol. 41, pp. 313-318, 2006.

[59] U. Nilsson, "Visual rehabilitation with and without education training in the use of optical aids and residual vision. A prospective study of patients with advanged

age-related macular degeneration," vol. 6, pp. 3-10, 1990.

[60] R. Rosenberg, E. Faye, M. Fisher and D. Budick, "Role of prism relocation in improving visual performance of patients with macular dysfunction," vol. 66, pp. 747-750, 1989.

[61] H. Smith, C. Dickenson, I. Cacho, B. Reeves and R. Harper, "A randomized controlled trial to determine the effectiveness of prism spectacles for patients with age-related macular degeneration," vol. 123, pp. 1042-1050, 2005.

[62] C. Verezen, H. Volker-Dieben and C. Hoyng, "Eccentrice viewing spectacles in everyday life for optimum use of residual functional retinal areas in patients with age related macular degeneration," vol. 73, no. 6, pp. 413-417, 1996.

[63] M. Parodi, L. Toto, M. Depollo and G. Ravalico, "Prismatic correction in patients affected by age-related macular degeneration," vol. 18, pp. 828-832, 2004.

[64] M. Everingham, B. Thomas and T. Troscianko, "Head mounted mobility aid for low vision using scene classification techniques," 1999.

[65] M. Everingham, B. Thomas and T. Troscianko, "Wearable mobility aid for low vision using scene classification in a Markov random field model framework," vol. 15, no. 2, pp. 231-244, 2003.

[66] J. Prothero, "The treatment of akinesia using virtual images," 1993.

[67] R. Massof and D. Rickman, "Obstacles encountered in the development of the low vision enhancement system," vol. 69, pp. 32-41, 1992.

[68] E. Peli, "Head mounted display as a low vision aid," 1995.

[69] E. Peli, "Vision multiplexing: an engineering approach to vision rehabilitation device development," vol. 78, no. 5, pp. 304-315, 2001.

[70] E. Peli and G. Lou, "Use of an augmented-vision device for visual search by patients with tunnel vision," vol. 47, no. 9, pp. 4152-4159, 2006.

[71] G. Goodrich and A. Zwern, "From virtual reality to large print access: development of a head mounted virtual display," Atlanta, Georgia, 1995.

[72] J. Wolffsohn, D. Mukhapodhyay and M. Rubinstein, "Image enhancement of real-time television to benefit the visually impaired," vol. 144, no. 3, pp. 436-440, 2007.

[73] F. Vargas-Martin, M. Palaex-Cocaa, E. Ros, J. Diaz and S. Mota, "A generic real-time video processing unit for low vision," vol. 1282, pp. 1075-1079, 2005.

[74] W. Atabany and P. Degenaar, "A robust edge enhancement approach for low vision patients using scene simplification," 2008.

[75] R. Juday, R. Barton, C. Johnson and D. Loshin, "Conformal and other image warpings for reading with field defect," pp. 92-102, 1994.

[76] R. Juday and D. Loshin, "Quasi-conformal remapping for compenstation of human visual field defects: Advances in image remapping for human visual field defects," vol. 1053, pp. 124-130, 1989.

[77] R. Juday and D. Loshin, "Some examples of image warping for low vision prosthesis," pp. 163-168, 1988.

[78] K. M. Miller, D. L. Alber, P. A. Asbell, N. H. Atebara and R. J. Schecter, Clinical Optics, 2008-2009, American Academy of Ophthalmology, 2008.

[79] K. Deepinder and M. Hassanlou, "Overview of Refractive Error," September 2013. [Online]. Available: http://www.merckmanuals.com/professional/eye_disorders/refractive_error/overview_of_refractive_error.html. [Accessed 2014].

[80] J. Garvin, "The Physics of Vision," University of Alaska, Fairbanks, 2013. [Online]. Available: http://ffden-2.phys.uaf.edu/211_fall2013.web.dir/jessica_garvin/background_info.htm. [Accessed 2014].

[81] "Global Computer Vision," Free University of Berlin, [Online]. Available: http://robocup.mi.fu-berlin.de/buch/chap9/ComputerVision.htm. [Accessed 2014].

[82] K. R. Spring and M. W. Davidson, "Astigmatism," Nikon, 2013. [Online]. Available: http://www.microscopyu.com/tutorials/java/aberrations/astigmatism/. [Accessed 2014].

[83] Image Engineering, "Longitudinal and Lateral Chromatic Aberration," 2014. [Online]. Available: http://www.image-engineering.de/index.php?option=com_content&view=article&id=510. [Accessed 2014].

[84] C. W. Brooks and I. M. Borish, System For Ophthalmic Dispensing, 3rd edition, Butterworth-Heinemann, 2006.

[85] D. Meslin and G. Obrecht, "Effect of chromatic dispersion of a lens on visual acuity," vol. 65, pp. 25-28, 1988.

[86] [Online]. Available: www.superfocus.com. [Accessed 2014].

[87] "Birefringence in Liquid Crystals," Case Western Reserve University, [Online]. Available: http://plc.cwru.edu/tutorial/enhanced/files/lc/biref/biref.htm.

[88] M. Born and E. Wolf, Principles of Optics, 7th edition, Cambridge, United Kingdom: Cambridge University Press, 1999.

[89] A. Karp, "PixelOptics Re-Emerges With Plan to Introduce Second Generation of Empower Eyewear," Vision Monday, 08 March 2013. [Online]. [Accessed 2014].

[90] "emPower eyeglasses use accelerometer and LCD layer for electronic," [Online]. Available: http://www.geek.com/chips/empower-eyeglasses-use-accelerometer-and-lcd-layer-for-electronic-focusing-1304520/.

[91] Sensics Inc., zSight Head Mounted Display User's Guide, Columbia, MD, 2012.

[92] Arrington Research, ViewPoint EyeTracker Software User Guide, Scottsdale, AZ, 2010.

[93] University of Leuven, "Dual Purkinje Eyetrackers," University of Leuven. [Online]. [Accessed 2014].

[94] SENSORAY, USB 4-Channel Video Capture Device: Model 2255 Hardware and Software Manual, Portland, OR: SENSORAY embedded electronics, 2012.

[95] "Sensoray Model 2255," [Online]. Available: http://www.sensoray.com/products/2255.htm.

[96] G. Wolberg, Digital Image Warping, Wiley-IEEE Computer Society, 1990.

[97] F. Liu and M. Gleicher, "Automatic image retargeting with fisheye-view warping," pp. 153-162.

[98] G. Furnas, "A fisheye follow-up: further reflections on focust + context," pp. 999-1008.

[99] Y. Wang, T. Lee and C. Tai, "Focus + context visualization with distortion minimizations," vol. 14, no. 6, pp. 1731-1738, 2008.

[100] J. de Villiers, F. Leuschner and R. Geldenhuys, "Centi-pixel accurate real-time inverse distortion correction," vol. 7266, pp. 1-8, 2008.

[101] OpenCV Development Team, OpenCV, 2013. [Online]. Available: docs.opencv.org. [Accessed 2014].

[102] W. R. LePage, Complex Variables and the Laplace Transform for Engineers, New York, NY: Dover Publications, 1980.

[103] G. Legge, S. Chung and S. Mansfield, "Psychophysics of Reading XVIII: The effect of print size on reading speed in normal peripheral vision," vol. 38, no. 19, pp. 2949-2962, 1998.

[104] G. Timberlake, M. Mainster, E. Peli, R. Rugliere, E. Essock and L. Arend, "Reading with a macular scotoma I: Retinal location of scotoma and fixation area," vol. 27, pp. 1137-1147, 1986.

[105] R. Schuchard and T. Raasch, "Retinal locus for fixation: Pericentral fixation targets," vol. 7, pp. 511-520, 1992.

[106] D. Fletcher and R. Schuchard, "Preferred retinal loci relationship to macular scotomas in a low vision population," vol. 104, pp. 632-638, 1997.

[107] S. Trauzettel-Klosinski, C. Teschner, R. Tornow and E. Zrenner, "Reading strategies in normal subjects and in patients with macular scotoma - assessed by two new methods of registration," vol. 14, pp. 15-30, 1994.

[108] J. Sunness, C. Applegate, D. Haselwood and G. Rubin, "Fixation patterns and reading rates in eyes with central scotomas from advanced atrophic age-related

macular degeneration and stargardt disease," vol. 103, pp. 1458-1466, 1996.

[109] E. Ergun, N. Maar, W. Radnar, I. Barbazetto, U. Schidt-Erfurth and M. Stur, "Scotoma size and reading speed in patients with subfoveal occult choroidal neovascularization in age-related macular degeneration," vol. 110, pp. 65-69, 2003.

[110] R. Schuchard, "Validity and interpretation of Amsler grid reports," vol. 111, pp. 776-780, 1993.

[111] D. Fletcher, R. Schuchard and G. Watson, "Relative locations of macular scotomas near the PRL: effect on low vision reading," vol. 36, no. 4, pp. 356-364, 1999.

[112] J. Baldasare, G. Watson, S. Whittaker and H. Miller-Shaffer, "The development and evaluation of a reading test for low vision individuals with macular loss," vol. 80, pp. 785-789, 1986.

[113] G. Legge, J. Ross, K. Maxwell and A. Luebker, "Psychophysics of Reading VII: Comprehension in normal and low vision," vol. 4, no. 1, pp. 51-60, 1989.

[114] S. Whittaker, J. Budd and R. Cummings, "Eccentric fixation with macular scotoma," vol. 29, no. 2, pp. 268-278, 1988.

[115] K. Lee and S. Markowitz, "Scotoma size reduction as an adaptive strategy in age-related macular degeneration," vol. 56, no. 4, pp. 393-398, 2010.

[116] G. Watson, W. Del'Aune, S. Long, J. Maino and J. Stelmack, "Veteran's use of low vision devices for reading," vol. 74, pp. 260-265, 1997.

[117] J. Laviola, "A discussion of cybersickness in virtual environments," vol. 32, pp. 47-56, 2000.

[118] D. Johnson, "Introduction to and review of simulator sickness research," 2005.

[119] K. Spring and M. Davidson, "Modulation Transfer Function," Nikon, 2013. [Online]. Available: http://www.microscopyu.com/articles/optics/mtfintro.html. [Accessed 2014].

[120] S. Isreal, "How to Choose a Lens," 1st Vision, Andover, MA.

[121] G. Walsh and W. Charman, "Objective technique for the determination of monochromatic aberrations of the human eye," vol. 1, no. 9, pp. 987-992, 1984.

[122] S. Anderson, K. Mullen and R. Ness, "Human peripheral spatial resolution for achromatic and chromatic stimuli: limits imposed by optical and retinal factors," vol. 442, pp. 47-64, 1991.

[123] B. Zuber, J. Semmlow and L. Stark, "Frequency characteristics of the saccadic eye movement," vol. 8, no. 11, pp. 1288-1298, 1968.

[124] D. Simon, Optimal State Estimation, Wiley, 2006.

[125] M. Kohler, "Using the Kalman Filter to track Human Interactive Motion - Modelling and Initialization of the Kalman Filter for Translational Motion," *Tech. Rep. #629, Informatik VII, University of Dortmund,* pp. 1-17, 1997.

[126] T. Grindinger, "Eye Movement Analysis & Prediction With the Kalman Filter," *Clemson University, Thesis,* 2006.

[127] D. Lowe, "Distinctive image features from scale-invariant keypoints," 2004.

[128] P. KaewTraKulPong and R. Bowden, "An improved adaptive background mixture model for real-time tracking with shadow detection," 2001.

[129] L. Ji and K. Gallo, "An agreement coefficient for image comparison," vol. 72, no. 7, pp. 823-833, 2006.

[130] E. Choi and C. Lee, "Feature extraction based on the bhattacharyya distance," vol. 36, pp. 1703-1709, 2003.

[131] D. Wilson, A. Baddeley and R. Owens, "A new metric for grey-scale image comparison," vol. 24, no. 1, pp. 5-17, 1997.

[132] E. Baudrier, F. Nicolier, G. Millon and S. Ruan, "Binary-image comparison with local-dissimilarity quantification," vol. 41, pp. 1461-1478, 2008.

[133] J. Wu and M. Trivedi, "Simultaneous eye tracking and blink detection with interactive particle filters," 2008.

[134] G. Legge, J. Ross, A. Luebker and J. LaMay, "Psychophysics of Reading VIII: The minnesota low-vision reading test," vol. 66, pp. 843-853, 1989.

[135] Lighthouse Low Vision Products, "MNRead Acuity charts, continuous-text reading-acuity charts for normal and low vision," 1994. [Online]. Available: http://gandalf.psych.umn.edu/groups/gellab/MNREAD/mnread.pdf. [Accessed 2014].

[136] A. Subramanian and S. Pardhan, "The repeatability of MNREAD acuity charts and variability at different test distances," vol. 83, no. 8, pp. 572-576, 2006.

[137] C. Curcio, K. Sloan, R. Kalina and A. Hendrickson, "Human Photoreceptor Topography," vol. 292, pp. 497-523, 1990.

[138] M. Varsori, A. Perez-Fornos, A. Safran and A. Whatham, "Development of a vewing strategy during adaptation to an artifical central scotoma," vol. 44, pp. 2691-2705, 2004.

[139] A. State, K. Keller and H. Fuchs, "Simulation-Based Design and Rapid Prototyping of a Parallax-Free Orthoscopic Video See-Through Head-Mounted Display," 2005.

[140] K. Iwamoto, "A Monocular Video See-through Head Mounted Display for Interactive Support System," 2009.

[141] "Eye Disease Anatomy," [Online]. Available: http://www.nysoa.org/index.php?page_id=132. [Accessed 2014].

[142] "Training Eccentric Viewing Technique: MagnaFlyer and Central Vision Loss," 2009. [Online]. Available: http://www.magnaflyer.net/eccen_view.html. [Accessed 2014].

[143] B. R. Land, "ECE 4760 - Optical Eye Tracking System," Cornell University, 2010. [Online]. Available: http://people.ece.cornell.edu/land/courses/ece4760//FinalProjects/s2010/yh428_aoo34/eyetracking/index.html. [Accessed 2014].

[144] D. Meslin and G. Obrecht, "Effect of chromatic dispersion of a lens on visual acuity," vol. 65, pp. 25-28, 1988.

[145] R. E. Woods, P. A. Wintz and R. C. Gonzalez, Digital Image Processing, 3rd Edition, Prentice Hall, 2007.

Appendix A

Eye Tracker Calibration for New Users

A.1 New User Calibration

In order for the HMD and eye tracker to successfully fit a new individual, some time and care must be taken to correctly adjust both items to their unique anatomical structures. The HMD adjustment straps should first be loosened holding on to the frame of the HMD so as not to strip the internal teeth of the straps. The individual should place the HMD over their head taking care not to hit the armature holding the mirror of the eye tracker. The HMD should then be tightened in a manner that allows the users visual axes to correctly align with the optical axes of the eye tubes. If the eye tubes are not laterally spaced correctly, the user should turn the IPD adjustment knob on the underside of the HMD until they are spaced correctly. If there appear to be refractive errors present in the HMD, the ends of the eye tubes may be twisted to compensate ± 4 diopters in an attempt to compensate for wearers with refractive errors.

With the HMD correctly positioned on the user, ensure that the mirror for the eye tracker is not causing discomfort. If it is, the 3 screws attached to the 2 linkages positioning it may be loosened using a hex key and the mount may be repositioned. When fittings appear to be correct, open the viewpoint eye tracking program. Set the search window to coincide with the extremes of motion for the pupil, and set the eye camera to 30 Hz high precision. Ensure that the pupil is able to be effectively located given the current brightness, contrast, minimum and maximum pupil sizes and pupil aspect ratio threshold. With these parameters correct for the user, initialize the calibration by clicking the "auto-calibrate" button. The user will be presented with, by default, 16 green squares whose centers they should stare at without blinking. Upon completion of the calibration, there will appear a mapping of points in the "eye space" window. These points should form a

quasi-rectilinear grid; if they do not, points that are deemed to be incorrect should be re-presented to the user.

A.2 ViewPoint Settings Files

The viewpoint eye tracker allows for command line instructions (CLI's) that change certain working parameters within the viewpoint workspace. These command line instructions allow users to control nearly every aspect of the viewpoint program. The CLI consists of a set of Instructions and the Command Line Parser (CLP) that in turn interprets the instructions. Each instruction sent in the CLI begins with a KeyTerm and is followed by one or more Arguments.

In this interface, strings are defined by enclosing a set of characters with quotes, comments are identified by the usual C comment identifier (//), delimiters separate command arguments, a colon is used as a target specifier (ex: EyeA: authothreshold), and braces provide a grouping of a sequence of commands.

By default, settings files are in ASCII format. They contain all GUI values and selections so that these values may be set automatically without the user having to redefine each of them individually in the GUI. By default, settings files are stored in the folder named "settings", which is located in the same folder as the ViewPoint application program.

Also by default, when the eye tracker is launched, it loads in the content of the file entitled "startup.txt", located in the settings folder. This file can be changed to automatically load default settings that are commonly used.

The settings file entitled "DefaultSettings 1.0.txt" includes default settings that have been found to be beneficial over the standard default settings that are included in the viewpoint program.

The primary changes that are made from default values are as follows:

EyeA: videoImageBrightness 0.675

- This is changed in an effort to reduce the under eye shadows that cause confusion for the program when the users blinks. Settings above this unnecessarily wash out features from the image. This parameter will be tuned on an individual to individual basis.

EyeA: pupilScanDensity 2

- This value is changed from the default 7 to try to minimize noise in the Hough transform to fit the pupil ellipse. This value specifies the pixel sampling interval for the threshold segmentation operation in the specified eye. A setting of 1 indicates to scan every pixel, a setting of 2 indicates to scan every other pixel and so on. Therefore, the smaller the number, the more computationally expensive the program becomes. This parameter will likely not require changes unless the computation expense is deemed excessive, or if the precision of eye tracking data needs to be changed.

EyeA: mappingFeature Pupil

- The string "Pupil" indicates that the feature to track is the border between the pupil and the iris.

EyeA: pupilSegmentationMethod OvalFit

- The string "Ellipse" indicates to the program that an ellipse, as opposed to other shapes, is to be fit to the detected pupil boarder. OvalFit informs the program to fit an oval to the pupil border; the user guide suggests that oval fit may provide a better avenue to detect blinks by setting a threshold on the aspect ratio.

EyeA: pupilThreshold 0.350

- The floating point number 0.350 sets the image intensity threshold such that the pupil can be segmented from the rest of the image. 0.250 is default, but was raised to this value since the image brightness was raised to try to reduce shadows. If the brightness is changed, this value should also be changed in an effort to set the intensity, ranging from 0 to 1, with which to threshold the pupil search.

EyeA: pupilScanArea 0.200 0.254 0.837 0.646

- These values were changed from 0.2 0.2 0.8 0.8, which indicates the corner values to be used for the region of interest in which the pupil is searched for. These values were reduced to try to reduce the search window to exclude portions that could not include the pupil and under eye shadows. These values will be changed on an individual to individual basis, and may need to be changed for every fitting.

EyeA: CalibData 0-15

- These data points indicated previous calibration mapping data and will be rewritten every time a new calibration is performed (which is necessary for every use). More calibration points may be used, and may prove to be beneficial if the user has abnormalities on their corneal surface.

EyeA: PositiveLock Yes

- Turns Positive-lock Threshold-Tracking on; this features continuously adjusts the intensity threshold for pupil detection in the specified eye. Changing this parameter to no and manually adjusting the threshold and contrast and brightness appears to increase eye tracking precision.

minimumPupilScanDensity 1

- Set the minimum pupil scan density to 1, e.g., set the minimum number of pixels between searches to 1 (scan every pixel for the pupil). This lower bound is reset from 7 to try to denoise the system to a certain degree (more precise pupil locating capability).

pupilAspectCriterion 0.6

- This is reset from the default 0.05. The pupil aspect criterion sets the minimum search value for the ratio of elliptical major axis to minor axis. If calculated aspect ratio goes below this value the pupil location is lost and no data should be sent. The final value used here will likely need to be tuned from the 0.6 indicated above, and should be done so by viewing the steady state pupil aspect ratio, and the ratio obtained during the process of a user blink.

calibration_StimulusDuration 30

- This is reset from the default of 15. This value specifies the delay, in milliseconds, between calibration stimulus changes. The default setting of 15 was far too quick for an individual's eye to track stimuli successfully and often resulted in poor mappings between eye space and gaze space.

At the moment, there is no way to change the video feed mode from the command line interface. As a result, to toggle between high speed (60 Hz) and high precision (30 Hz) video capture, the user will have to click the icon at the bottom right hand corner of the EyeCamera window (), then click mode, then choose “High Precision”, or “High Speed Normal”. It has been suggested by the user guide that the high precision mode may be better for high precision applications.

Additionally, although the settings file can save the location of the region of interest in which to look for the pupil, this location may easily change on an individual to individual basis. To change the region of interest, click on the EyeCamera window, click on the region of interest rectangle button (), then click the location of one corner, drag the cursor to the opposite corner to define a rectangle, and release the cursor. If you are satisfied with this region of interest click the lock button () to lock the region of interest into place. The region of interest should be defined such that shadows under the eye and at the corners of the eye (where the pupil could not possibly reside), can not interfere with locating the pupil (see below, where the red rectangle denotes the region of interest).

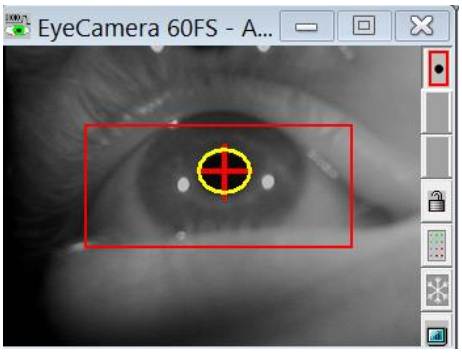

Figure A.0.1: EyeCamera pupil search window

Note in figure A.1, that the window title “EyeCamera 60FS” indicates that the eye camera is set to the high speed 60 Hz setting, which would likely perform better in the 30 Hz high precision setting, which will have the title “EyeCamera 30HP”.

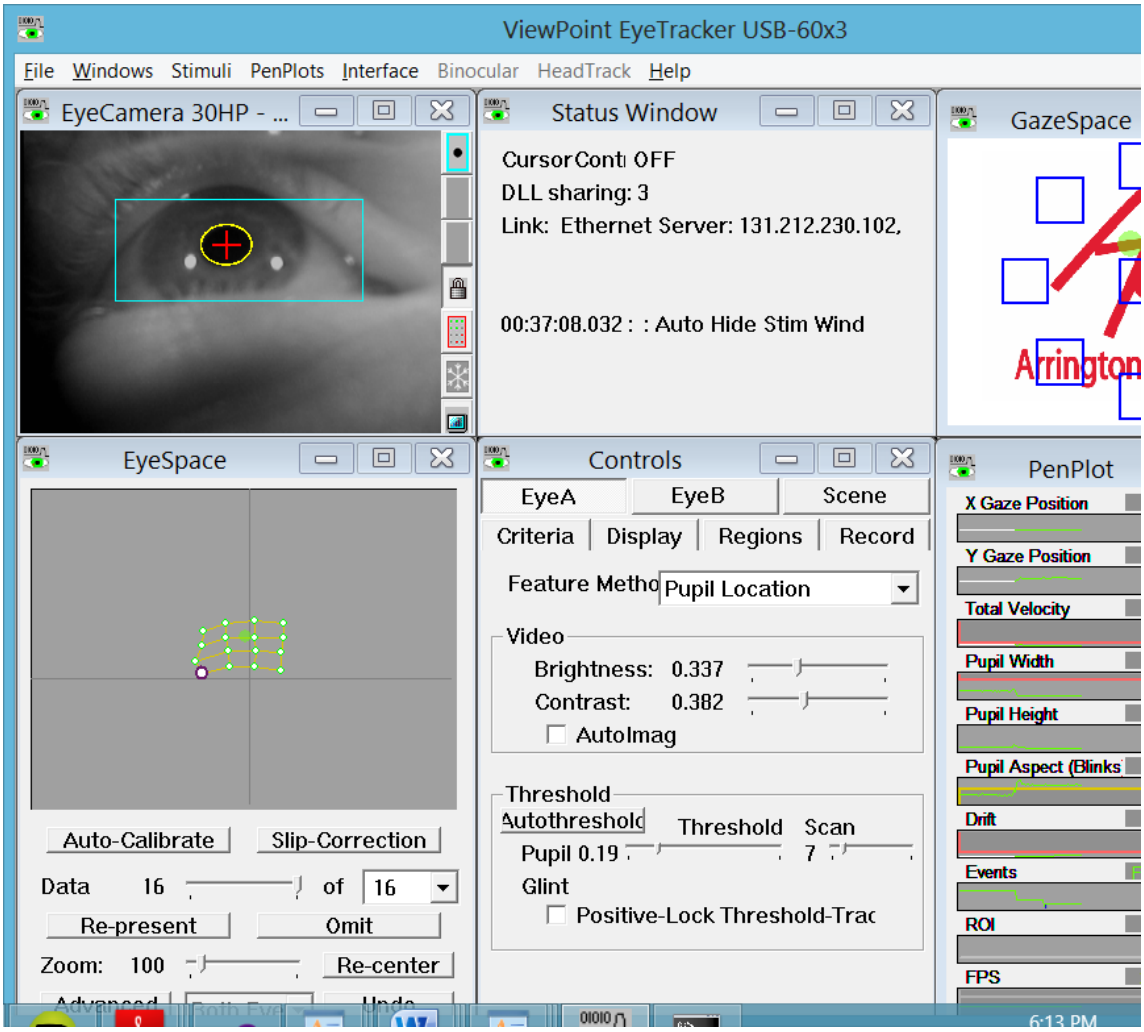

Figure A.0.2: ViewPoint EyeTracker user window

Additionally, when performing the auto-calibration, 16 points will be presented to the user. The eyespace in figure A.2 shows the mapping of these points. It is the user's responsibility to ensure that the mapping is quasi-rectilinear, as shown above. An example of a non satisfactory mapping is shown below. If a situation like this arises, the user should select the point that does not appear to be correct and click the "Re-present" button, to attempt to remap that point. Sometimes more than one point may need to be remapped, sometimes none will need to be.

Appendix B

Software Details

B.1 Software Implementation Details

In order for the program to successfully operate, two external APIs must be reachable by the IDE: OpenCV 2.4.6 and the ViewPoint API. A property sheet, "Opencv246gpu_debug2" has been created with all of the necessary properties so that OpenCV's and ViewPoint's functions can be found. For this property sheet to successfully work, the folder containing the OpenCV library and ViewPoint API must be added to the system path first. Within the property sheet are C/C++ additional include directories that reference the location of the OpenCV include files and Viewpoint API from their shortcut from the system path. Furthermore, linker additional include directories have been added so the program can identify which libraries to link to in order to use the respective APIs. Linker input additional dependencies then include all of the library files for the many OpenCV functions, as well as the VPX_interapp.lib file used to communicate with the viewpoint eye tracker.

B.2 Additional Programs Written

The additional programs written include the "mnread image creation 2.exe", included in the project of the same name, that was used to programmatically access all of the screen shots of MNRead sentences. This program can be reused to center and white pad images given that it is looking in the correct directory.

The program "s2255_simple_console.exe" was used to test the various methods of detecting when a user's eye is open and when a user'

Appendix C

MNRead Visual Acuity Test

C.1 MNRead Test Sentences and Score Sheets

Score sheets were created for the MNRead test sentences that consisted of the sentences themselves, which are to be marked if a word is incorrectly identified, and an area for recorded time and comments. The score sheets are included in their entirety below.

MNRead Score Sheet		
ID		**Date**
logMAR		**Eye OU OS OD**
Comments		Pg 1
1 My father asked me to help the two men carry the box inside *calibration*	**9** The young boy held his hand high to ask questions in school *max wpm 1*	**17** The old man caught a fish here when he went out in his boat *dense scotoma 4*
2 Three of my friends had never been to a circus before today *calibration*	**10** My brother wanted a glass of milk with his cake after lunch *max wpm 2*	**18** Our mother tells us that we should wear heavy coats outside *dense scotoma 5*
3 My grandfather has a large garden with fruit and vegetables *calibration*	**11** I do not understand why we must leave so early for the play *max wpm 3*	**19** One of my brothers went with his friend to climb a mountain *dense, remap 1*
4	**12**	**20**

My father takes me to school every day in his big green car *calibration*	It is more than four hundred miles from my home to the city *max wpm 4*	The three elephants in the circus walked around very slowly *dense, remap 2*
5 Everyone wanted to go outside when the rain finally stopped *calibration*	**13** Our father wants us to wash the clothes before he gets back *max wpm 5*	**21** We could not guess what was inside the big box on the table *dense, remap 3*
6 They were not able to finish playing the game before dinner *calibration*	**14** They would love to see you during your visit here this week *dense scotoma 1*	**22** The two friends did not know what time the play would start *dense, remap 4*
7 He told a long story about ducks before his son went to bed *calibration*	**15** The teacher showed the children how to draw pretty pictures *dense scotoma 2*	**23** He looked up at his mother and told her he was really happy *dense, remap 5*
8 My mother loves to hear the young girls sing in the morning *calibration*	**16** Nothing could ever be better than a hot fire to warm you up *dense scotoma 3*	**24** The phone rang six times before we all rushed to pick it up *dense, remap, roi 1*

MNRead Score Sheet		
ID		**Date**
logMAR		**Eye OU OS OD**
Comments		Pg 2
25 She was waiting for over an hour before	**33** The policeman said he would not let us	**41** She could not sleep after the wind blew

the doctor returned *dense, remap, roi 2*	play basketball here *relative scotoma 5*	the front door open *relative, remap, roi 3*
26 Instead of watching television we could play in your garden *dense, remap, roi 3*	**34** His blue hat was on the table before we went out for dinner *relative, remap 1*	**42** I like to read books with my teddy bear before going to bed *relative, remap, roi 4*
27 The boy carried the toy car in his hand for most of the day *dense, remap, roi 4*	**35** Today we raced our new red cars on the track outside school *relative, remap 2*	**43** There are four stop signs on the way to the big stone house *relative, remap, roi 5*
28 All of us ate dinner and then went over to see the new dogs *dense, remap, roi 5*	**36** The only thing they forgot to bring was the book about pets *relative, remap 3*	**44**
29 The children found a tiny chocolate pig inside each package *relative scotoma 1*	**37** Nobody thought we would ever find any treasure in the chest *relative, remap 4*	Additional comments:
30 I did not read all of the book because it was making me sad *relative scotoma 2*	**38** The cat climbed up onto the giant chair and had a short nap *relative, remap 5*	
31 I am making a cake today for my family and friends to enjoy *relative scotoma 3*	**39** My teacher told my brother to study the big words carefully *relative, remap, roi 1*	
32 My little puppy has a small white patch below her right eye *relative scotoma 4*	**40** We all smiled when she finally sat down and closed her eyes *relative, remap, roi 2*	

Appendix D

Glossary and Acronyms

Efforts have been made to minimize the usage of ambiguous jargon and acronyms, but complete elimination of such things can never be achieved. This section defines lexicon which may be mystifying to readers outside of disciplines that frequently use such terms.

D.1 Glossary

- **Application Programming Interface (API)** – A computer program that specifies how software components interact with each other.
- **Axon** – A long, slender projection of a nerve cell or neuron that is used to conduct electrical impulses away from a neuron cell's body.
- **Bipolar cell** – Retinal cells that receive synaptic input from retinal photoreceptors and output to ganglion cells.
- **Canny (edge detection)** – An edge detection method which utilizes multidirectional derivatives followed by non-maximum suppression and hysteresis thresholding.
- **Choroidal neovascularization –** The formation of a microvasculature structure within the innermost layer of the choroid.
- **Conformal map** – A mathematical function which preserves angles, typically with a domain and range in the complex plane.
- **Corneal limbus –** The border between the cornea and the sclera of the eye.
- **Cybersickness –** A term used to describe symptoms akin to motion sickness which arise due to being in virtual environments.

- **Diopter –** A unit of measure of the optical power of a lens which is equal to the reciprocal of its focal length.
- **Eigenvalue decomposition –** The factorization of a square matrix, A, into a canonical form, whereby a matrix is represented in terms of its eigenvalues and eigenvectors, $Av = \lambda v$.
- **Eigenvalue –** A value, v, in eigenvalue decomposition used to specify scaling in the directions of importance specified by the eigenvectors.
- **Eigenvector –** A nonzero vector that, when a matrix is multiplied by an eigenvalue v, yields a constant multiple of v; eigenvalues specify directions of simplistic importance in dynamical systems.
- **Fisheye lens** - An ultra-wide angle lens that was created to mimic the view a fish would see from under the surface of a body of water, whereby due to refraction and total internal reflection, all views of objects from above the surface are seen through a cone of light of width of about 96 degrees. The aforementioned field of view is due to a phenomenon known as Snell's window.
- **Floating point number –** A decimal representation of a real number, where there is no fixed number of digits before or after the decimal point, therefore allowing the decimal point to "float".
- **Gaussian function** – A function used to describe a normal distribution in statistics.
- **Hough transform –** A computer vision algorithm which detects lines, circles, ellipses, or other geometric patterns in images by employing an accumulator array.
- **Image histogram –** A graphical representation of the various pixel intensities of a chromatic or achromatic image.
- **Image warping –** The process of digitally manipulating an image in a manner that causes the image to appear distorted or warped.
- **Interpupillary distance –** The distance between the center of the pupils of the two eyes.
- **Mat –** The OpenCV 2.x container for images, allowing manipulating of individual pixels and data types.
- **Norm -** A metric used to compare the magnitude of a vector regardless of the vector's inherent dimension; norms may also be applied to matrices.
- **Parafoveal region –** The region surrounding the fovea centralis.
- **Periodogram –** A graphical representation of the spectral density of a signal.

- **Pixel –** A picture element in a digital picture, used as a physical point in a raster image.
- **Prism diopter –** A unit of measure for the deflecting capability of a prism equal to a deflection of 1 centimeter at a distance of 1 meter.
- **Saccade –** A fast movement of the human eye.
- **Scanning laser ophthalmoscope –** A method of examining the eye by employing confocal laser scanning microscopy as a means of diagnostic imaging of the human retina.
- **Scotoma –** An area of alteration in the field of vision consisting of a partially or entirely degenerated visual acuity that is surrounded by a normal visual field. All mammalian eyes have an anatomical scotoma where the optic nerve exits the retina.
- **Singular value decomposition –** A factorization of a real or complex non-square matrix consisting of two unitary matrices describing a rotation, and one diagonal matrix describing scaling.
- **Sobel (edge detection) –** An edge detection method which uses convolution of a kernel that approximates a first order spatial derivative.
- **Vergence –** The simultaneous movement of both eyes in opposite directions to maintain binocular vision. Convergence describes the rotation of the eyes towards each other, and divergence the rotation of the eyes away from each other.

D.2 Acronyms

- **AMD** – Age-related macular degeneration
- **API** – application programming interface
- **BCEA** – bivariate contour ellipse area
- **BCVA** – best corrected visual acuity
- **BGR** – blue, green, red color space
- **BNC** – bayonet nut coupling connector
- **CA** – chromatic aberration
- **CAD** – computer aided design
- **CCTV** – closed circuit television
- **CLI** – command line interface

- **CPU** – central processing unit
- **DC** – direct current (used to refer to steady state values)
- **DLP** – digital light processing
- **DMD** – digital micromirror device
- **EOG** – electro-oculography
- **ETDRS** – early treatment diabetic retinopathy study chart
- **EVES** – electronic vision enhancement system
- **FDAtool** – filter design and analysis tool
- **FIR** – finite impulse response filter
- **GA** – geographic atrophy
- **GP** – gaze point
- **GPU** – graphics processing unit
- **HDMI** – high definition multimedia interface
- **HMD** – head mounted display
- **IIR** – infinite impulse response filter
- **IOL-VIP** – intraocular lens for visually impaired patients
- **IPD** – interpupillary distance
- **LogMAR** – logarithm of the minimum angle of resolution
- **LVIS** – low vision enhancement system
- **MTF** – modulation transfer function
- **OCT** – optical coherence tomography
- **OD** – oculus dexter (right eye)
- **OMP** – OpenMP
- **OS** – oculus sinister (left eye)
- **OTF** – optical transfer function
- **OU** – oculus uterque (both eyes)
- **PCTF** – pre-corneal tear film layer
- **PDT** – photodynamic therapy
- **PIOL** – phakic intraocular lens
- **PRL** – preferred retinal locus
- **PTF** – phase transfer function

- **ROI** – region of interest
- **RPE** – retinal pigment epithelium
- **SIFT** – scale-invariant feature transform
- **SLO** – scanning laser ophthalmoscope
- **SMT** – spectacle miniature telescope
- **USB** – universal serial bus type connector
- **VA** – visual acuity
- **VE** – virtual environment
- **VEGF** – vascular endothelial growth factor
- **VFAS** – visual field awareness system
- **VGA** – video graphics array type connector